

3 AN EXPERIMENTAL COMPARISON OF THREE TYPICAL
AMARS ENTRY BODY SHAPES ON THE BASIS OF TOTAL
EQUILIBRIUM SHOCK-LAYER RADIATION

by

6 H. B. Dyner and W. G. Reinecke 9

1 AVCO MISSILES, SPACE AND ELECTRONICS GROUP 3
SPACE SYSTEMS DIVISION
RESEARCH AND TECHNOLOGY LABORATORIES
11 Wilmington, Massachusetts 01887

AVSSD-0228-66-RR

Contract JPL-951331

9 10 October 1966 11

APPROVED

H. Gold

H. Gold

Manager, Aerophysics Department

P. Levine

P. Levine

Project Manager

Prepared for

JET PROPULSION LABORATORY
4800 Oak Grove Avenue
Pasadena, California

This work was performed for the Jet Propulsion Laboratory,
California Institute of Technology, sponsored by the
National Aeronautics and Space Administration under
Contract NAS7-100, 25

N67 17948
(ACCESSION NUMBER)
10/10/66
(PAGES)
100
(NASA CR OR TMX OR AD NUMBER)
(THRU)
(CODE)
33
(CATEGORY)

HCA 300
MF 65

10F103

PRECEDING PAGE BLANK NOT FILMED.

ABSTRACT

An approximate comparison has been made of the total equilibrium shock-layer radiation for three potential Martian entry body shapes at 0-, 45-, and 90-degrees angles-of-attack. This assessment was performed by conducting radiation measurements in a shock tube, and shock shape measurements in a shock tunnel. Using these data, radiation results were extrapolated to a trajectory condition for the full-size vehicles using a simplified analytical model. The efficacy of the extrapolation method was tested by comparing the zero angle-of-attack extrapolated results of the shock tube to the radiation measurements obtained in ballistic range experiments (which simulated the true entry conditions except for size) and to theory. The agreement was found to be satisfactory for the blunt cone and Apollo shapes, but, due to a lack of range data and because the theory may not be valid for the tension shell, no comparison could be made for that shape.

Local radiation distribution measurements were performed in the shock tube for a blunt 60-degree half-angle cone, using a model instrumented with fiber optics. The effect of pressure on the total equilibrium radiation was determined over a limited range for the blunt cone at zero angle-of-attack.

EDITED BY:
EDITORIAL SERVICES SECTION
A.C. PETRALIA

iii/iv

CONTENTS

| | |
|---|----|
| SUMMARY | xv |
| I. INTRODUCTION | 1 |
| II. THEORETICAL BACKGROUND | 3 |
| A. Radiation Energy Transfer | 3 |
| B. Thermochemical Equilibrium and Radiation Calculations | 3 |
| C. Simulation and Scaling Considerations | 5 |
| III. EXPERIMENTAL PROGRAM | 14 |
| IV. EXPERIMENTAL FACILITIES AND PROCEDURE | 16 |
| A. Ballistic Range | 16 |
| B. Shock Tube | 24 |
| C. Shock Tunnel | 28 |
| D. Data Acquisition and Reduction | 28 |
| E. Instrumented Shock-Tube Model | 31 |
| V. ERROR ANALYSIS | 37 |
| A. Shock-Tube Tests | 37 |
| B. Range Tests | 38 |
| C. Scaling Analysis | 38 |
| VI. RESULTS AND DISCUSSION | 39 |
| A. Shock Shapes | 39 |
| B. Ballistic Range Radiation Measurements | 39 |
| C. Shock-Tube Radiation Measurements | 39 |
| D. Radiation Predictions | 54 |
| E. Instrumented Model | 62 |
| VII. CONCLUSIONS | 67 |
| VIII. REFERENCE | 69 |

CONTENTS (Concl'd)

APPENDIXES

| | |
|--|----|
| A. Radiation Calibration Theory | 75 |
| B. Optically Thin-Equilibrium Radiation Criteria | 79 |
| C. Theoretical Radiation Calculations | 81 |
| D. Shock-Tube Simulation of Radiative Intensity | 89 |

ILLUSTRATIONS

| | | |
|----------|---|----|
| Figure 1 | Geometry for Radiative Transfer Solution | 4 |
| 2a | NASA Ames Theoretical Spectral Distribution: Trajectory Condition | 6 |
| 2b | NASA Ames Theoretical Spectral Distribution: Shock- Tube Condition | 7 |
| 2c | NASA Ames Theoretical Spectral Distribution: Ballistic Range Condition | 8 |
| 3a | Avco Theoretical Spectral Distribution: Shock-Tube Condition | 9 |
| 3b | Avco Theoretical Spectral Distribution: Ballistic Range Condition | 9 |
| 4 | Ballistic Range Schematic | 17 |
| 5 | Photograph of Tension Shell Model and Sabot | 18 |
| 6a | Ballistic Range Spectrum: Ablating Model | 20 |
| 6b | Ballistic Range Spectrum: Nonablating Model | 21 |
| 7 | Head-on Measurement Schematic | 22 |
| 8 | Output of Radiometers Viewing the Approaching Model Head-on | 23 |
| 9 | 6-1/2-Inch Combustion-Driven Shock Tube | 25 |
| 10 | Shock-Tube Optical System | 26 |
| 11 | Typical Shock-Tube Data | 27 |
| 12a | Spectral Response of Entire Shock-Tube Optical System.. | 29 |
| 12b | Spectral Response of Entire Ballistic Range Optical System | 30 |

ILLUSTRATIONS (Cont'd)

| | | | |
|--------|-----|--|----|
| Figure | 13 | Martian Entry Body-Shape Test Models | 32 |
| | 14 | Instrumented 60-degree Half-Angle Blunt Cone | 33 |
| | 15 | Angular Calibration of Fiber Bundles | 34 |
| | 16 | Spectral Transmission of Crofon Plastic Fiber | 35 |
| | 17 | Fiber Optics Data; Run No. 183 | 36 |
| | 18a | Shock-Tunnel Schlieren Photograph of Blunt Cone; $\alpha = 0$ degrees | 40 |
| | 18b | Shock-Tunnel Schlieren Photograph of Blunt Cone; $\alpha = 45$ degrees | 40 |
| | 18c | Shock-Tunnel Schlieren Photograph of Blunt Cone; $\alpha = 90$ degrees | 40 |
| | 18d | Shock-Tunnel Schlieren Photograph of Modified Apollo; $\alpha = 0$ degrees | 40 |
| | 18e | Shock-Tunnel Schlieren Photograph of Modified Apollo; $\alpha = 45$ degrees | 40 |
| | 18f | Shock-Tunnel Schlieren Photograph of Modified Apollo; $\alpha = 90$ degrees | 40 |
| | 18g | Shock-Tunnel Schlieren Photograph of Tension Shell; $\alpha = 0$ degrees | 40 |
| | 18h | Shock-Tunnel Schlieren Photograph of Tension Shell; $\alpha = 45$ degrees | 47 |
| | 18i | Shock-Tunnel Schlieren Photograph of Tension Shell; $\alpha = 90$ degrees | 48 |
| | 18j | Image Converter Photograph of Tension Shell in Shock Tube; $\alpha = 0$ degrees | 49 |
| | 19 | Shock-Tube Radiation Data (S-11) | 51 |

ILLUSTRATIONS (Concl'd)

| | | | |
|--------|----|---|----|
| Figure | 20 | Shock-Tube Radiation Data (S-1) | 52 |
| | 21 | Shock-Tube Radiation Pressure Effect Data (S-11) | 55 |
| | 22 | Shock-Tube Radiation Pressure Effect Data (S-1) | 56 |
| | 23 | Extrapolated Trajectory Data (S-11; $R_B = 9.25$ feet) . . . | 59 |
| | 24 | Extrapolated Trajectory Data (S-1; $R_B = 9.25$ feet) | 60 |
| | 25 | Comparison of Radiation Heating Rate Distributions | 66 |
| C-1a | | Blunt-Cone Hypersonic Shock Shape and Pressure Distribution | 82 |
| C-1b | | Modified Apollo Hypersonic Shock Shape and Pressure Distribution | 83 |
| C-1c | | Tension Shell Hypersonic Shock Shape and Pressure Distribution | 84 |
| C-2 | | Blunt-Cone and Trajectory Condition Radiation Heating Rate Distribution | 85 |
| C-3 | | Modified Apollo Trajectory Condition Radiation Heating Rate Distribution | 86 |
| C-4 | | Tension Shell Trajectory Condition Heating Rate Distribution | 87 |
| D-1 | | Intensity Ratio versus Shock Angle | 91 |
| D-2 | | Enthalpy Ratio versus Shock Angle | 91 |
| D-3 | | Intensity Error versus Shock Shape | 91 |

TABLES

| | | | |
|-------|------|--|----|
| Table | I | Shock-Tube Text Matrix and Nominal Conditions | 15 |
| | II | Radiative Volumes | 50 |
| | III | Ballistic Range Radiation Data | 50 |
| | IV | Shock-Tube Radiation Data | 53 |
| | V | Comparison of Predicted to Actual Ballistic Range Data ... | 58 |
| | VI | Comparison of Predicted Free-Flight Radiation | 61 |
| | VII | Fiber Optics Data | 63 |
| | VIII | Shock-Wave Standoff Distances | 63 |
| | AI | Spectral Correction Factors | 77 |
| | CI | Trajectory Point Radiation Properties | 88 |

SYMBOLS

| | | |
|--------------|---|---|
| A | = surface area | , cm^2 |
| \AA | = angstrom | |
| B_λ | = Planck Black Body function | , watt/cm^2 steradian μ |
| C_2 | = hc/k , second radiation constant | , $\text{cm}^\circ \text{K}$ |
| f | = electronic oscillator strength | |
| H | = radiative density | , watt/cm^3 |
| I_λ | = monochromatic radiation flux intensity | , watt/cm^2 steradian μ |
| J | = radiative flux | , watt/ster |
| N | = total number density | , particles/cm^3 |
| p | = pressure | , atmosphere |
| \dot{q} | = heating rate per unit surface area | , watt/cm^2 |
| R | = local body radius | , cm |
| r | = radius vector | , cm |
| r_o | = e^2/mc^2 is the classical electron radius | , cm |
| R_B | = body base radius | , cm |
| S_λ | = spectral radiance of tungsten filament source | , $\text{watt/cm}^2 \text{ ster } \mu$ |
| T | = temperature | , $^\circ \text{K}$ |
| u | = velocity | , $\text{mm}/\mu\text{sec}$ |
| V | = radiating volume | , cm^3 |
| W | = total energy transfer to surface | , watts |
| X, Y | = arbitrary variables | |

SYMBOLS (Cont'd)

| | | |
|----------------------|--|---------------------------|
| α | = angle-of-attack | , degrees |
| γ | = specific heat ratio | |
| δ | = local shock standoff distance | , cm |
| ϵ_{λ} | = spectral emissivity of tungsten source | |
| ϕ | = azimuthal angle | , radians |
| Φ | = a factor containing the Franck-Condon factors and corrections for the rotational structure | |
| λ | = wavelength | , microns |
| μ_{λ} | = monochromatic absorption coefficient | , cm^{-1} |
| μ^* | = nongray absorption coefficient (ref. 9) | , cm^{-1} |
| ρ | = gas density | , gm/cm^3 |
| θ | = longitudinal angle | , radians |
| ν_{00} | = wave number of the 0-0 vibrational transition, | , cm^{-1} |
| ω | = solid angle | , steradians |

Subscripts

| | |
|---|---|
| A | = Apollo shape |
| a | = shock-tube conditions |
| b | = ballistic range condition |
| B | = blue wavelength radiometer region ($3400\overset{\circ}{\text{\AA}}$ - $5600\overset{\circ}{\text{\AA}}$) |
| C | = blunt cone shape |
| c | = trajectory condition |

SYMBOLS (Concl'd)

Subscripts

- i = ith-species
 - R = red wavelength radiometer region ($4800\text{\AA} = 13,000\text{\AA}$)
 - st = stagnation conditions
 - 1 = stagnation point
 - 2 = fiber bundle location halfway between apex and cone edge ($R/R_B = .5$)
 - 3 = fiber bundle location at cone edge ($R/R_B = 1.0$)
 - 4 = fiber bundle location in base of cone ($R/R_B = 0.5$)
 - ∞ = free-stream conditions
 - *
- * = nominal test conditions

SUMMARY

Total shock-layer equilibrium radiation has been measured and compared experimentally for three typical Martian entry body shapes (60-degree half-angle blunt cone, modified Apollo, and tension shell). The radiation measurements were performed at zero degrees angle-of-attack for models launched by a light gas gun in a ballistic range, and at 0-, 45-, and 90-degrees angle-of-attack in a combustion-driven shock tube. All the tests were performed at one nominal stagnation temperature (5730° K) and a stagnation pressure-diameter product gaged to ensure that the radiation was primarily in equilibrium and the shock layer was optically thin. In addition, shock-shape measurements at the three angles-of-attack were obtained in the shock tube with an image converter and in a shock tunnel with a conventional schlieren system, using CF₄ as the test gas. This low specific heat ratio ($\gamma = 1.08$) gas yielded the hypersonic conditions (density ratio approximately 15) corresponding to free flight in the Martian atmosphere, and enabled the accurate simulation of the shock shapes not obtainable in the shock tube.

A simple scaling of the radiation data, using the ratio of the radiating volumes, was used to obtain the comparative heating loads to the three configurations. This scaling method was tested by comparing the shock-tube and range measurements; agreement was found to be within a factor of 2 for the comparative heating load for the cone and Apollo shapes. The tension shell data were insufficient to check the scaling criteria. The purpose of the shock-tube experiments was to obtain radiation data that could be scaled to a full-size vehicle at a point along a Martian trajectory. The range data were used as a check on the validity of the scaling analysis. The results for the relative, full-scale, total radiative heat load to the vehicle surface during Martian entry are summarized (versus angle of attack) in the following table:

| Angle of Attack | $\frac{W_{\text{Apollo}}}{W_{\text{Cone}}}$ | $\frac{W_{\text{Tension Shell}}}{W_{\text{Cone}}}$ |
|-----------------------|---|--|
| 0 degrees | 2.9 | 16.0 |
| 45 degrees | 1.7 | 1.8 |
| 90 degrees | 3.0 | 0.7 |

Large differences were noted in the shock shapes taken in the shock tube and the shock tunnel, due to the low flow Mach number in the shock tube. In order to assess the angle-of-attack variations, large volumetric scaling factors were required, and the shock-tunnel data were particularly valuable for doing the scaling to the flight condition.

The effect of ambient pressure on the radiation was assessed for the blunt cone at constant stagnation temperature over a pressure range from 1 to 10 torr initial shock-tube pressure, and showed the expected increase with pressure over the limited range investigated.

Point measurements of the radiation to the surface of a blunt 60-degree, half-angle cone were made in the shock tube, using a model instrumented with four fiber optical bundles. The three-point radiation distribution, thus obtained, agreed qualitatively with the theoretical result that the radiation at locations on the body other than the stagnation point may be higher than that at the stagnation point. The ratios of radiation to the body at a mid-point on the cone ($R/R_B = 0.5$) to that at the stagnation point was found, via a scaling analysis based on the shock-tube data, to be 1.8 compared to simple theoretical estimates of 1.5 - 4.0, while at the cone edge, an experimentally scaled ratio of 12 compared to 3-5 from the simple theory.

ACKNOWLEDGEMENT

The authors wish to acknowledge Messers. Todisco, McKay, Buck, and Harrington for their assistance in the conduct of the experiments, and to A. Modica and J. Eckerman for their concept of the experiments.

I. INTRODUCTION

It has been shown,¹ that at certain points along an entry trajectory, the radiative heat transfer to a vehicle may dominate the convective heat transfer, and thus become a significant factor in the determination of the most efficient heat-shield design. The fact that the total radiation to the entering vehicle from Martian type atmospheres may exceed the radiation from air at the velocities required for planetary entry² establishes the need for accurate determination of the radiative energy transfer to the body surface.

The problems associated with the determination of the total radiation to a body are (1) the distribution of radiative flux over the body, (2) the effect of wavelength dependent absorption coefficient, (3) the effect of self-absorption, and (4) nonequilibrium radiation. The earliest investigations of the effect of radiation on a vehicle were limited mainly to stagnation point heating^{3, 4} because of the relative simplicity of the analysis, and because the magnitude of the radiation had been shown to fall off rapidly away from the stagnation point.^{5, 6} The analyses³⁻⁷ that considered the radiation in the stagnation region assumed a grey gas emissivity, or treated the gas cap as a transparent, infinite radiating slab, using the actual gas emissivity and assuming the body surface to be black-body.

An early attempt to predict the variation of heat transfer at points on the body away from the stagnation point, was made by DeL'Estoile and Rosenthal.⁵ They showed that the radiative heat transfer rate diminished by more than a factor of 2 faster than the convective heat-transfer rate along a meridian line of a hemispherical nose. This result is expected because the radiative transfer goes as T^4 , a much greater temperature dependence than that of convective heat transfer. Bobbit¹ performed a simple analysis of the effect of shape (bluntness) for various bodies at hyperbolic velocities, assuming that the total heating rate to the body (convective plus radiative) could be expressed as the product of a geometrical factor and the stagnation point heating rate. He showed that the decrease in the convective heating rate with greater bluntness was greatly offset by the increase in radiation. Furthermore, he showed that a measurement of stagnation point heating rates would fail to indicate the effects of shape changes. Since the most important region, from the standpoint of efficient heat-shield design, is the area away from the stagnation point⁸ (because of the larger surface area exposed to the radiation), the accurate determination of the total heating is desirable as a screening criterion for vehicle shape selection.

Several analyses of the radiative transfer to the stagnation point of a vehicle have been made taking into account the actual wavelength dependence of the radiation.^{3, 4, 9} These analyses, however, have been limited to that of an optically thin gas of simple geometry. To date, there has been no accurate method accounting for the effect of self-absorption except in the case of simple geometry and/or spectrally averaged absorption coefficients. A conservative estimate

of the effects of spectral self-absorption in the shock layer of an entry body has, however, recently been made.^{8,9} The method of Reference 8 can be used to obtain a conservative estimate of the effect of self-absorption in four important band systems $N_2^+(1-1)$, CN_v , CN_{red} , and $CO(4^+)$ if the temperature of the gas and the number densities of the specie are known.

In considering the effect of radiative heat transfer from the shock layer, one can distinguish between emission from the gas in a nonequilibrium thermodynamic state immediately after passing through the bow shock, and in the equilibrium thermodynamic state near the body. The magnitude of the nonequilibrium radiation may be several times that of the equilibrium radiation^{10,11,12} at some points on the entry trajectory; however, the portion of the shock layer from which the radiation is in nonequilibrium may be so small that the total radiation may be considered to be equilibrium radiation. That is, with regard to Figure 10 of Reference 11, the integral of the radiative intensity, H , over the shock layer standoff distance can be approximated by the integral of the equilibrium radiative intensity, H_{eq} , over that distance. The experiments reported below are concerned only with simulating radiation that satisfies this criterion.

From these considerations, it is concluded that a reliable, purely analytical determination of the shock-layer radiation to complex shapes is currently beyond the state-of-the-art. On the other hand, the selection of Martian probe shapes requires knowledge of this radiation. What is required, and was proposed to the Jet Propulsion Laboratory, is an approximate but realistic experimental determination of the total equilibrium radiation for various proposed Martian entry shapes.

The purpose of the reported experiments was to conduct tests on scale models to compare the total equilibrium radiation heat loads for three J.P.L.-approved entry body shapes under simulated Martian entry conditions over a range of angles-of-attack up to and including 90 degrees. Briefly, the technique employed in the reported tests was to conduct detailed radiation measurements in a shock tube, and shock-shape measurements in a shock tunnel for the three body shapes (blunt cone, Apollo, tension shell) at 0, 45, and 90 degrees angle of attack. The results were then employed in a simple analytical model to extrapolate the analysis to a full-scale vehicle. The efficacy of the extrapolation method was tested by comparing scaled results of the shock-tube tunnel data and the results from ballistic range firings, which simulated the real entry case in all significant regards but size.

In addition, local measurements of the radiation to the surface of a blunt 60 degree half-angle cone were made in the shock tube using a model instrumented with fiber optics, and the effect of pressure on radiative energy transfer was assessed for the cone at zero degree angle-of-attack.

II. THEORETICAL BACKGROUND

A. RADIATION ENERGY TRANSFER

The complexities inherent in calculating the radiative heat transfer to a body surface arise from the fact that the transfer equations are field equations. Consequently, the radiation to a point on the body depends on the conditions in the entire inhomogeneous radiating volume, and not just on the gas in the immediate vicinity of the point of interest.

Consider Figure 1; following the method of Reference 13, the total energy, q , transferred per unit time and per unit area of the surface, dA , is

$$\dot{q} = \int_{\lambda=0}^{\infty} \int_{\omega=0}^{2\pi} I_{\lambda} \cos \theta \, d\lambda \, d\omega = \int_{\lambda=0}^{\infty} \int_{\theta=0}^{\theta(\phi) \leq \pi/2} \int_{\phi=0}^{2\pi} I_{\lambda} \cos \theta \sin \theta \, d\theta \, d\phi \, d\lambda, \quad (1)$$

where the integration has been taken over all frequencies λ , and over all possible directions of incident radiation in a solid angle no greater than 2π steradians (the solid angle may be less than 2π steradians at points on the body away from the stagnation point; e.g., the inflection point on the tension shell).

A further complication to the above equation arises from the factor I_{λ} , the monochromatic intensity of the radiation flux incident on unit area of the surface in the solid angle $d\omega$, which makes an angle θ with respect to the normal surface. I_{λ} in itself is the solution to the radiative transfer equation

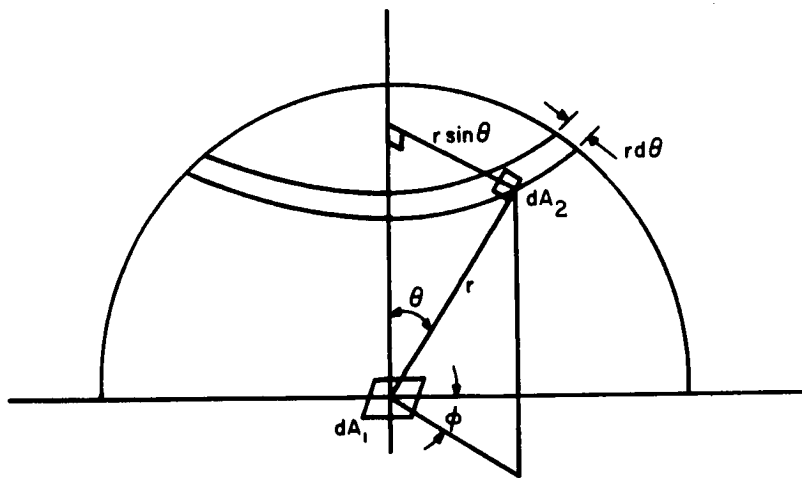
$$\frac{dI_{\lambda}}{dr} = \mu_{\lambda}' [B_{\lambda}(r) - I_{\lambda}] \quad (2)$$

where μ_{λ}' is the absorption coefficient allowing for induced emission.

It is quite evident that the solution to the radiation transfer problem for any actual reentry vehicle would be a huge task. The complexity of this problem has generally been circumvented by the assumption of simple geometries, transparent gases, blackbody surfaces, and spectrally averaged absorption coefficients (the so-called gray gas approximation).

B. THERMOCHEMICAL EQUILIBRIUM AND RADIATION CALCULATIONS

A thermochemical equilibrium calculation coupled with the Rankine-Hugoniot equations¹⁴ was used to calculate the equilibrium conditions in the stagnation region of the ballistic range models, the shock-tube models, and the actual entry vehicles. The determination of a spectral distribution for the radiating



86-8717

Figure 1 GEOMETRY FOR RADIATIVE TRANSFER SOLUTION

gas is necessary for the determination of absolute intensity from the experimental measurements. The procedure for obtaining this is explained in detail in Appendix A. Theoretical spectral distributions at the conditions of interest were calculated by both the Ames Research Center of NASA¹⁵ and by Avco. The former calculation was the smeared line model of Williams and Treanor,¹⁶ while the latter used Keck's¹⁷ model for the smeared-out rotational structure to compute the spectral intensities of diatomic band systems. The equation used by Avco to calculate the diatomic absorption coefficient for species i is

$$\mu_{\lambda_i} = \pi r_o f_i N_i \Phi \frac{C_2}{T} \exp \left[-\frac{C_2}{T} \left(\nu_{00} - \frac{1}{\lambda} \right) \right] \quad (3)$$

The calculation also computes the bound-free absorption coefficient, which is not of importance at our test conditions.

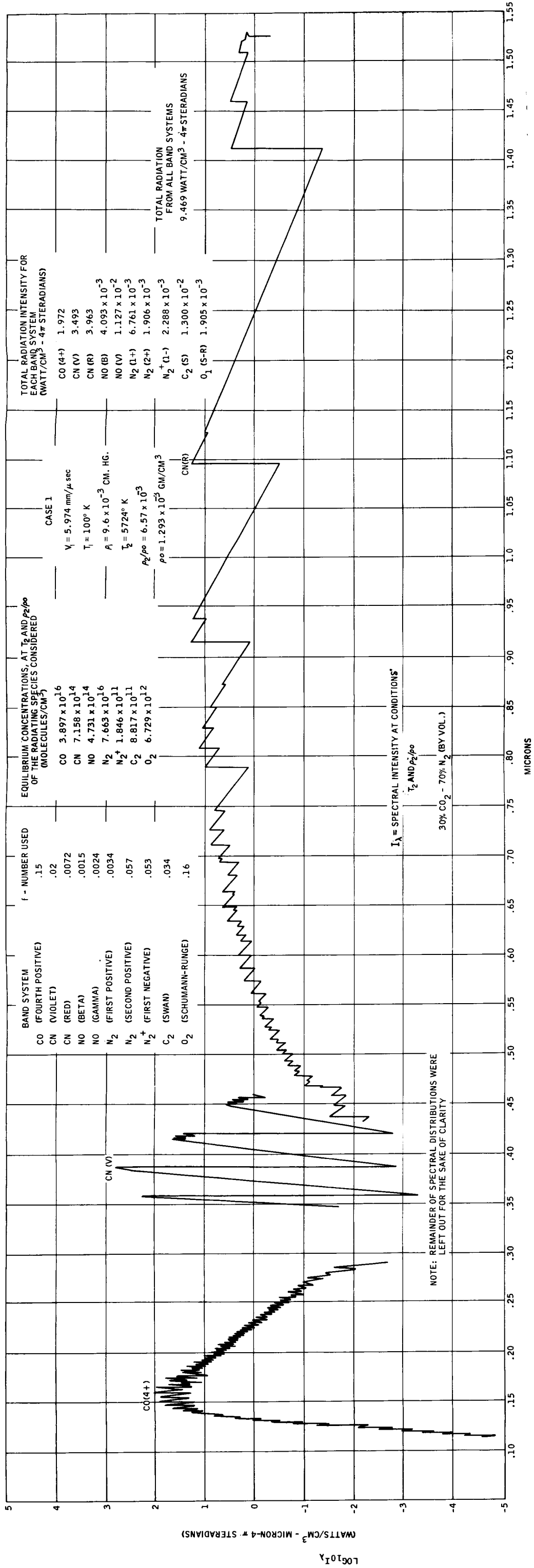
Once the absorption coefficients are calculated as a function of wavelength, they are summed at each wavelength, giving the total spectral absorption coefficient as a function of temperature and pressure. These values are then used in the solution of Equations (1) and (2) and solved for the assumption of a plane, parallel, optically thin layer.

Certain discrepancies were found between the two (Ames and Avco) spectral distributions. The main causes for the discrepancies were the different dissociation energies used for CN (8.2 eV by Ames and 7.5 eV by Avco) (see Reference 18), the different oscillator strengths, and the inclusion of the Co-Angstrom band system in the Avco calculation. The higher dissociation energy for CN used by Ames led to a larger CN number density, and thus a larger contribution to the total radiation from the CN-band systems. The inclusion of the Co-Angstrom band system in the Avco program, assuming an oscillator strength of 0.01, changed the spectral distribution significantly. The two spectral distributions are shown in Figures 2 and 3.

The detailed spectral distributions are not required for the assessment of the relative merits of the three shapes in each facility, since they were assessed using the same instrumentation at the same test conditions. A spectral distribution must be assumed, however, when scaling the shock-tube data to the range and trajectory conditions. While not proposing either theoretical spectra as being exactly representative of the radiation, the Ames spectrum was chosen on the basis of a qualitative resemblance to the experimentally measured spectrum (see Figure 6b).

C. SIMULATION AND SCALING CONSIDERATIONS

The flight condition along the Martian entry trajectory chosen to be simulated was 19,600 ft/sec with ambient conditions of 5.05×10^{-7} gm/cc and 100° K. The model atmosphere was taken to be 30-percent CO_2 + 70-percent N_2 (by volume). This point corresponded to the altitude of maximum estimated heating for a case of direct entry at an angle of -25 degrees.¹⁹



86-8718

Figure 2a NASA AMES THEORETICAL SPECTRAL DISTRIBUTION: TRAJECTORY CONDITION

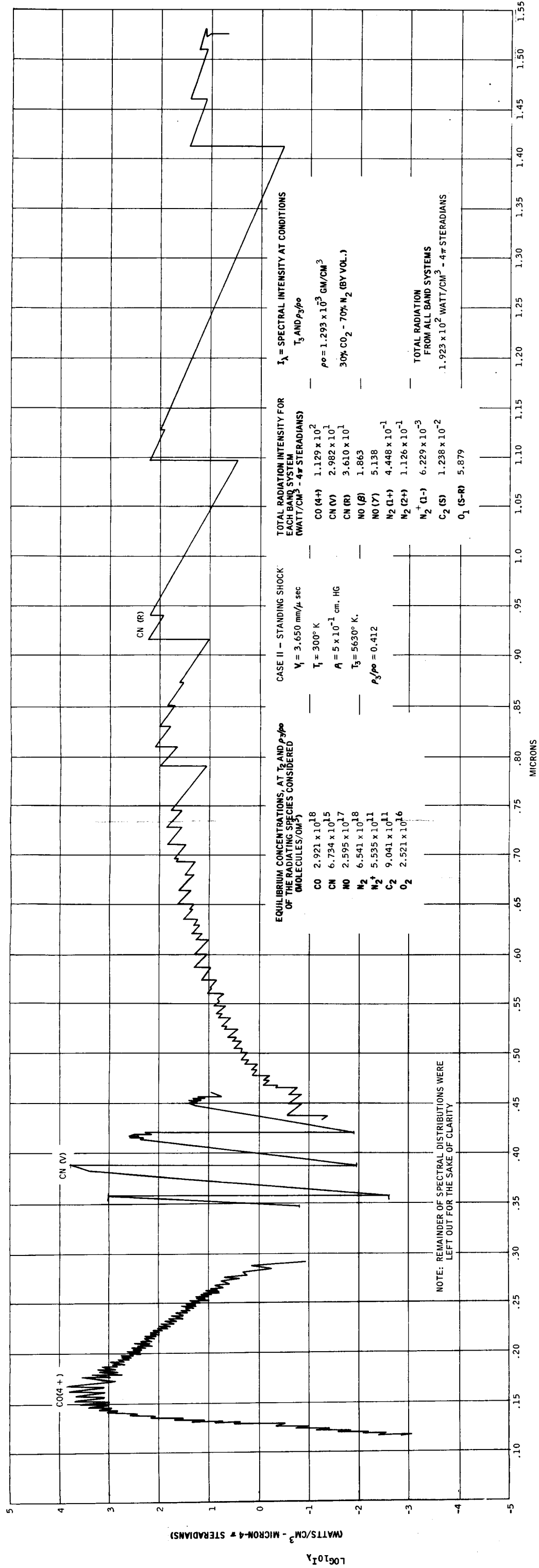


Figure 2b NASA AMES THEORETICAL SPECTRAL DISTRIBUTION: SHOCK-TUBE CONDITION

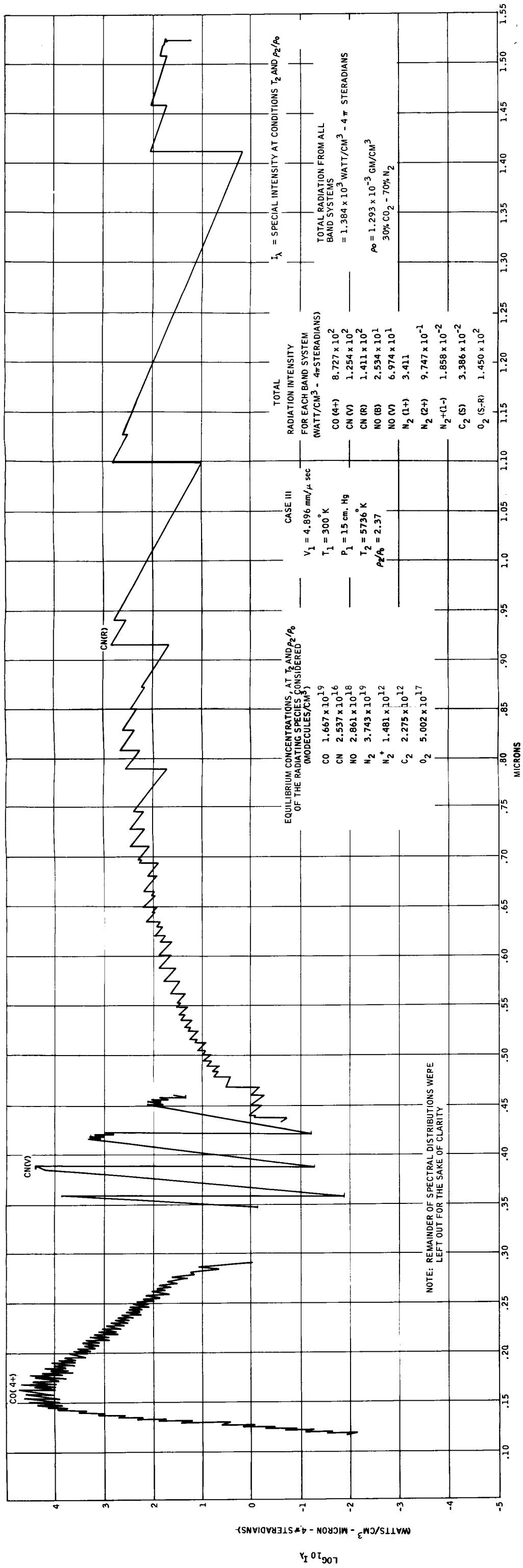


Figure 2c NASA AMES THEORETICAL SPECTRAL DISTRIBUTION: BALLISTIC RANGE CONDITION

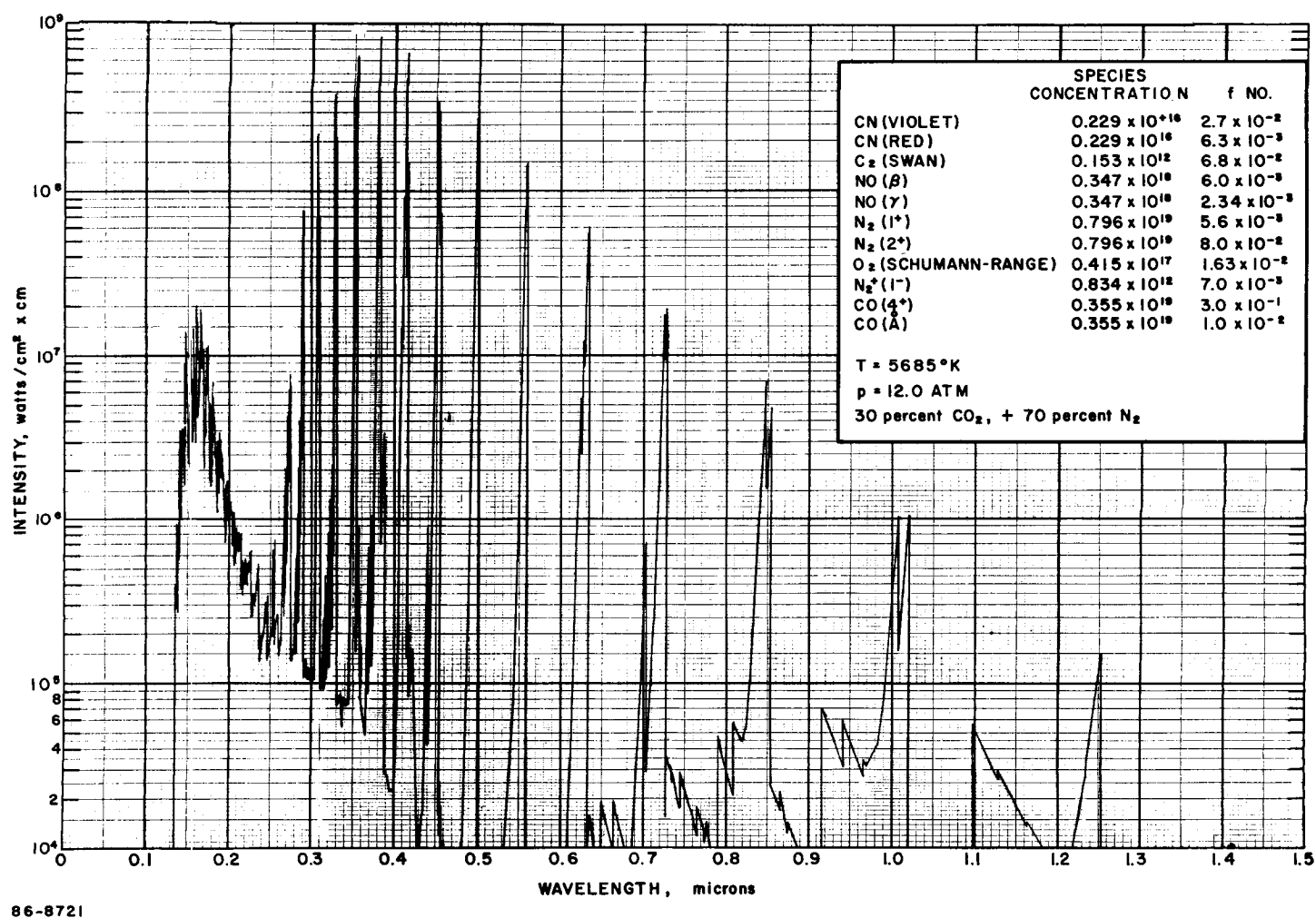


Figure 3a AVCO THEORETICAL SPECTRAL DISTRIBUTION:
SHOCK-TUBE CONDITION

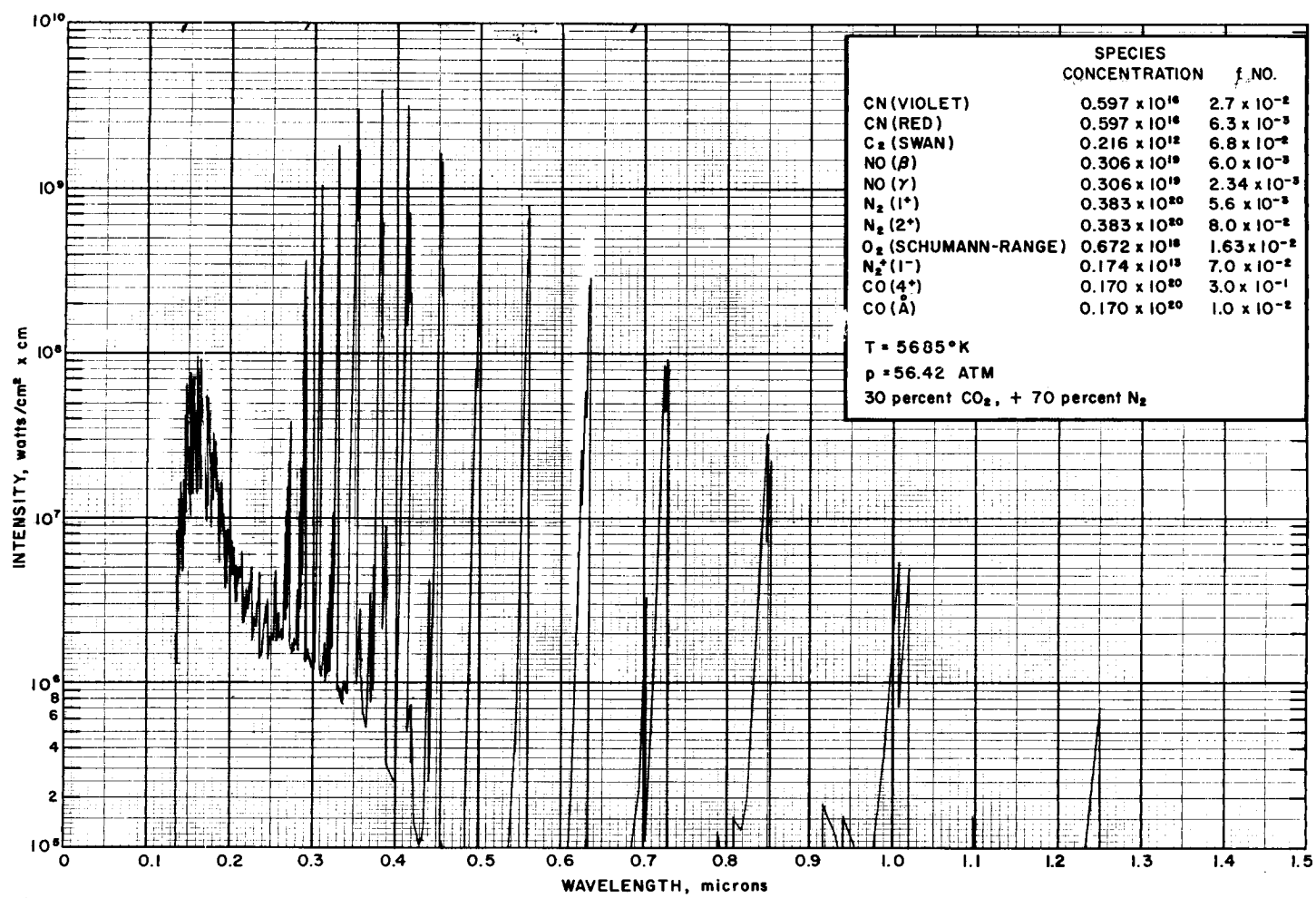


Figure 3b AVCO THEORETICAL SPECTRAL DISTRIBUTION: BALLISTIC
RANGE CONDITION

Shock-tube data 10, 11, 12 indicate that nonequilibrium radiation is a problem at this flight condition. Since the intent was to simulate only the equilibrium radiation experimentally, the test conditions were chosen so that the relative amount of nonequilibrium to equilibrium heating was small. The choice of test conditions is a tradeoff governed by the pressure in the ballistic range. One deciding parameter was the small size of the models, which required high pressures to minimize nonequilibrium effects. Opposing this was the model ablation phenomenon.

The total radiative heat transfer is dependent on the chemical composition, density, and especially the temperature of the radiating gas. Consequently, accurate results are dependent on the accurate simulation of the flow field.

For the flight condition chosen, the major portion of the equilibrium radiation comes from the inviscid flow. Thus, since the concern here is only with the equilibrium radiation, simulation requires matched flow geometry, gas composition, and stagnation enthalpy and pressure. Chemical equilibrium, of course, must also be obtained.

These requirements are generally quite difficult to satisfy. Both the ballistic range and shock tube are capable of simulating the equilibrium radiation. Each facility, however, has limitations in that complete simulation cannot be achieved in either facility alone. The shock tube, for instance, provides the correct enthalpy level, but the test flow has been predissociated by the incident shock. The ballistic range can match all the required parameters, but the data requires scaling over two or three orders-of-magnitude in size, and angle-of-attack-effects cannot easily be obtained.

The simulation procedure chosen was to match stagnation temperature and to scale effects of Mach number, stagnation pressure, and body size.

When the shock-layer radiation is in equilibrium, certain portions of the spectrum may be optically thick (for the Martian type atmospheres, likely candidates are CN violet and CO fourth positive).^{8, 9} For simulation of optically thick radiation, a further requirement is that the typical optical path, $p_{st} \delta$, should match the flight value.

The need for obtaining accurate data at both zero and nonzero angles-of-attack makes it necessary to use the shock tube for the majority of the tests. The shock tube, however, achieves the stagnation temperature and pressure required for simulation by testing in the gas processed by the incident shock, and thus at a lower flow velocity and Mach number than that of free flight. This lower Mach number (approximately 3), and consequent lower shock density ratio, means that the flow geometry, the shock shape in particular, is not well simulated. We can, however, simulate the shock shapes accurately at all angles-of-attack in a shock tunnel, using a gas with a low specific heat ratio, γ . Using CF₄

($\gamma = 1.08$), as the test gas enables us to obtain the hypersonic density ratio (approximately 15) corresponding to free flight in the Martian atmosphere.

The scaling model used considers that the total radiation heat load to the model and the full-scale vehicle can be written

$$W_a \propto V_a \bar{H}_a \quad (4)$$

$$W_c \propto V_c \bar{H}_c$$

where V_c and V_a are the effective radiative volumes of the gas cap, and \bar{H}_c and \bar{H}_a are volumetrically averaged radiation per unit volume. For a particular shape, say the Apollo, the ratio W_c/W_a is

$$\frac{W_{cA}}{W_{aA}} = \frac{V_{cA}}{V_{aA}} \times \frac{\bar{H}_{cA}}{\bar{H}_{aA}} \quad (5)$$

The comparative total heat load for two shapes, say the Apollo and blunt cone is then

$$\frac{W_{cA}}{W_{cC}} = \frac{W_{aA}}{W_{aC}} \times \frac{V_{cA}}{V_{cC}} \times \frac{V_{aC}}{V_{aA}} \left(\frac{\bar{H}_{cA}}{\bar{H}_{aA}} \times \frac{\bar{H}_{aC}}{\bar{H}_{cC}} \right) \quad (6)$$

The ratios W_{aA}/W_{aC} and V_{aC}/V_{aA} are determined from shock-tube data, whereas V_{cA}/V_{cC} is found from the shock-tunnel shock shapes. The averaged intensity ratios between the two configurations are assumed the same for flight and test conditions (see Appendix D), hence the scaling is

$$\frac{W_{cA}}{W_{cC}} = \frac{W_{aA}}{W_{aC}} \times \frac{V_{cA}}{V_{cC}} \times \frac{V_{aC}}{V_{aA}} \quad (7)$$

For scaling absolute intensities to each body shape, rather than comparing the intensities among the body shapes, Equation (5) must be considered in more detail. Since the stagnation temperature is matched, the ratio of radiative flux to the body is (according to Equation 3) proportional to the number density of the radiating species. Consequently, the radiative flux due to a single optically thin band system may be scaled by

$$\left(\frac{J_c}{J_a} \right)_i = \left(\frac{V_c}{V_a} \right) \left(\frac{[N_i]_c}{[N_i]_a} \right) \quad (8)$$

For the total radiation in a given wavelength interval, this would be extended to

$$J_{c_{\text{total}}} = \left(\frac{v_c}{v_a} \right) \sum_i (J_a)_i \left(\frac{[N_i]_c}{[N_i]_a} \right) \quad (9)$$

Because of the questions raised in Section B with regard to the correct number densities and spectral distributions, and because the total radiation over relatively large wavelength intervals was measured, an approximation to Equation (9) was used as the scaling equation. This was

$$\left(\frac{J_c}{J_a} \right)_{\text{total}} = \left(\frac{v_c}{v_a} \right) \left(\frac{\rho_c}{\rho_a} \right)_{\text{stag}} \quad (10)$$

With the above considerations in mind, the assumptions underlying the scaling model are:

1. The gas cap is everywhere in equilibrium.
2. The gas cap is optically thin.
3. The gas cap is geometrically thin; i. e., it lies close to the body (local shock-layer thickness \ll local body radius of curvature).
4. The volumetric averages of intensity have the same ratio for flight and test conditions for all the models.
5. The total spectrally integrated equilibrium radiation can be assessed, using the radiation in the limited spectral region actually monitored during the tests.

Assumptions 1 and 2 are examined in Appendix B and found to be good. Assumption 3 was checked visually by examination of the image converter photographs and was found to be valid for all 0 and 45 degrees angle-of-attach cases (see Figure 18). It is questionable for the shock-tube 90 degree cases because of the relatively small radius of curvature of the model edge which is now the stagnation point. Even this limitation is minor, because most of the radiation at this condition comes from the shock layer on the afterbody.

Assumption 4 is discussed in Appendix D. It was found that assumption 4 is good to within 35 percent for the shock tube and flight conditions, and to within 20 percent for the shock-tube and range simulation.

26

The effect of assumption 5 is probably negligible in assessing the relative merits of the three body shapes, as the tests are all performed at the same nominal condition in each facility. Its effect on the scaling of the radiation cannot be accurately determined, since the relative effect of the neglected radiation (primarily the CO (4+) band system) varies from 21 percent of the total radiation at the trajectory conditions, to 63 percent for the range, and 59 percent in the shock tube (see Figure 2).

We retain these assumptions, however, in spite of the approximate nature of some, for lack of equally tractable ones, keeping in mind that the entire model will be checked by comparing the shock-tubes results with those obtained in the range.

On the basis of this model, the radiation seen per steradian from the front of a body will be twice that seen from the side, and the radiation to the body is proportional to both.

The coupling of the radiation measurements made in the shock tube with the shock shapes obtained in the shock tunnel allows a reasonable prediction for the comparative equilibrium radiation under actual flight conditions (also allowing for body-size variation). This scaling analysis can be checked by comparison with the radiation observed in the ballistic range and with simple theoretical treatments.

III. EXPERIMENTAL PROGRAM

The conditions in the ballistic range and shock tube were chosen to simulate one point on the entry trajectory of a Martian type atmosphere consisting of 30-percent CO₂ + 70-percent N₂ by volume:

$$T = 100^{\circ}\text{K}$$

$$\rho = 5.05 \times 10^{-7} \text{ gm/cc}$$

$$u = 19,600 \text{ ft/sec}$$

These conditions yield a stagnation temperature of 5730°K and a stagnation pressure of 0.17 earth sea-level atmospheres.

The nominal test condition at which all the tests were made in the ballistic range was

$$\rho = 2.63 \times 10^{-4} \text{ gm/cc}$$

$$T = 300^{\circ}\text{K}$$

$$u = 15,900 \text{ ft/sec}$$

$$p = 150 \text{ torr,}$$

yielding a stagnation temperature of 5730°K and stagnation pressure of 56.4 earth sea-level atmospheres.

Similarly, the nominal test condition run in the shock tube was

$$\rho = 8.77 \times 10^{-6} \text{ gm/cc}$$

$$T = 300^{\circ}\text{K}$$

$$u = 3.655 \text{ mm}/\mu\text{sec}$$

$$p = 5 \text{ torr,}$$

yielding a stagnation temperature of 5730°K and a stagnation pressure of 12.2 earth sea-level atmospheres. As mentioned in the previous section, the stagnation temperature is the most important thermochemical variable, and the experiments were run with the aim of achieving a constant stagnation temperature for all cases, while the pressure was varied. The pressures were chosen to ensure that the radiation in the shock tube and ballistic range was primarily equilibrium (see Appendix B).

In addition, a series of shock tube tests at four other initial pressures were run to investigate the effects of pressure on the radiation. The shock tube test conditions are summarized in Table I, and the models are shown in Figure 13.

TABLE I
SHOCK TUBE TEST MATRIX AND NOMINAL CONDITIONS

| | Angle-of-Attack (degrees) | Initial Pressure (torr) | Incident Shock Velocity (mm/μsec) | Stagnation Temperature (°K) | Stagnation Pressure Atmospheres |
|---|------------------------------|----------------------------|--------------------------------------|--------------------------------|------------------------------------|
| Tension Shell | 0 | 5.0 | 3.655 | 5730 | 12.2 |
| " | 45 | 5.0 | " | " | " |
| " | 90 | 5.0 | " | " | " |
| Modified Apollo | 0 | 5.0 | " | " | " |
| " | 45 | 5.0 | " | " | " |
| " | 90 | 5.0 | " | " | " |
| 60-Degree Blunt Cone | 0 | 5.0 | " | " | " |
| " | 45 | 5.0 | " | " | " |
| " | 90 | 5.0 | " | " | " |
| " | 0 | 1.0 | 3.762 | " | 2.8 |
| " | 0 | 2.5 | 3.722 | " | 6.5 |
| " | 0 | 7.5 | 3.636 | " | 17.8 |
| " | 0 | 10.0 | 3.618 | " | 23.2 |
| 60-Degree Blunt Cone with Fiber Optics | 0 | 5.0 | 3.655 | " | 12.2 |

IV. EXPERIMENTAL FACILITIES AND PROCEDURE

The experiments which were used to obtain total equilibrium radiation were performed in three Avco Space Systems Division facilities:

1. The 100-foot-long ballistics range equipped with a caliber 0.600, two-stage hydrogen gas gun,
2. The 6-1/2 inch inside diameter (i. d.) combustion-driven shock tube, and
3. The 20-inch diameter test section shock tunnel (used in the tailored interface mode), capable of Mach 18 in air.

A. BALLISTICS RANGE

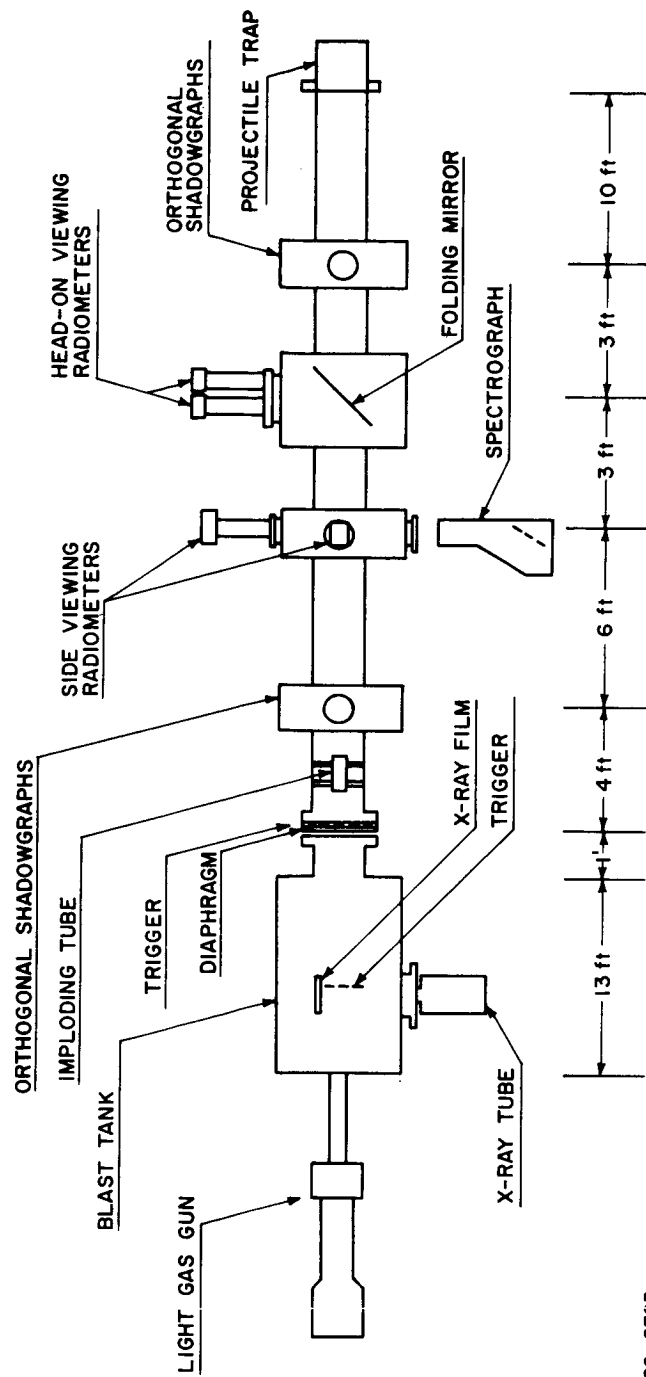
The range and its pertinent instrumentation are shown schematically in Figure 4. The light gas gun was used to accelerate the model and sabot. A rifled launch tube was used to spin-stabilize the model package at approximately 1600 revolutions per second. The models used were constructed of solid aluminum, one-quarter-inch in diameter, with cylindrical afterbodies. These models had the same frontal shapes as those used in the shock-tube and shock-tunnel experiments, except for a shoulder radius of 0.03 inch to avoid ablation. A photograph of an earlier version of the tension shell model (not used in the tests) and its sabot are shown in Figure 5.

The entire ballistics range was initially evacuated to below 1 torr, and then filled with the required 70-percent N_2 + 30-percent CO_2 mixture at the test condition of 150 torr and room temperature.

After firing, the model left the launch tube and passed into the blast tank, wherein the hydrogen cooled and decelerated along with any extraneous particles such as shear disc and piston fragments. The sabot petals separate and impact baffles in this blast tank.

During the initial tests, a flash X-ray photograph of the model was taken 3 feet from the muzzle to monitor sabot separation and model orientation and integrity. When the models were flying properly, this station was no longer used.

A side-looking photomultiplier monitored the arrival of the model at the end of the blast tank. After an appropriately set delay, a pulse from this photomultiplier fired a 1-1/2 inch imploding tube, through which the model left the blast tank, which closed in 40 μ sec, preventing any spurious particles and gun gases from following the model into the test section.



86-8723

Figure 4 BALLISTIC RANGE SCHEMATIC

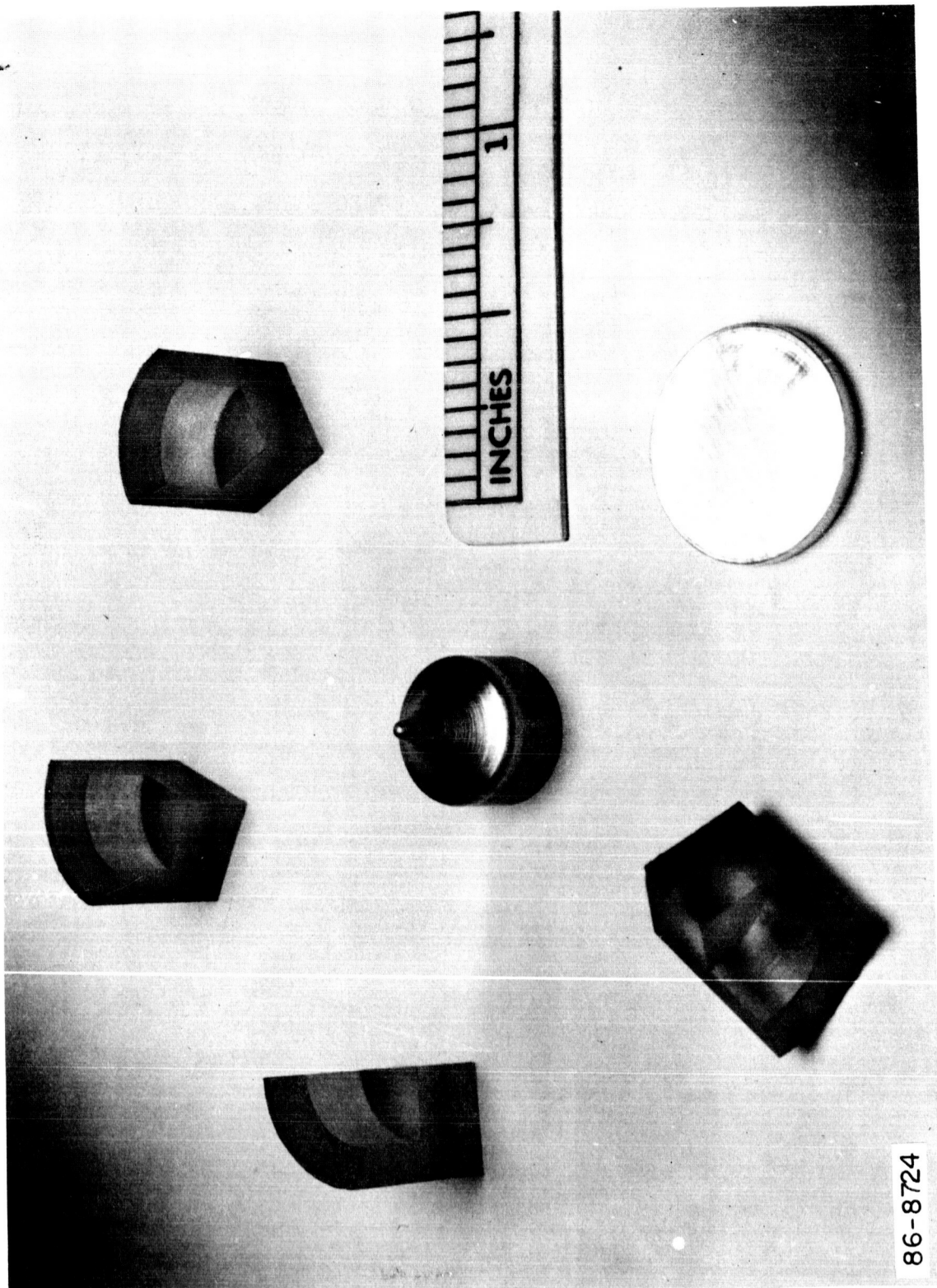


Figure 5 PHOTOGRAPH OF TENSION SHELL MODEL AND SABOT

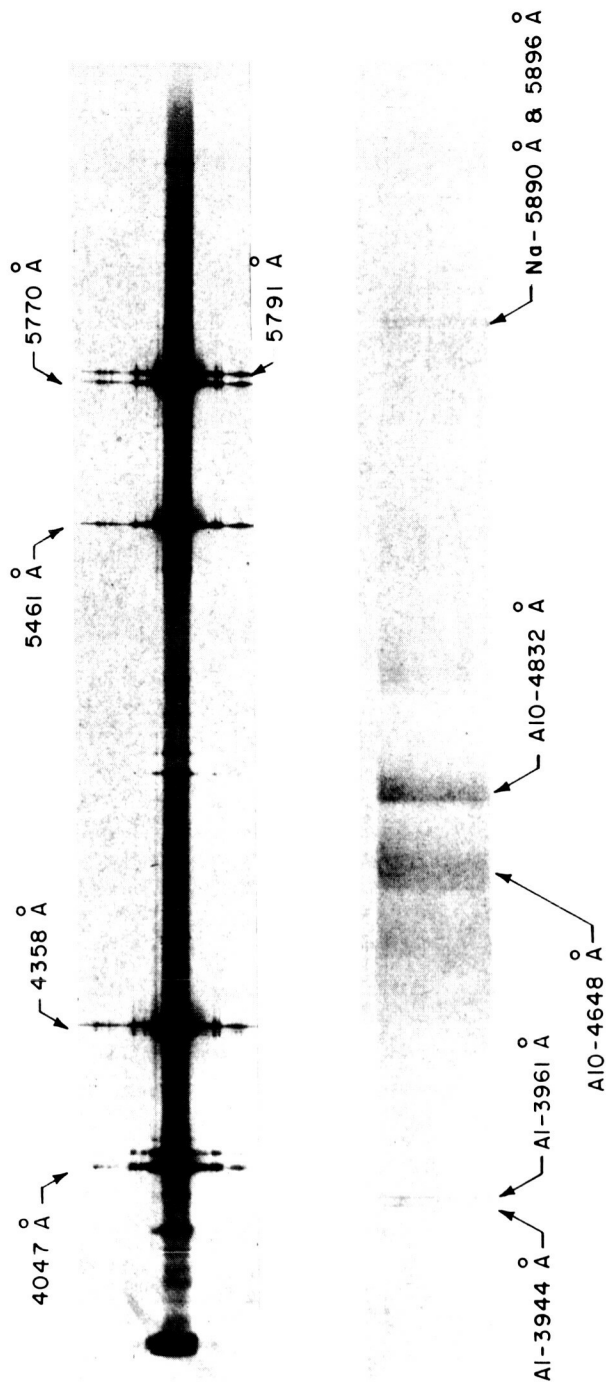
Upon entering the test section, the model was photographed at a set of orthogonal shadowgraph stations to determine its angle-of-attack. The root mean square (rms) angle-of-attack for all shots was 1.5 degrees. The model then passed through the field-of-view of a spectrograph which was used to determine if the projectile was ablating or if any other contaminant was radiating significantly. The Avco-made spectrograph had an f-9 optical system and used a diffraction grating as the dispersive element to view a spectral range from 3000 to 6500 Å. The recorded spectra were developed and examined to determine the presence or absence of atomic aluminum lines or aluminum oxide band heads (see Figure 6). This was a criterion for determining whether or not the model was ablating. Moreover, since the spectrographic plate was exposed to radiation from the test section for about 1 minute, both prior to and subsequent to the passage of the projectile, it provided a very conservative check on the presence of any spurious radiation. Each plate was calibrated immediately prior to firing with a mercury source to ensure accurate wavelength determination from the plates.

The gas cap radiation was measured by two wideband radiometers viewing the projectile head-on. This was accomplished by the use of an aluminized mylar mirror, as shown in Figure 7. The oscilloscopes began monitoring the radiation when the model was approximately 6 feet upstream of the folding mirror and ended upon impact of the model with the mirror. A sharp rise in light level indicated the moment of impact, thus providing a time reference mark from which the axial position of the model was determined prior to impact.

The model's speed was determined using a 10-Mc counter started by the photomultiplier pulse which triggered the imploding tube and photographed the model at the first shadowgraph station, and stopped by the pulse which triggered the second shadowgraph unit. The average velocity thus coincided with a station 3 feet upstream of the folding mirror. An estimate of the effect of drag on the velocity (assuming that the drag force was equal to the stagnation pressure multiplied by the frontal area, and for a mass of 1.8 grams) showed that the velocity decreased by 0.3 percent per foot for a nominal velocity of 15,500 ft/sec. A second independent velocity measurement was made from the elapsed time between the detection of the model at the first shadowgraph station and the time of arrival at the folding mirror.

The output signals from the radiometers were fed into Tektronix oscilloscopes and recorded photographically. Typical records are shown in Figure 8. The output signal is logarithmic to ensure that no test data are lost because of the trace going offscreen. The reduced data should show a $\frac{1}{t^2}$ dependence, since the model has a nearly constant velocity and the radiation incident on the photo tube varies as $1/r^2$, where r is the distance from model to photo tube.

Hg SPECTRA



86-8725

Figure 6a BALLISTIC RANGE SPECTRUM: ABLATING MODEL

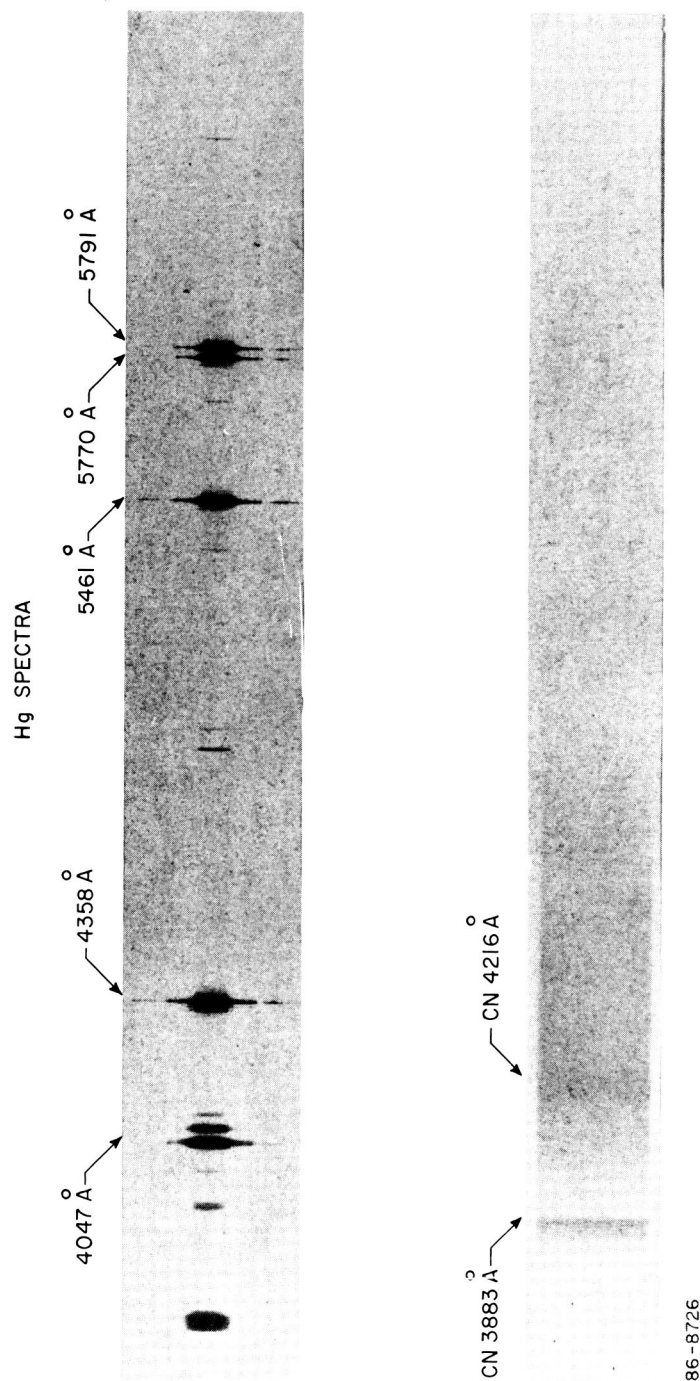


Figure 6b BALLISTIC RANGE SPECTRUM: NONABLATING MODEL

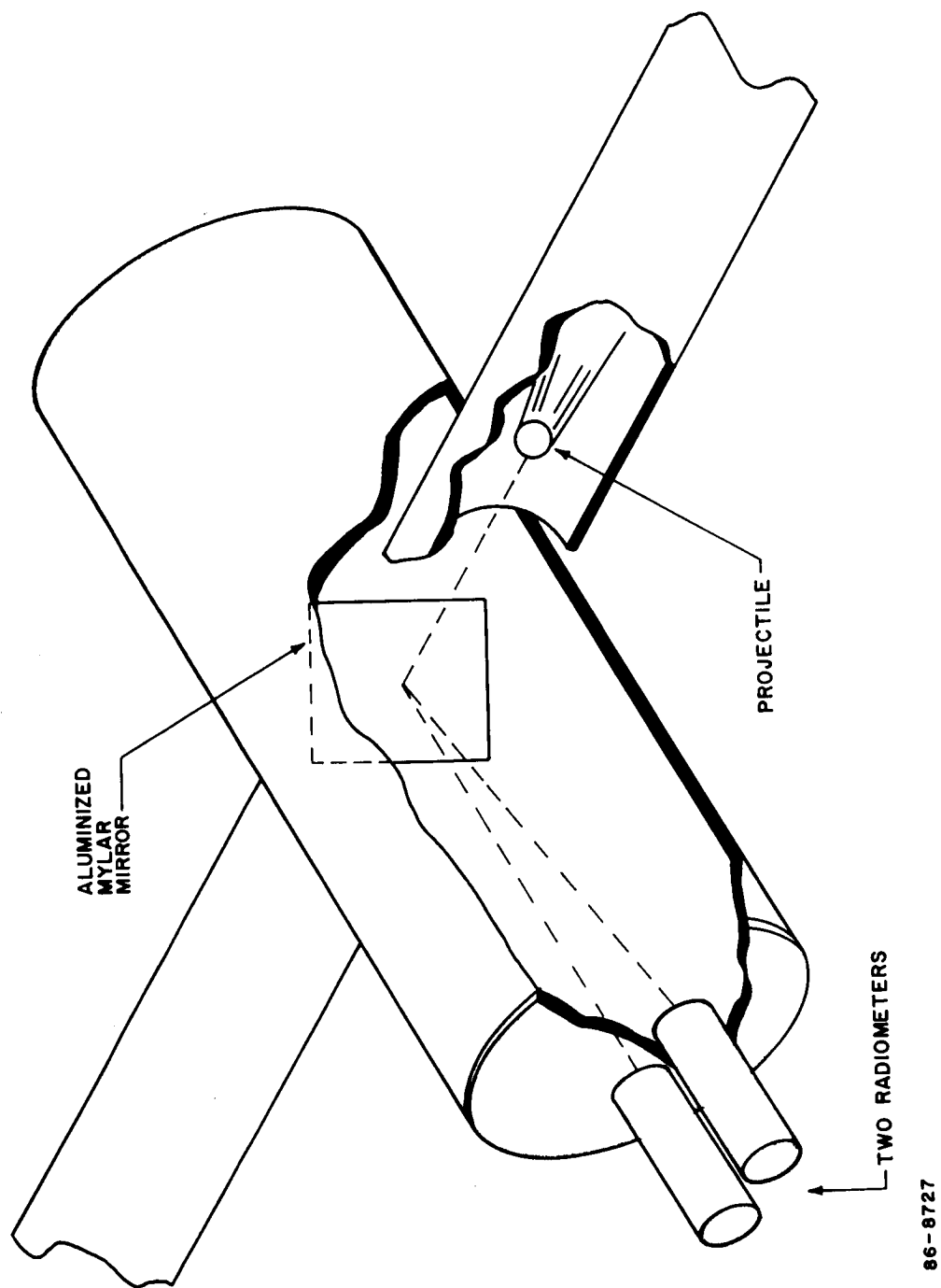


Figure 7 HEAD-ON MEASUREMENT SCHEMATIC

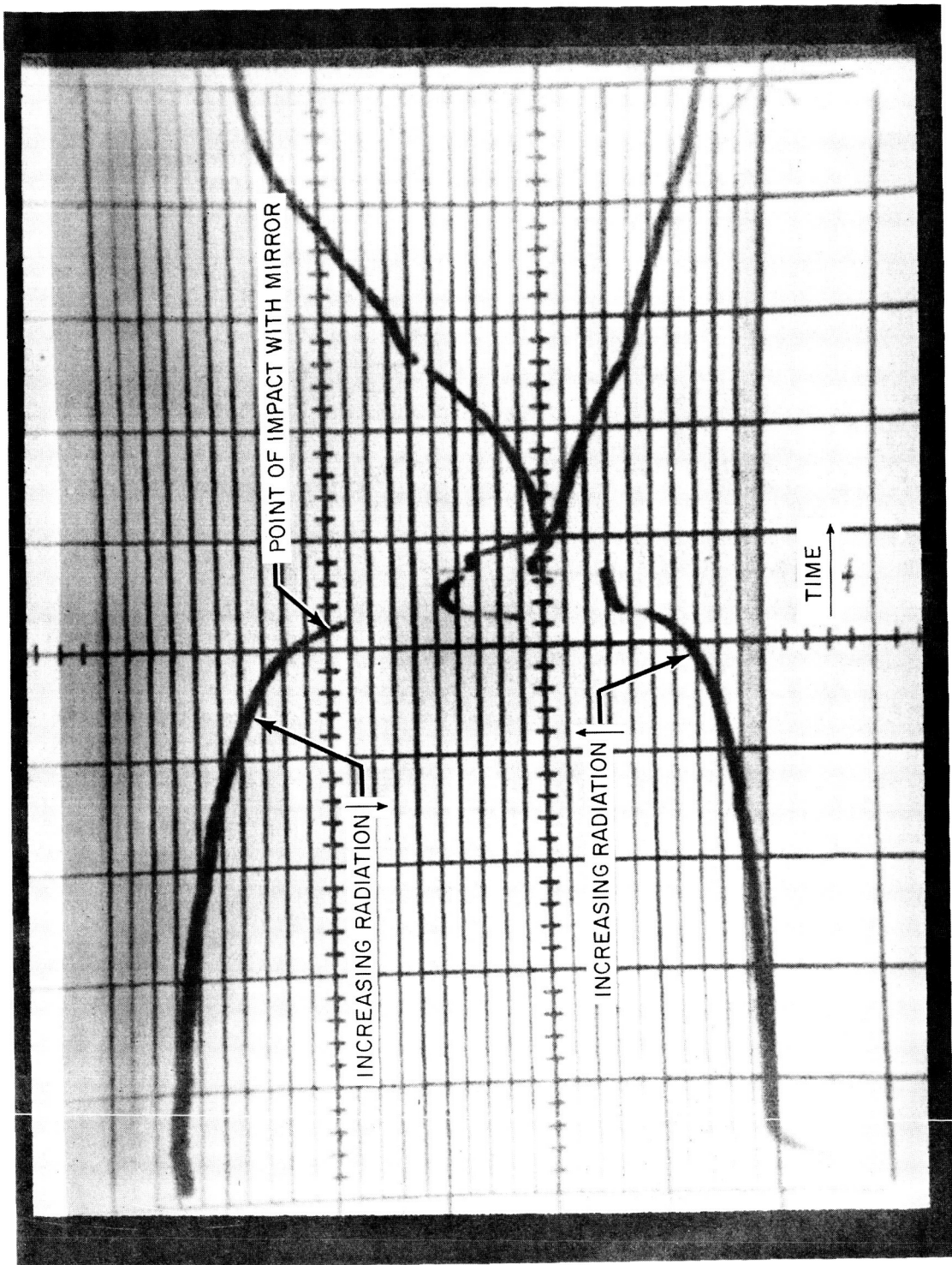


Figure 8 OUTPUT OF RADIOMETERS VIEWING THE APPROACHING
MODEL HEAD-ON

B. SHOCK TUBE

The 6-1/2-inch i.d. combustion-driven shock tube (Figure 9) consists of three 9-foot-long sections, a 2-foot-long test section, and a 2-foot-long vacuum coupling section joined to a 5-foot-long 1-1/2-inch i.d. driver by a 30-inch-long conical transition section. The test section was located between the second and third driven sections, yielding a nominal flow duration of approximately 120 μ sec at the test condition, with no interference from the reflected shock. A flushing action was achieved in the setting of the initial pressure by filling from the manifold near the transition section and evacuating the tube through the vacuum coupling section at the downstream end. This procedure was initiated after the entire shock tube and manifold system had been evacuated to at least 5×10^{-4} torr.

Shock speeds were measured using ionization gages at four stations upstream, one downstream, and one in the test section, 4 inches ahead of the model. The output of the gages was fed into and displayed on a time-mark folded oscilloscope sweep (Tektronix 535A), driven by a Radionics (model TWN-2A) triangular waveform and timing marker generator. Shock transit times were measured to ± 1 percent, yielding an uncertainty of 7 percent in the total radiation.

Total, over-the-body, radiation was monitored by two appropriately filtered photomultipliers (similar to those used in the ballistics range study) viewing the entire test section. A TRW Systems Image Converter Camera, used in the framing mode, monitored the flow over the model at suitable intervals after the establishment of a steady flow and was used to obtain shock shapes. The shock tube and optical layout are shown in Figures 9 and 10. The ionization gage directly upstream of the model triggered two Tektronix 555 dual-beam oscilloscopes into which the output of the photomultipliers was fed. The gate from one of the scopes was taken and suitably delayed through an S.T.L. Trigger delay generator, and used to pulse the image converter after a predetermined delay.

Avco-made spectrograph, similar to that used in the ballistics range study, was used intermittently to determine whether the test slug was being contaminated by shock-tube ablation products and other impurities generated in the combustion driver. A mechanical brushing procedure was used to clean the shock tube between each series of runs to ensure cleanliness.

Typical output signals from the two radiometers are shown in Figure 11. The upper trace monitors the image converter camera, with the spikes indicating the instant at which each of the three frames are taken. The photomultiplier signal shows the small increase in light level as the shock traverses the test section, indicating the increase of light intensity as more of the shocked gas is visible by the detectors. Then, the intensity peaks and decays as the incident shock passes over and partially reflects from the model, and the bow shock forms and the flow becomes steady. The level portion is indicative of the steady state, and as such was used to obtain the equilibrium radiation data.

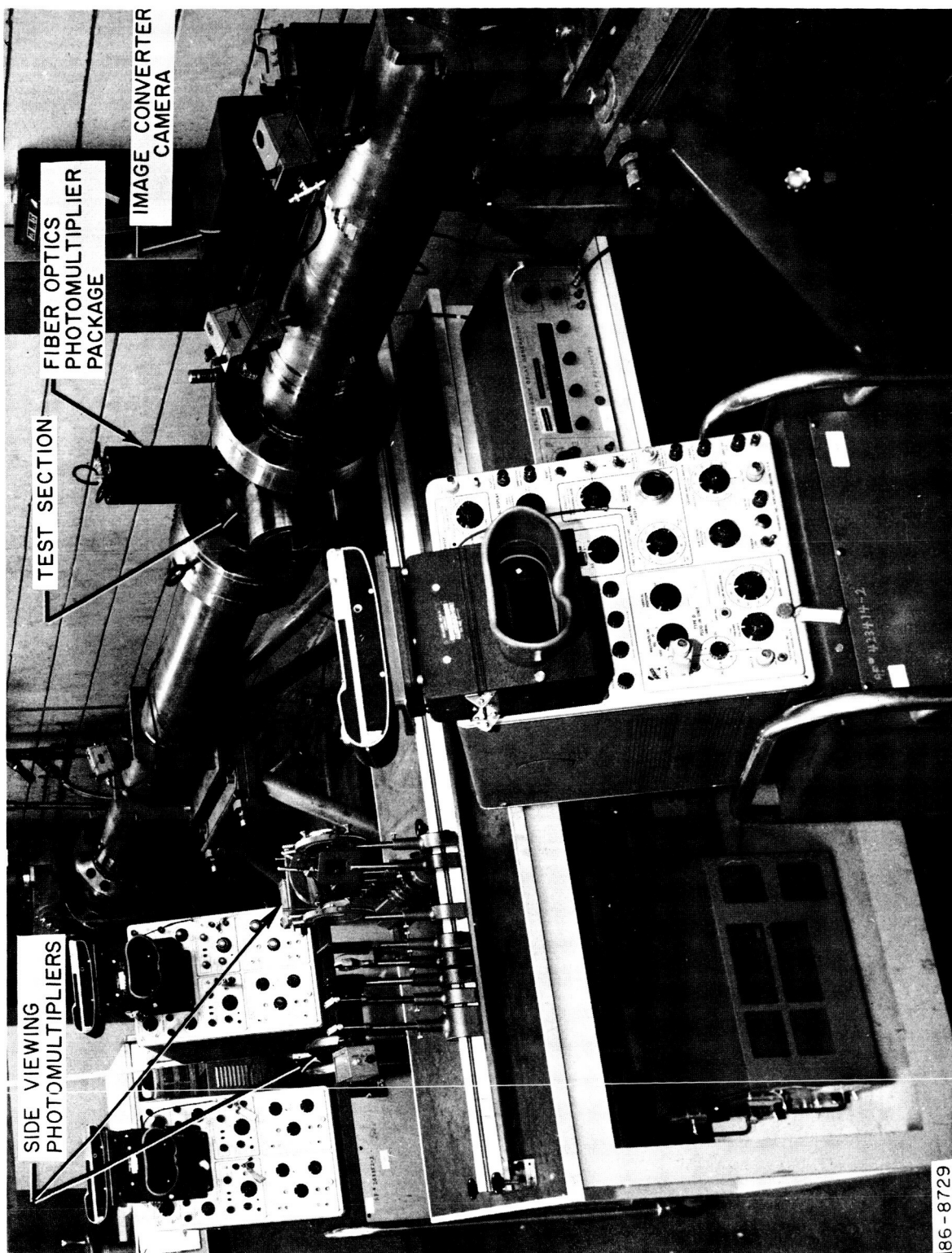
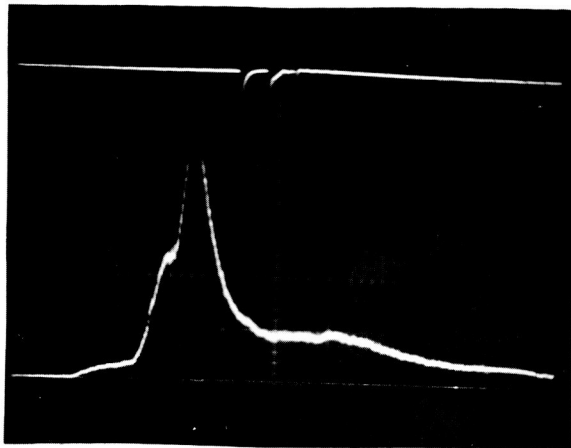
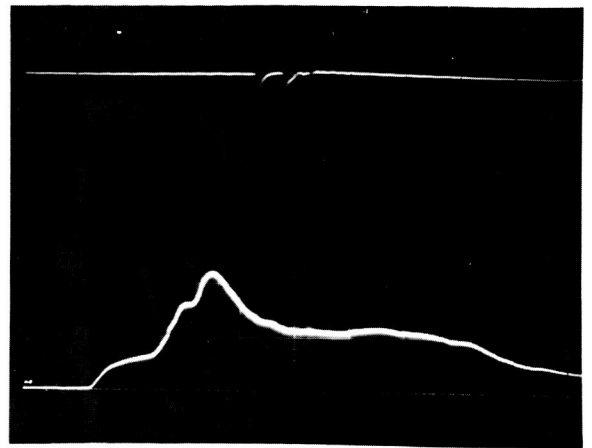


Figure 9 6-1/2-INCH COMBUSTION-DRIVEN SHOCK TUBE



S-II
10 mv/cm 20 μ sec/cm



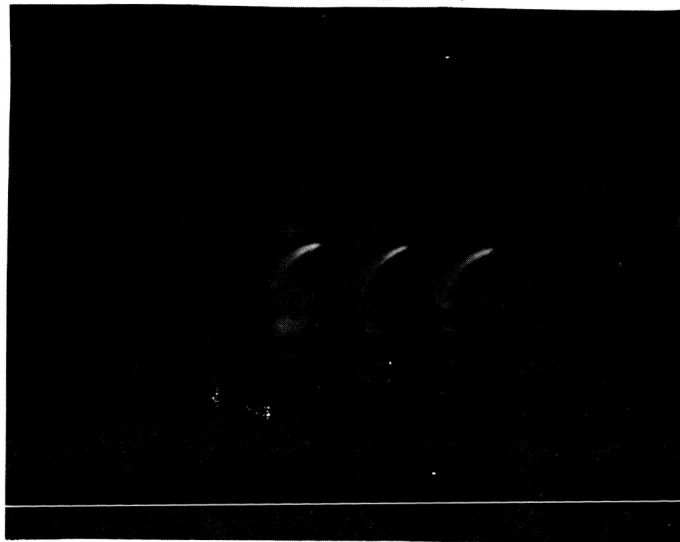
S-I
5mv/cm 20 μ sec/cm

RUN NO. 144

$p_1 = 4.85$ mm Hg $U_s = 3.61$ mm/ μ sec

MODIFIED APOLLO , $\alpha = 45$ degrees

3 2 1



86-8731

Figure 11 TYPICAL SHOCK-TUBE DATA

The data reduced for each run were scaled to account for the slight variations from the nominal test condition using the pressure and velocity variation of the radiation for this mixture as determined by previous studies.^{2, 11, 12}

C. SHOCK TUNNEL

Schlieren pictures of the shock wave about the models at high Mach number and angle-of-attack were obtained in the 20-inch test section shock tunnel. This tunnel is capable of Mach 18 in air, but due to the need to simulate the required low adiabatic exponent, γ , corresponding to the equilibrium decomposition of the model Martian atmosphere, the tests were conducted in pure CF_4 .

The tunnel had a maximum possible area ratio of 10^4 , with typical tailored reservoir conditions of $p = 12,000$ psia and $T = 1900$ K. The pitot pressure measured during one run was 1.5 psia. An equilibrium nozzle program²⁰ was run at these reservoir conditions, but yielded answers only until the gas was expanded to a pitot pressure of 5.0 psia, due to program limitations, corresponding to a Mach number of 5.80 and a shock density ratio of 14.36. Thus, the flow being in the hypersonic regime for CF_4 , with a density ratio comparable to that for the entry condition (15.5) chosen for the model Martian atmosphere, resulted in a well-simulated shock shape.

D. DATA ACQUISITION AND REDUCTIONS

The shock-layer gas radiation in both the ballistic range and shock tube was measured by two wideband radiometers. One radiometer consisted of an S-1 response RCA No. 7102 photomultiplier and a Corning 3-70 glass filter (4800 Å - 13,000 Å), while the other radiometer has an S-11 response RCA No. 6199 photomultiplier and a Corning 5-57 filter (3400 Å - 5600 Å). Appropriate neutral density screens and Kodak neutral density filters were used to reduce the total light level input to the face of the photomultiplier tube. The transmission of all filters and of the window was measured on a Cary recording spectrograph. The final spectral response of the radiometers, including all filters is shown in Figure 12.

The need for an accurate determination of the true spectral distribution of the radiation necessitated taking a photograph of the spectrum shown in Figure 6. The CN (violet) band system is quite prominent, and no other band system is observable above the background. This agrees qualitatively with the spectral distribution determined experimentally by Thomas and Menard¹⁰ for this mixture at approximately the same temperature in a shock tube. On the basis of this result, the Ames distribution was used in obtaining absolute intensities from the experimental measurements, as it resembled the experimental spectra more than did the Avco distribution. Absolute intensities are required only for the scaling portion of this investigation, not for the relative comparison of the radiation in the shock tube. For this latter portion, therefore, the equivalent blackbody intensity (Equation A4 of Appendix A) was used.

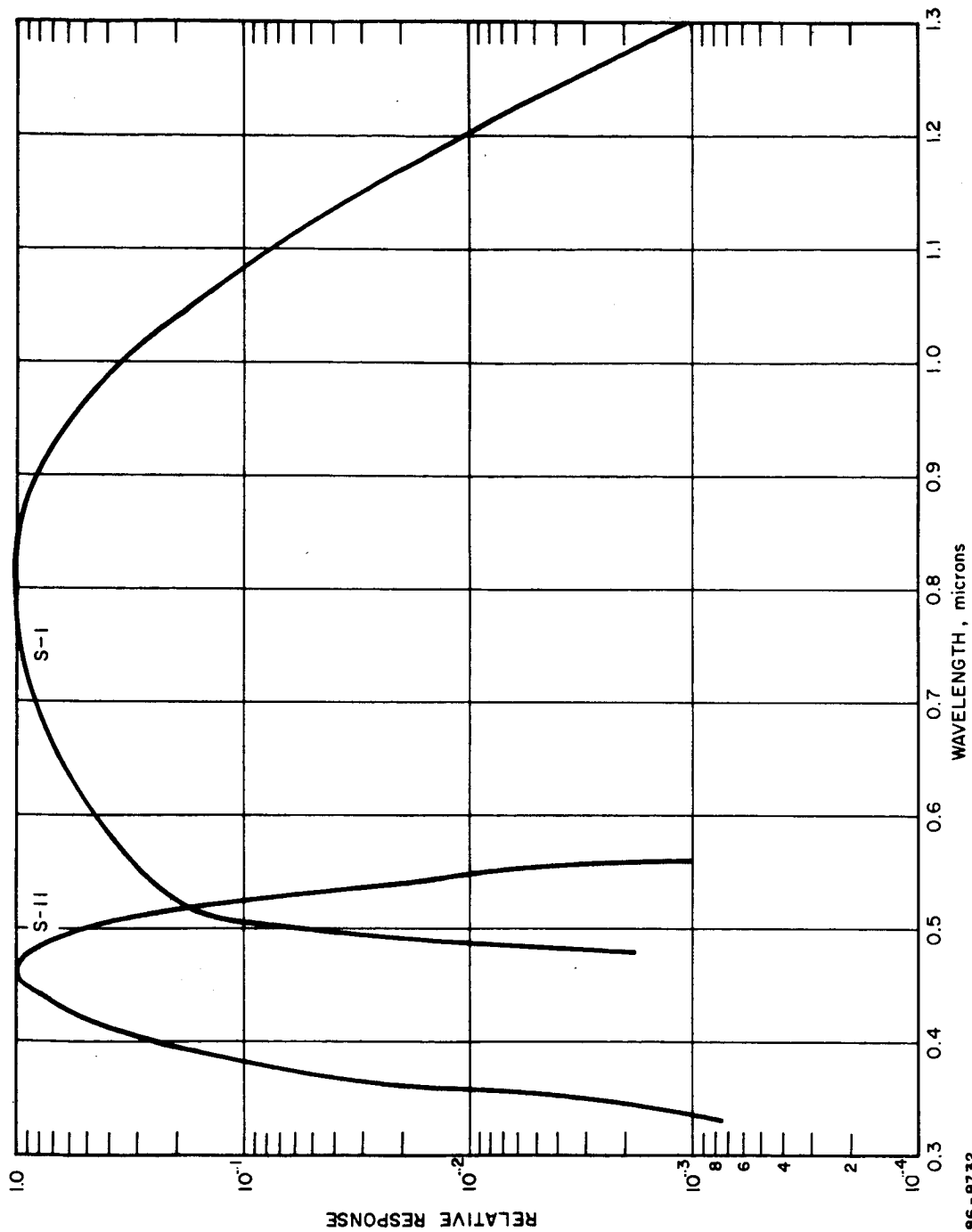
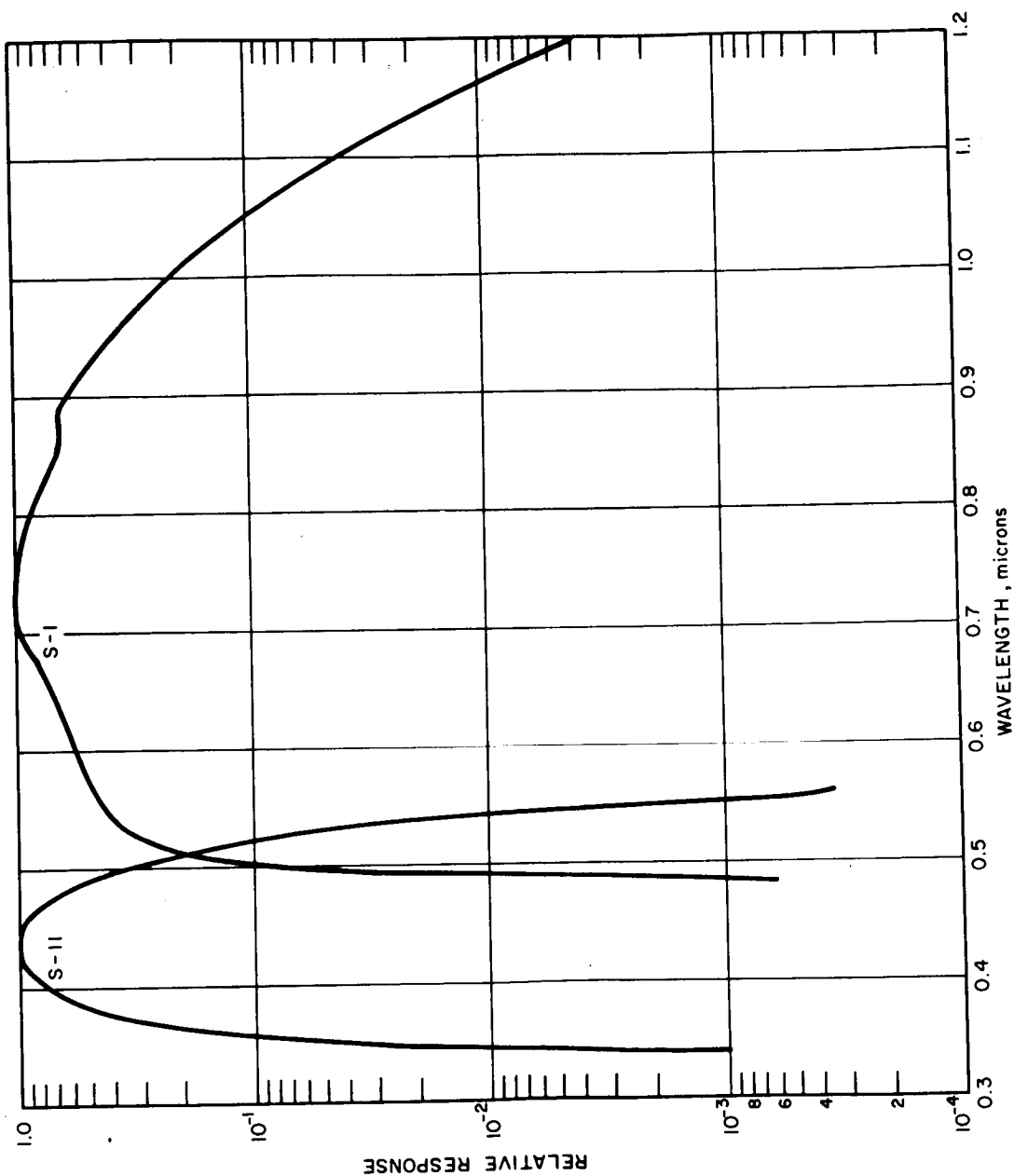


Figure 12a SPECTRAL RESPONSE OF ENTIRE SHOCK-TUBE OPTICAL SYSTEM

86-8732



86-8733

Figure 12b SPECTRAL RESPONSE OF ENTIRE BALLISTIC RANGE OPTICAL SYSTEM

The calibration and data reduction procedures which make use of these response functions are described in Appendix A of this report.

Figure 13 shows the three models and their holder used in the shock tube and shock tunnel experiments.

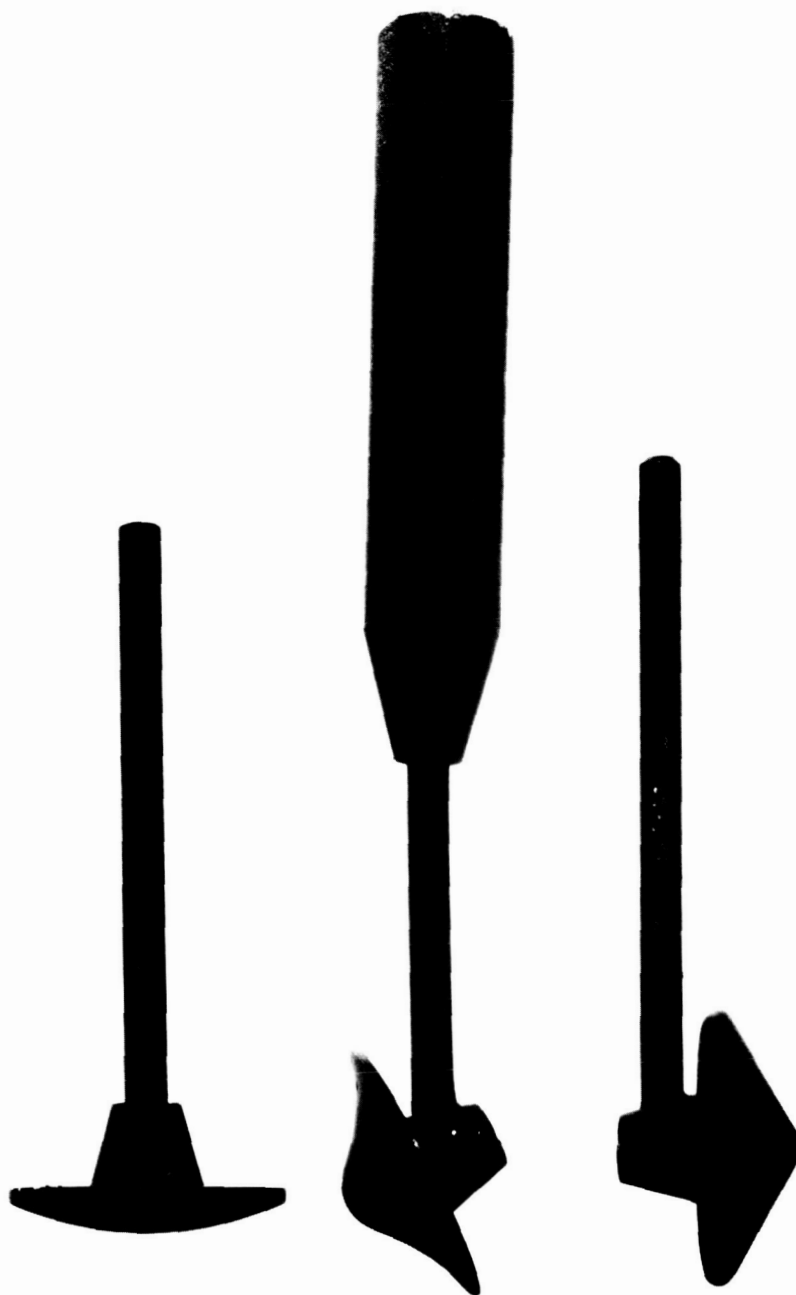
E. INSTRUMENTED SHOCK TUBE MODEL

Several runs were made at zero angle-of-attack with a blunt-cone model instrumented at four radial locations with plastic fiber optical bundles. The Crofon™ Light Guides (made by duPont), of which the fiber bundles were constructed, consisted of a core of Lucite polymethyl methacrylate sheathed with a transparent polymer of lower refractive index. Each 10-mil diameter plastic fiber strand, however, had only a 0.001 in.² cross-sectional area for light transmittance. The bundles consisted of 29 or 30 fiber strands cemented at the ends in a 1/8-inch diameter 1-1/2-inch-long brass tubing, and enclosed in a No. 13 Alphlex black plastic tubing. The brass tubing was brazed into the model so that the fibers were flush with the body surface: (a) at the stagnation point, (b) half-way aft of the apex, (c) at the shoulder of the model, and (d) in the base of the cone, half-way between the shoulder and the axis (see Figure 14). The tubing containing the fiber strands was taken outside the shock tube through a strut whose cross section was in the shape of a diamond airfoil. The brass tubing ends were then glued into appropriate mounting holes in a plate which acted as the support for the photomultiplier instrument package and as a vacuum seal to the shock tube (see Figure 9).

A calibration curve showing the response of a fiber bundle as a function of the angle of incident radiation is shown in Figure 15. Because of the rapid decrease in response as a function of the angle of incident radiation, a rectangular function response with angle was assumed:

$$\text{response} \begin{cases} = 1, & -5 \text{ degrees} \leq \theta \leq +5 \text{ degrees} \\ = 0, & |\theta| > 5 \text{ degrees} \end{cases}$$

A spectral transmission curve of Crofon light guides, supplied by duPont, is shown in Figure 16. This transmission curve, in conjunction with the S-1 spectral response of the RCA 7102 photomultiplier tube was used to calibrate the fiber bundles in situ in accordance with the procedure given in Appendix A. Traces from a run are shown in Figure 17.



86-8734

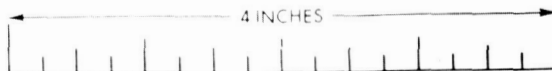


Figure 13 MARTIAN ENTRY BODY-SHAPE TEST MODELS

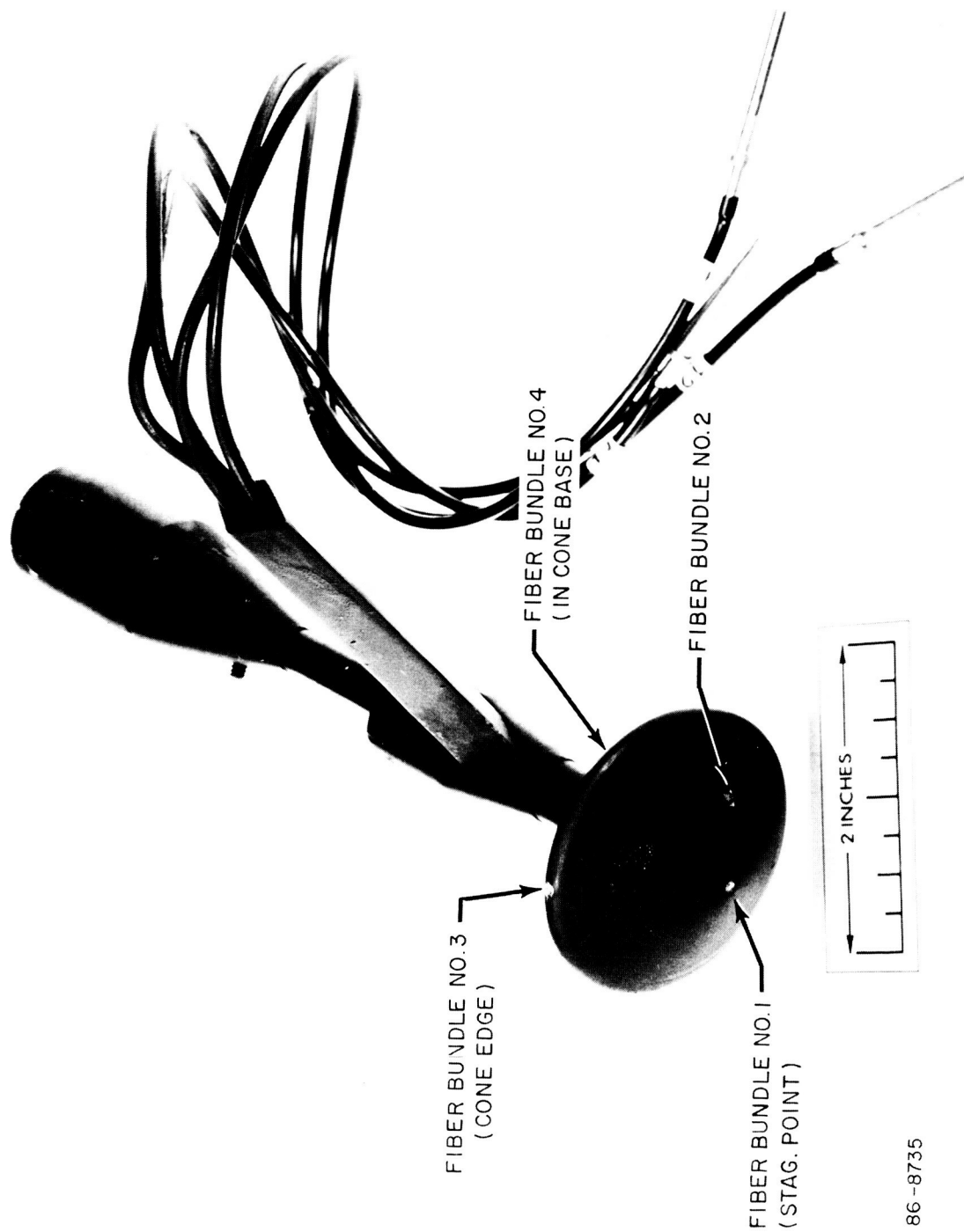


Figure 14 INSTRUMENTED 60-DEGREE HALF-ANGLE BLUNT CONE

86-8735

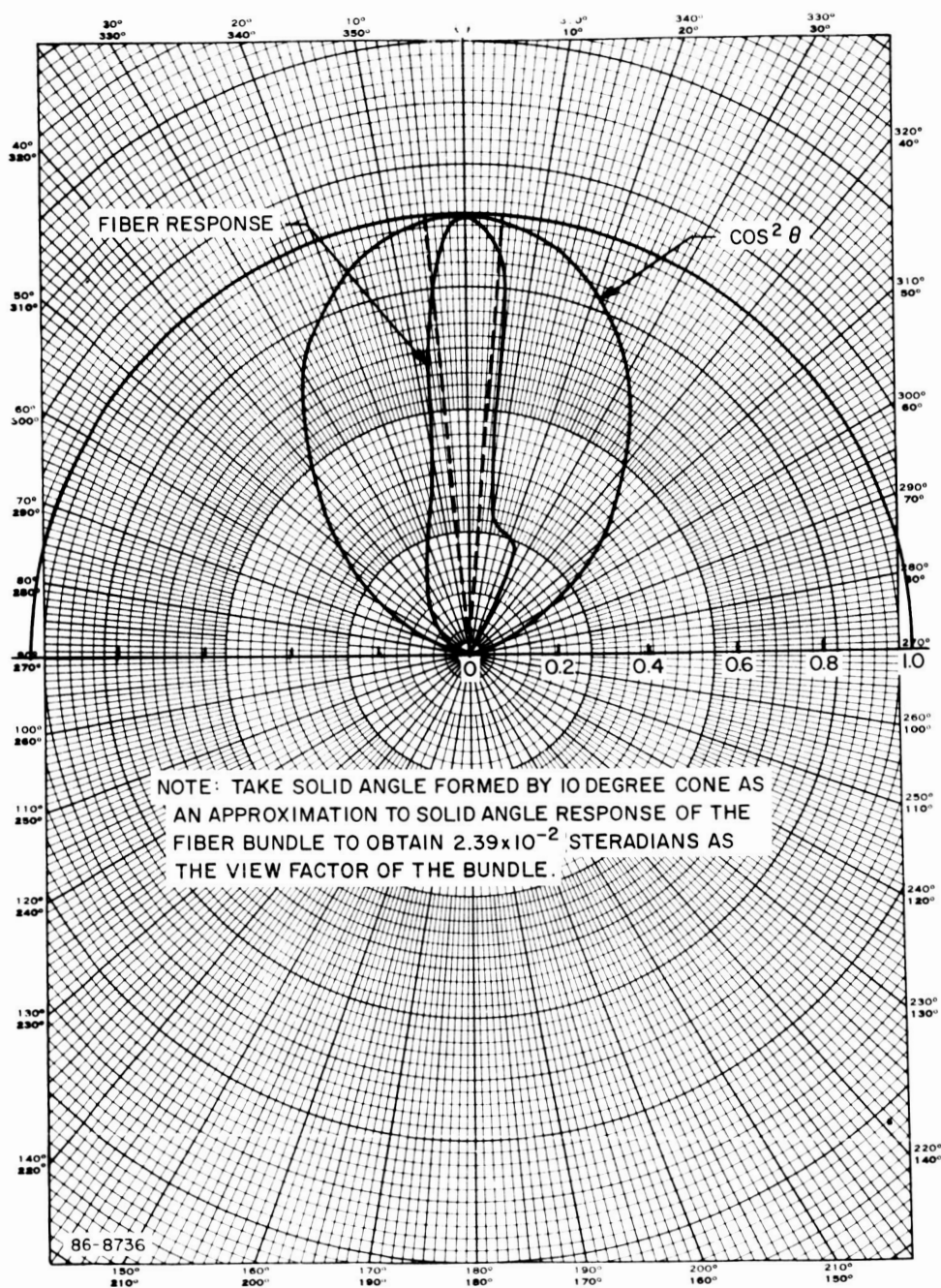


Figure 15 ANGULAR CALIBRATION OF FIBER BUNDLES

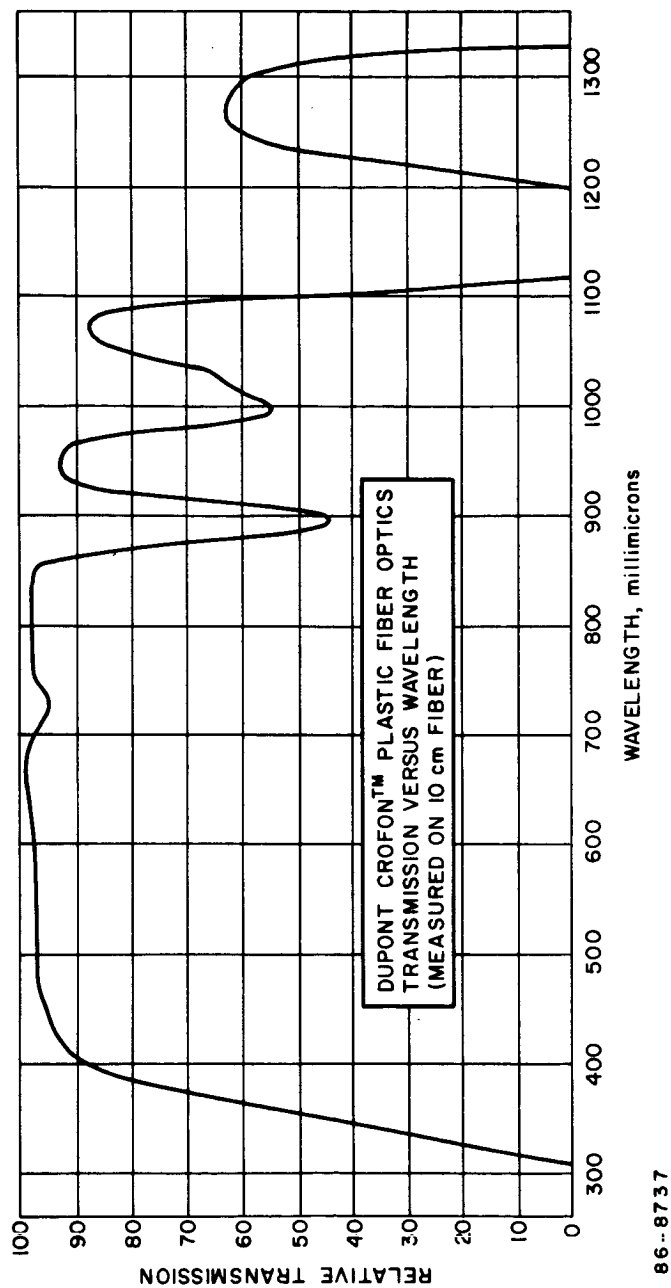
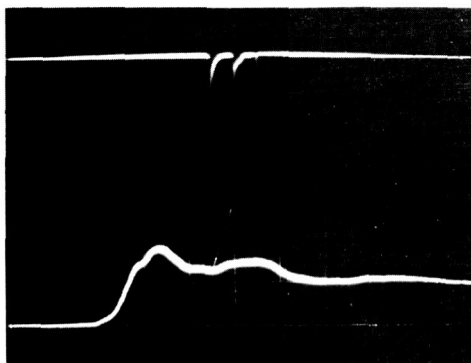
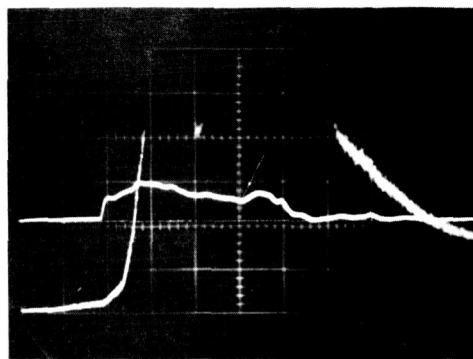


Figure 16 SPECTRAL TRANSMISSION OF CROFON PLASTIC FIBER



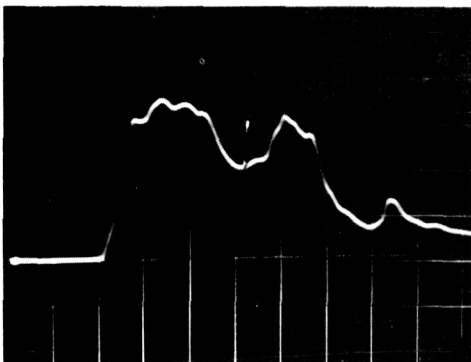
TOP: MONITOR FROM IMAGE CONVERTER;
20 μ sec/cm

BOTTOM: S-I RADIOMETER, SIDE VIEW
5 mv/cm 20 μ sec/cm

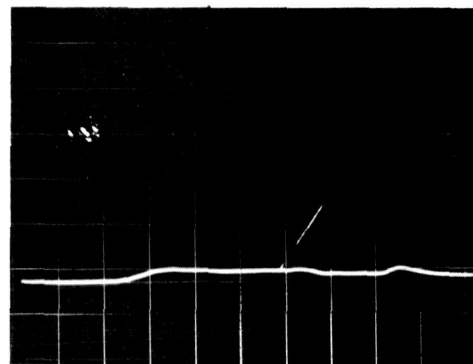


TOP: FIBER NO. 1, 200 mv/cm 20 μ sec/cm

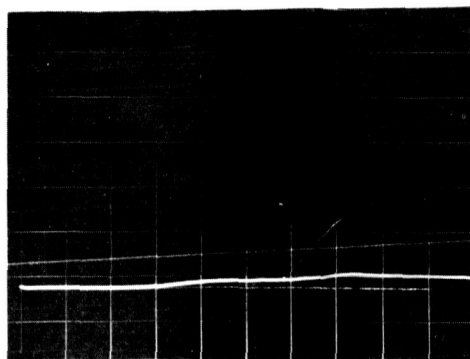
BOTTOM: S-II RADIOMETER, SIDE VIEW
5 mv/cm, 20 μ sec/cm



FIBER NO. 2; 100 mv/cm 20 μ sec/cm



FIBER NO. 3; 200 mv/cm 20 μ sec/cm



FIBER NO. 4; 200 mv/cm 20 μ sec/cm

86-8738

Figure 17 FIBER OPTICS DATA; RUN NO. 183

V. ERROR ANALYSIS

It is of importance to obtain an estimate of the errors involved in this investigation in order to determine the maximum probable error in the measurements and in the final radiation prediction.

A. SHOCK-TUBE TESTS

There are several probable sources of error, both in the measurement and data reduction, and in the scaling analysis.

The maximum probable error in measurement and data reduction can be estimated by reviewing the experimental setup. The error in calibration of the optical system is estimated as ± 3 percent, but the scatter in the day-to-day calibration constants is as high as 25 percent. This is due to experimental difficulties in aligning the tungsten filament lamp at the precise location corresponding to the stagnation point of the model. The probable error in data reduction is estimated as ± 5 percent. There are, however, other sources of error in the measurements arising from the tests themselves; that is, the tests were taken to be at a certain measured pressure and shock velocity in a gas of given composition. As discussed in Section IV, the ± 1 -percent scatter of the shock velocity implies a ± 7 -percent scatter in the radiation data. The initial gas pressure has a ± 2 -percent possible error estimated from the 0.1-torr scale divisions at the 5-torr nominal pressure (at the other test pressures, this error will be directly proportional to the nominal test pressure). The effect of contaminants is estimated as having the same effect as the error in the initial pressure and is found from the leak rate (10^{-3} torr per minute) and the time required to set up a test (~ 5 minutes) to be 0.1 percent. This is negligible compared to the other sources of error. The initial gas composition may be in error by ± 1 percent, taken directly from the Matheson Company quotation.

The error in the gas pressure implies a ± 2 percent possible error in the radiation, since the radiation is linearly dependent on the pressure. The effect of the error in composition is more difficult to assess, since it depends on the equilibrium composition. A conservative estimate, based on an ideal 2-body dissociative process, is ± 2 percent. This variation affects the radiation exactly as does the pressure effect.

Assuming that all possible sources of error are small and that they arise independently; i.e., $Y = Y(X_1, X_2, \dots, X_n)$, leads to the determination of the total probable error from

$$Y = \left[\sum_{i=1}^n (\Delta X_i)^2 \right]^{1/2} \quad (11)$$

as being ± 9.5 percent if the 3-percent error in calibration is used in the above equation, or as 27-percent scatter if the 25-percent scatter in the calibration constant is used.

B. RANGE TESTS

The probable error in the ballistic range tests is also found from Equation (11). All the sources of error present in the shock-tube tests are present in the range tests, and their estimated magnitudes are the same for all sources except that due to the initial pump down procedure and leak rate. The range was evacuated only to 1 torr prior to loading and the leak rate was 1 torr per minute. The time required to fill the range to the 150 torr initial pressure and fire the gun was a maximum of 2 minutes. The error due to contaminants is thus 2 percent. Additional possible sources of error in the range tests enter due to the 0.3-percent per foot effect of drag on the velocity (7 percent on the radiation over a 3-foot section), ablation effect (found to be nil from the spectra taken during each test), and angle-of-attack effect. The rms angle of attack for all shots was 1.5 degrees; its effect on the radiation is estimated as 0.2-percent using a $\cos^6 \alpha$ dependence of the radiation on the angle-of-attack. This is not strictly correct, since this dependence on angle is an approximation¹ to the decay of the radiation along a hemispherical nose.

Again, assuming that all possible sources of error are small and independent leads to a value for the total probable error of ± 10 percent, with the scatter still within 27 percent.

C. SCALING ANALYSIS

The above error analysis has considered only the probable errors entering into the radiation measurements. As far as the accuracy of the radiation scaling prediction is concerned, additional sources of error enter first through the subjective choice of the radiating volumes, and secondly through their measurement. The error in measurement of the volumes is estimated as 20 percent (due to a 10-percent maximum probable error in the measurement of the shock standoff distance at the stagnation point and a 3-percent error at $R/R_B = 0.5$) for the shock-tube volumes. The error in the volumes from the shock tunnel are much less. The error due to the subjective choice made in the choice of radiating volumes cannot be made without a detailed radiation distribution for each of the models tested. The effect of the difference in radiation distributions between the shock tube and flight and range conditions was found to be approximately 25 percent (Reference Appendix D).

Thus, an estimate of the error in the final predictions at the trajectory point is found to be approximately ± 30 percent, while the scatter is ± 50 percent.

VI. RESULTS AND DISCUSSION

A. SHOCK SHAPES

The schlieren photographs of the shock shapes in the shock tunnel and a typical image converter photograph of the tension shell taken in the shock tube are shown in Figures 18a through 18j.

An estimate of the radiating volume was obtained from the photographs (measured with a Jones and Lamson optical comparator FC-30ER) using the Second Proposition of Pappus for tests at zero angle-of-attack, and by a similar method (by dividing the shock layer into segments) in the case of angle-of-attack.

The radiating volume corresponding to the ballistic range case was taken as that obtained in the hypersonic shock tunnel, corrected by the cube of the ratio of the corresponding base diameters. A similar procedure was used to obtain the radiating volume on a nominal flight vehicle (base diameter = 18.5 feet). All the appropriate radiating volumes are given in Table II.

B. BALLISTIC RANGE RADIATION MEASUREMENTS

The radiation emitted in the forward direction by the models in the ballistic range is tabulated in Table III. Since the data were reduced using a $\frac{1}{r^2}$ dependence, all the data for a given run should be constant. Only one Apollo run and one blunt-cone run satisfy this requirement within a factor of 2. The remaining runs show a much larger scatter, indicating that the radiation did not follow a $\frac{1}{r^2}$ dependence. The reason for this behavior is unknown, since the $\frac{1}{r^2}$ dependence held during calibration to within 4 percent; hence, a reliable radiation measurement for the tension shell was not obtained in the ballistic range. Other runs were made; however, the information necessary for data reduction was incomplete (e.g., no model velocity was obtained), or ablation was present.

The two good runs indicate that the Apollo shape generates a higher level of radiation than does the blunt cone, as seen by the S-1 and S-11 radiometers.

C. SHOCK-TUBE RADIATION MEASUREMENTS

The radiation over the entire body was monitored by the side-looking radiometers. The results are shown in Figure 19 and 20 and tabulated in Table IV. Only in case of the tension shell does the radiation decrease significantly with angle-of-attack. This is because only for this body shape does the shock layer change drastically as we go from 0 to 45 degrees. This is due to the fact that the stand-off distance in the shock tube is quite high and the flow Mach number is quite low,

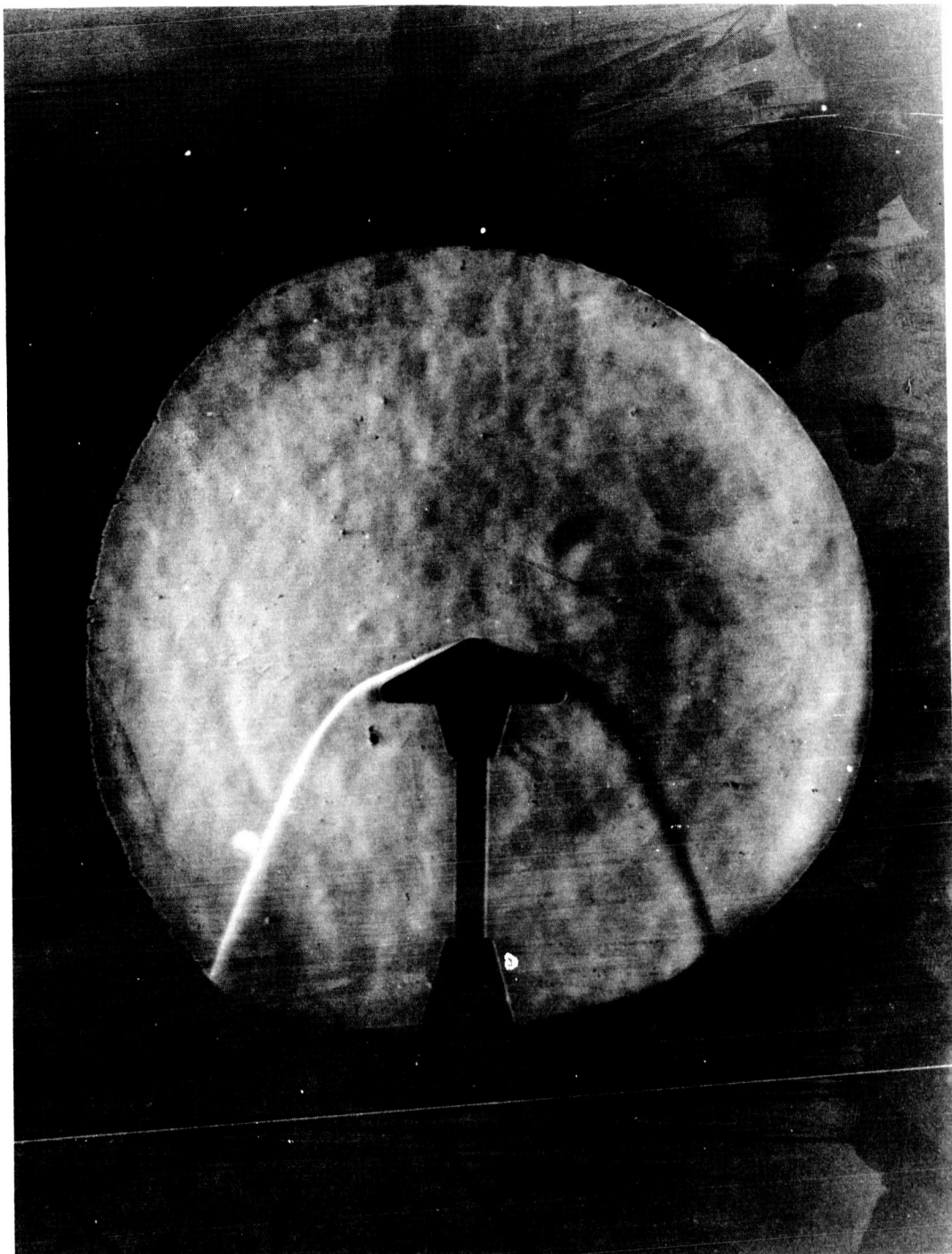


Figure 18a SHOCK-TUNNEL SCHLIEREN PHOTOGRAPH OF BLUNT CONE;
 $\alpha = 0$ DEGREES

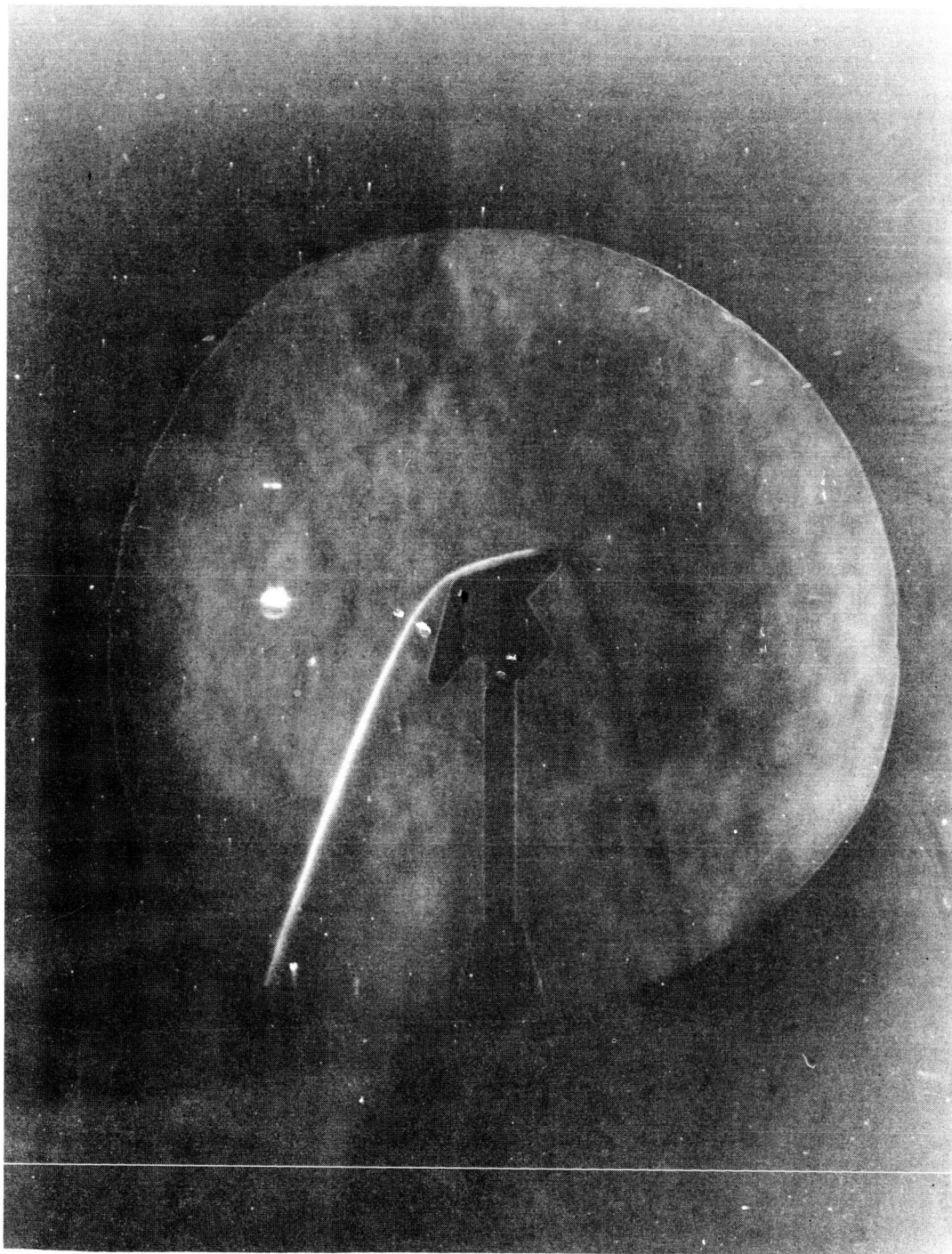


Figure 18b SHOCK-TUNNEL SCHLIEREN PHOTOGRAPH OF BLUNT CONE;
 $\alpha = 45$ DEGREES

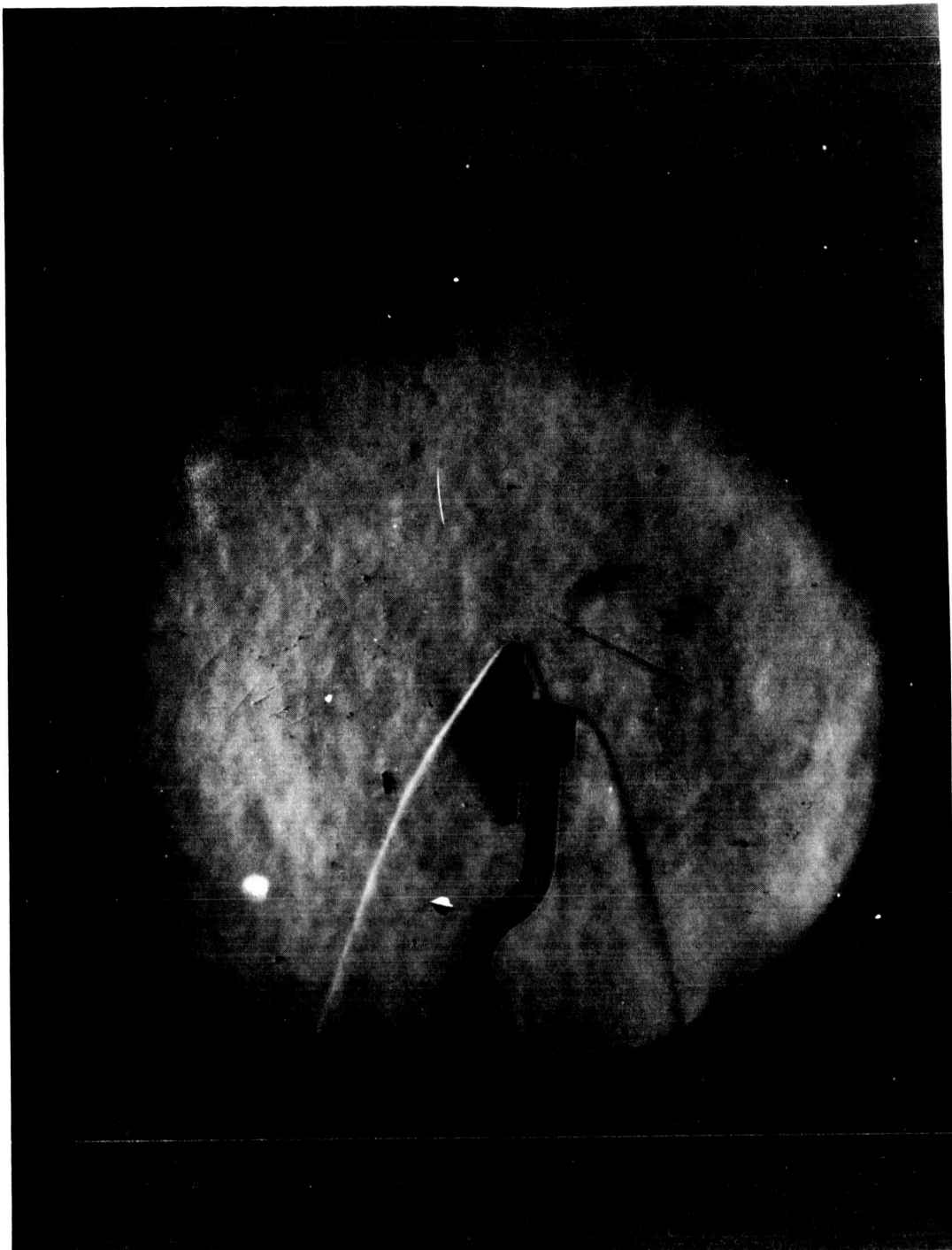


Figure 18c SHOCK-TUNNEL SCHLIEREN PHOTOGRAPH OF BLUNT CONE;
 $\alpha = 90$ DEGREES

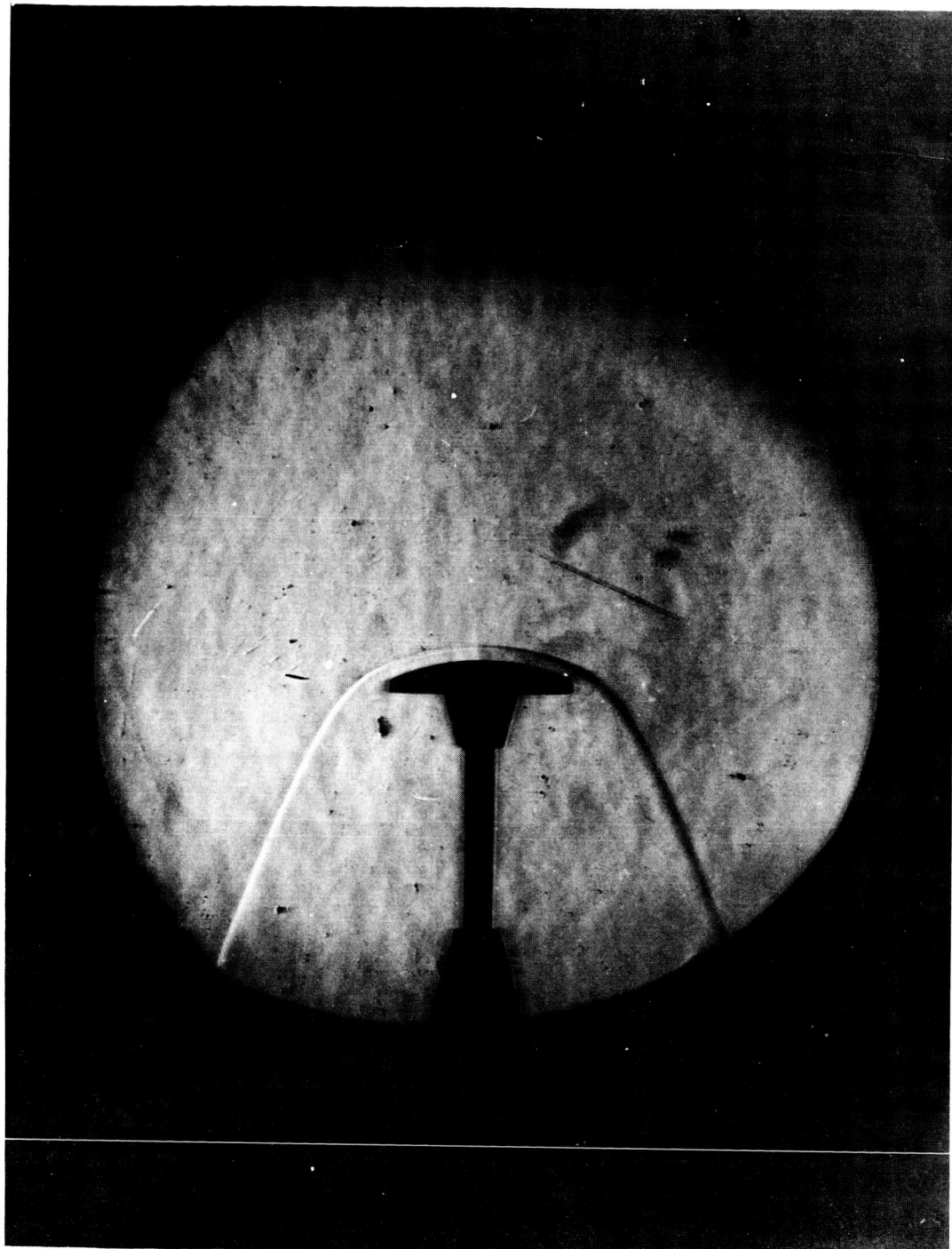


Figure 18d SHOCK-TUNNEL SCHLIEREN PHOTOGRAPH OF MODIFIED APOLLO;
 $\alpha = 0$ DEGREES

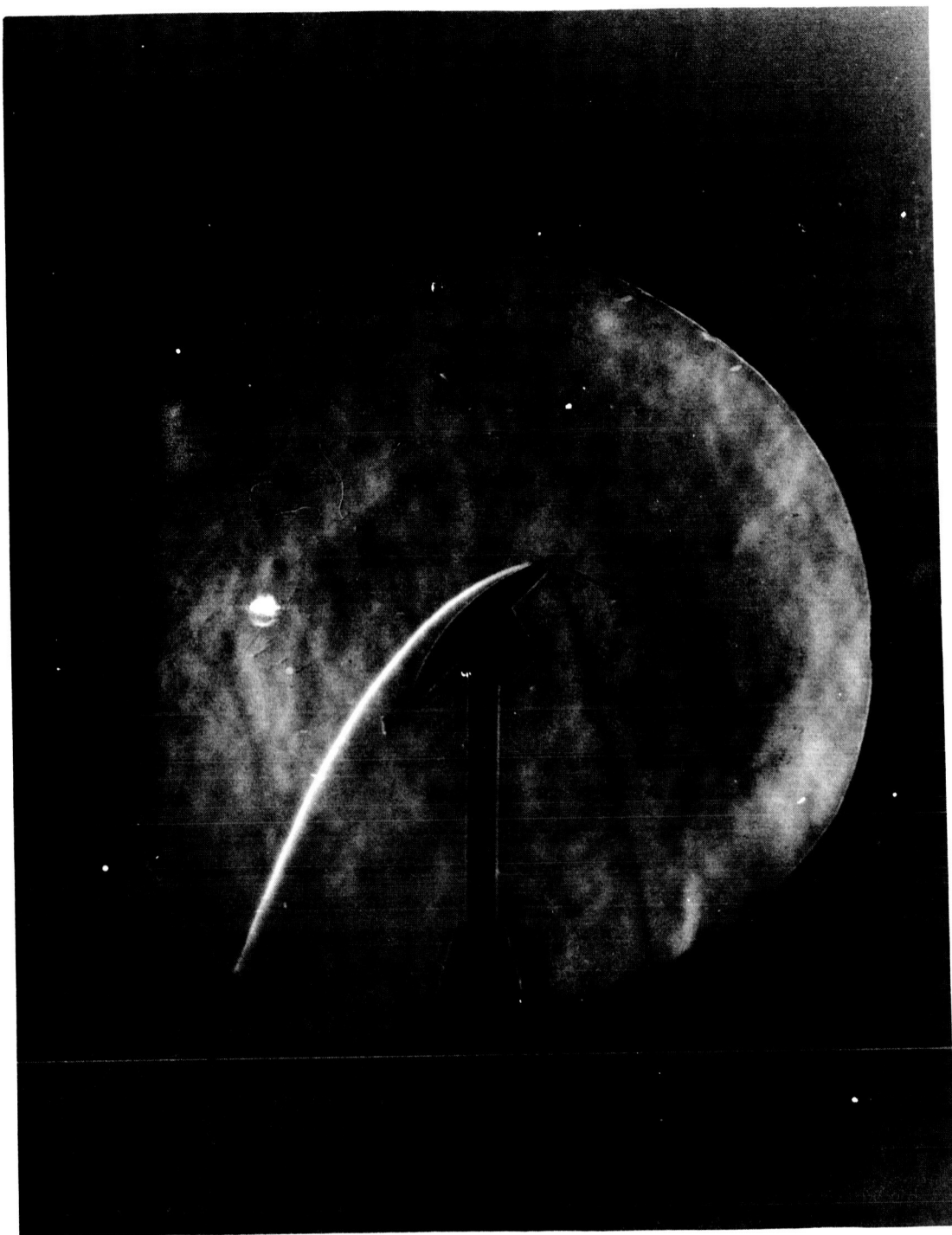


Figure 18e SHOCK-TUNNEL SCHLIEREN PHOTOGRAPH OF MODIFIED APOLLO;
 $\alpha = 45$ DEGREES

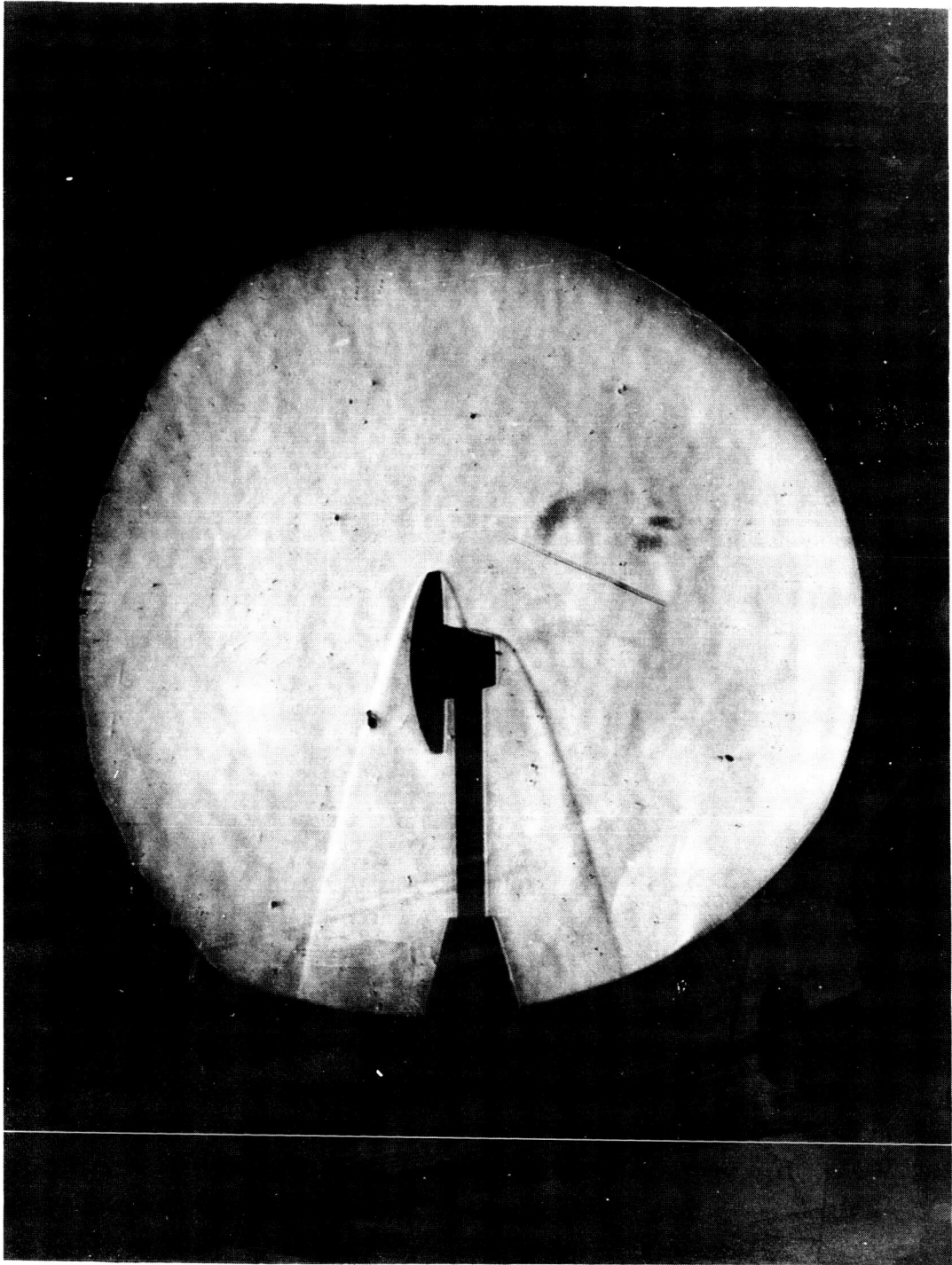


Figure 18f SHOCK-TUNNEL SCHLIEREN PHOTOGRAPH OF MODIFIED APOLLO;
 $\alpha = 90$ DEGREES

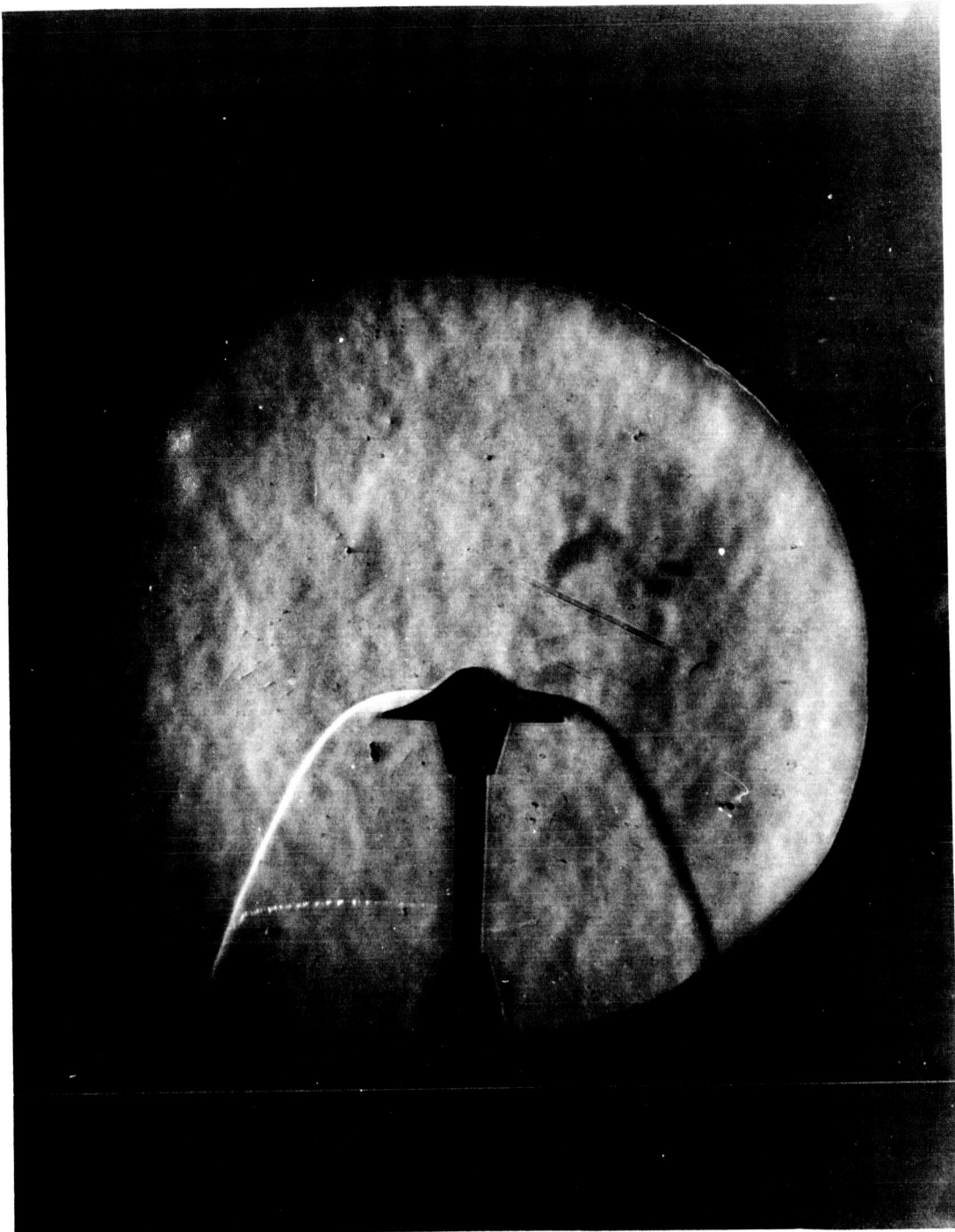


Figure 18g SHOCK-TUNNEL SCHLIEREN PHOTOGRAPH OF TENSION SHELL;
 $\alpha = 0$ DEGREES

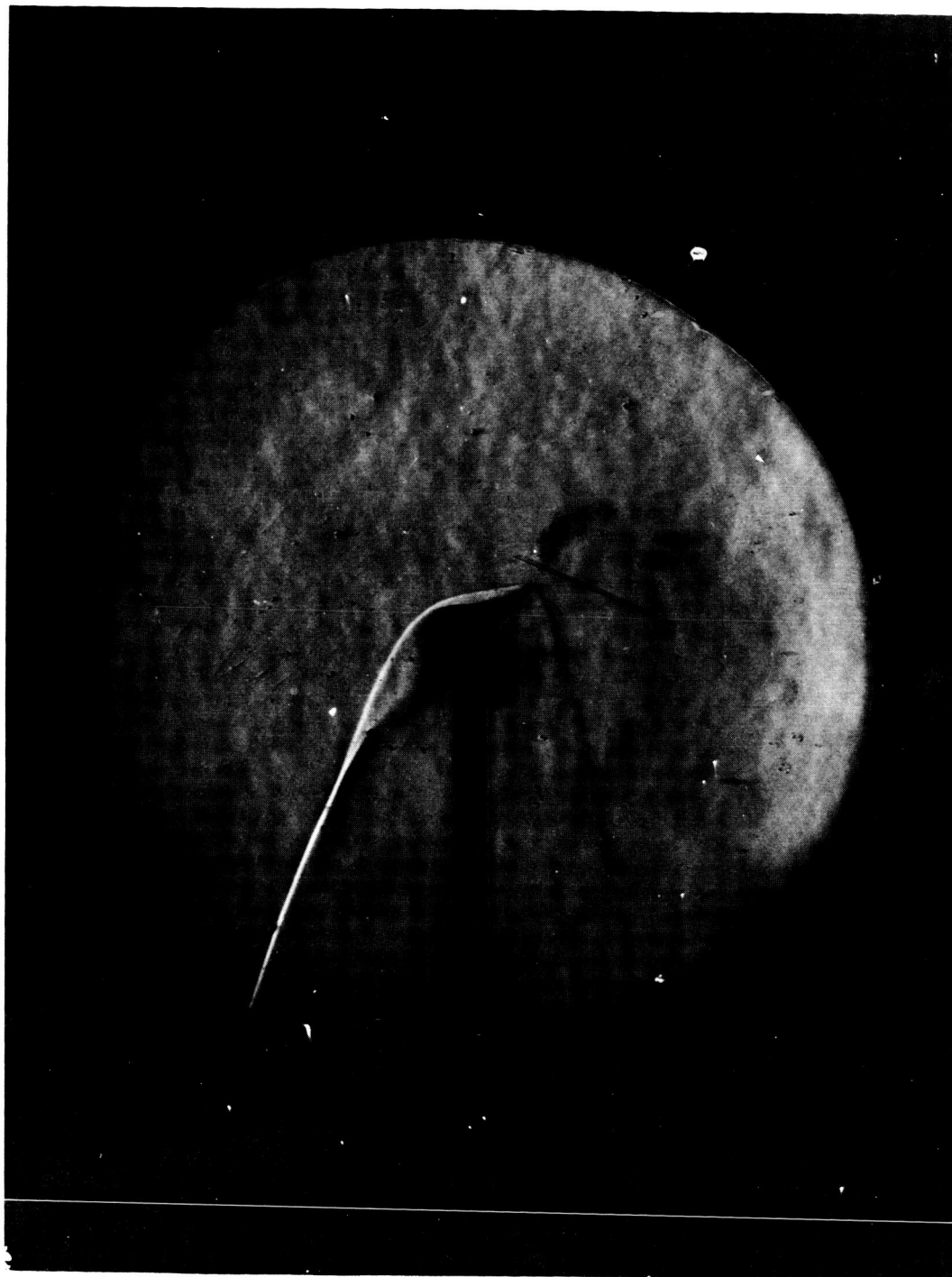


Figure 18h SHOCK-TUNNEL SCHLIEREN PHOTOGRAPH OF TENSION SHELL;
 $\alpha = 45$ DEGREES

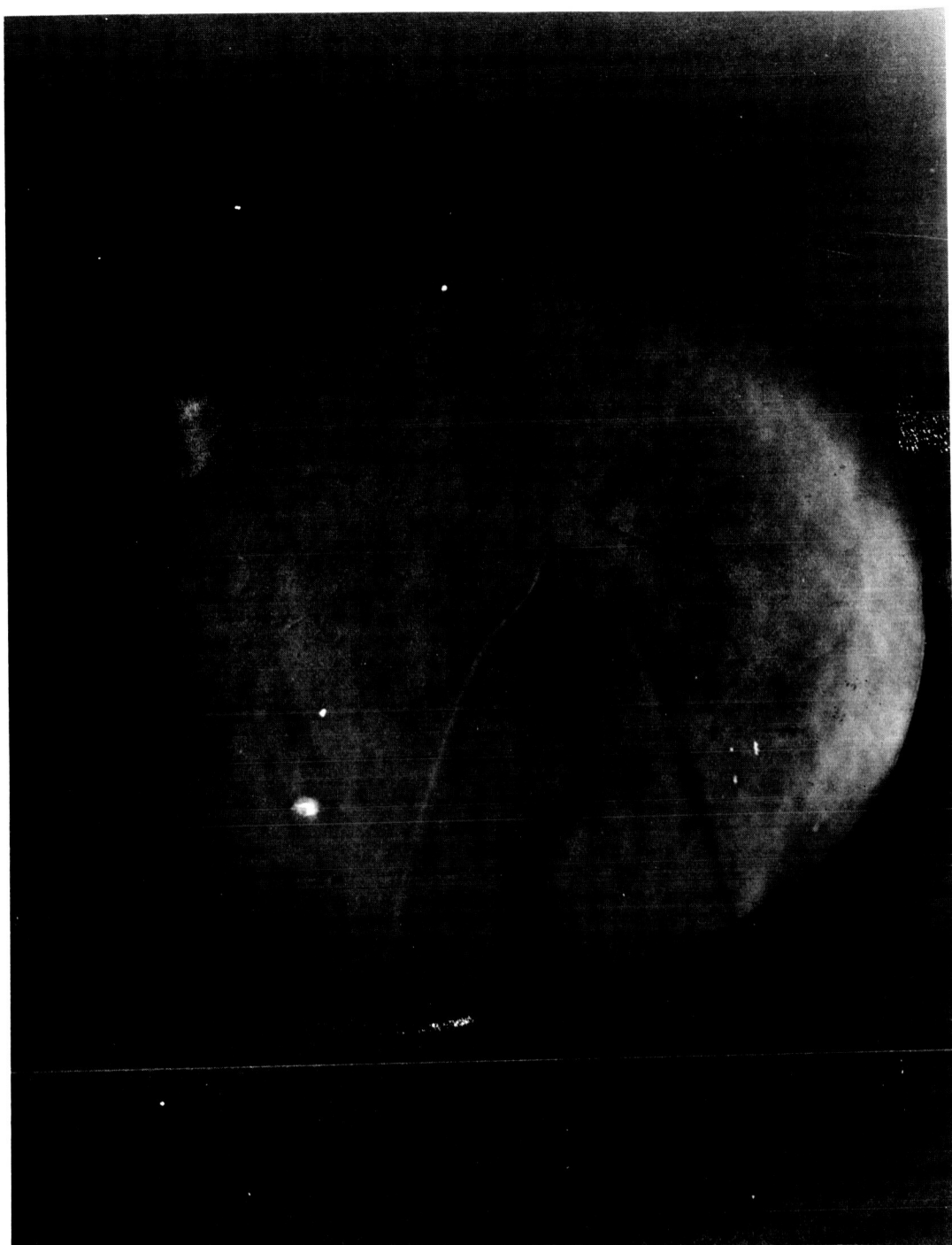
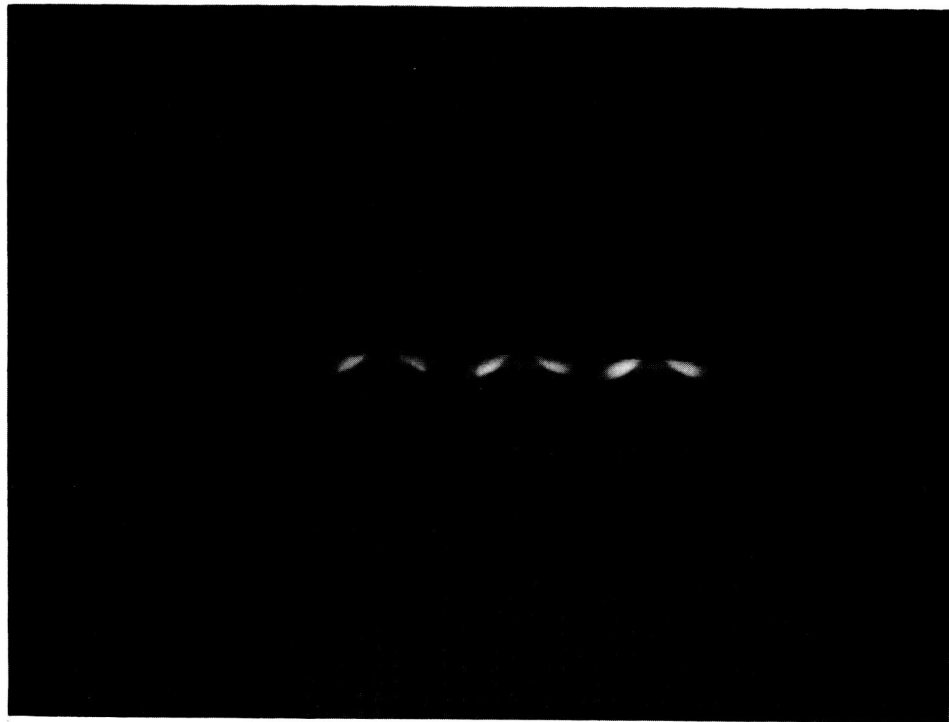


Figure 18i SHOCK-TUNNEL SCHLIEREN PHOTOGRAPH OF TENSION SHELL;
 $\alpha = 90$ DEGREES



86-8745

Figure 18j IMAGE CONVERTER PHOTOGRAPH OF TENSION SHELL IN SHOCK
TUBE; $\alpha = 0$ DEGREES

TABLE II
RADIATIVE VOLUMES

| | Shock Tube ($R_B = 1$ inch) | Shock Tunnel ($R_B = 1$ inch) | Ballistic Range ($R_B = .2$ inch) | Trajectory ($R_B = 9.25$ feet) |
|---------------|--|--------------------------------|------------------------------------|------------------------------------|
| Blunt Cone | $\alpha = 0$ degrees 25.9 cm ³ | (6.17 cm ³) | 0.0493 cm ³ | 8.44×10^6 cm ³ |
| | $\alpha = 45$ degrees 11.6 cm ³ | (1.50 cm ³) | 0.0120 cm ³ | 2.05×10^6 cm ³ |
| | $\alpha = 90$ degrees 3.22 cm ³ | (2.58 cm ³) | 0.0206 cm ³ | 3.53×10^6 cm ³ |
| Apollo | $\alpha = 0$ degrees 45.4 cm ³ | (19.8 cm ³) | 0.159 cm ³ | 27.2×10^6 cm ³ |
| | $\alpha = 45$ degrees 17.6 cm ³ | (3.34 cm ³) | 0.0267 cm ³ | 4.57×10^6 cm ³ |
| | $\alpha = 90$ degrees 1.90 cm ³ | (3.15 cm ³) | 0.0253 cm ³ | 4.31×10^6 cm ³ |
| Tension Shell | $\alpha = 0$ degrees 17.8 cm ³ | (13.7 cm ³) | 0.110 cm ³ | 18.8×10^6 cm ³ |
| | $\alpha = 45$ degrees 7.29 cm ³ | (1.88 cm ³) | 0.0150 cm ³ | 2.57×10^6 cm ³ |
| | $\alpha = 90$ degrees 3.09 cm ³ | (4.30 cm ³) | 0.0344 cm ³ | 5.88×10^6 cm ³ |

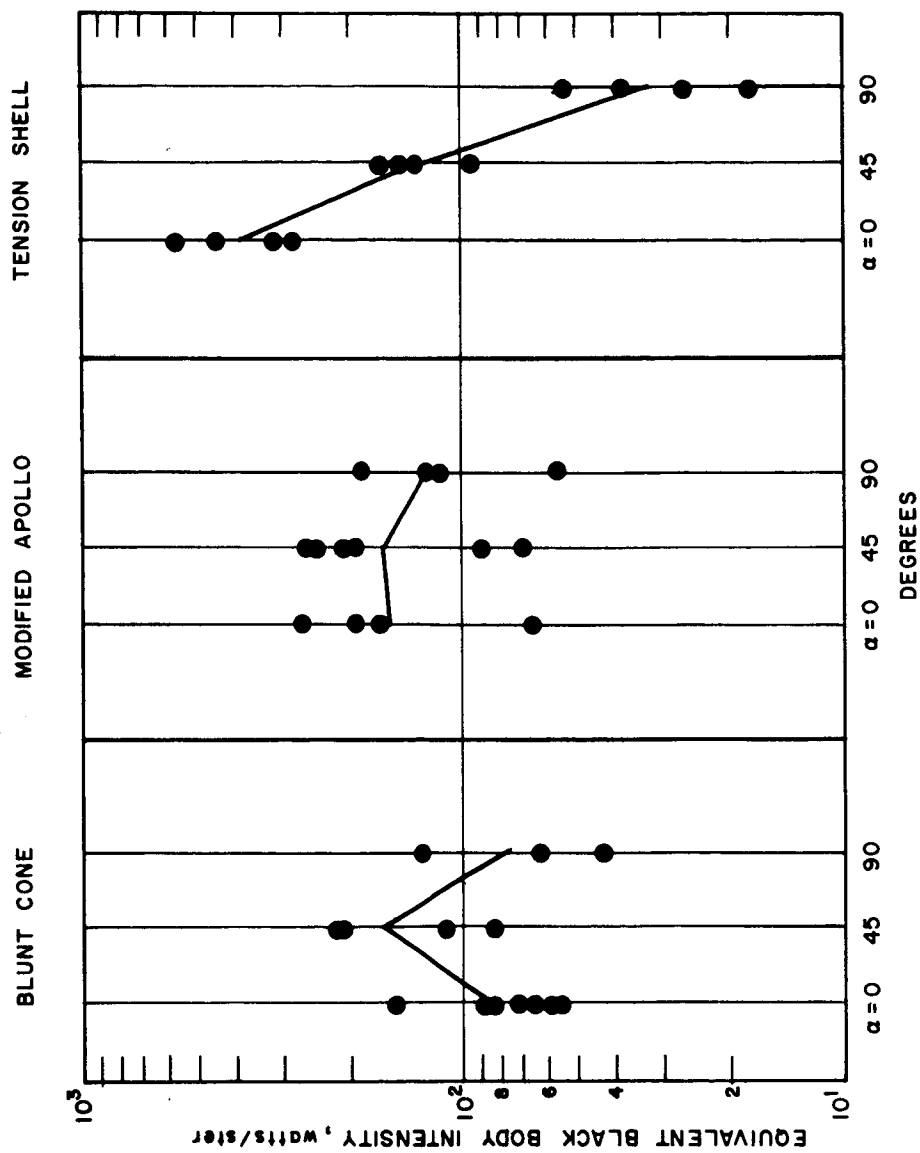
TABLE III
BALLISTIC RANGE RADIATION DATA ⁺

| | cm | J_B Equiv. Black Body Intensity (watt/ster) | $J_B \left(\frac{U^*}{U_m} \right)^{11.8}$ (watt/ster) | $J_B \left(\frac{U^*}{U_m} \right)^{11.8} / J_B$ (watt/ster) | J_R Equiv. Black Body Intensity (watt/ster) | $J_R \left(\frac{U^*}{U_m} \right)^{11.8}$ (watt/ster) | $J_R \left(\frac{U^*}{U_m} \right)^{11.8} / J_R$ (watt/ster) |
|--|-----|--|--|--|--|--|--|
| Model: Blunt Cone flight velocity: 15,842 ft/sec | 82 | 1.87 | 1.95 | 6.30 | | | |
| | 132 | 1.03 | 1.07 | 3.47 | 0.218 | 0.228 | 0.501 |
| Model: Apollo flight velocity: | 82 | 11.7 | 10.2 | 33.1 | | | |
| 16,083 ft/sec | 132 | 8.66 | 7.58 | 24.4 | less than ++ | less than | less than |
| | 182 | 8.19 | 7.17 | 23.1 | 50.0 | 43.8 | 96.5 |
| | 232 | 5.88 | 5.15 | 16.6 | | | |

⁺ Note: The * indicates the appropriate nominal test conditions indicated in Table I were used. Subscript B is for S-11 response, and subscript R for S-1 response.

++ This was the first run, and instrumentation sensitivity was set too high.

$3400 \text{ \AA} \leq \lambda \leq 5600 \text{ \AA}$

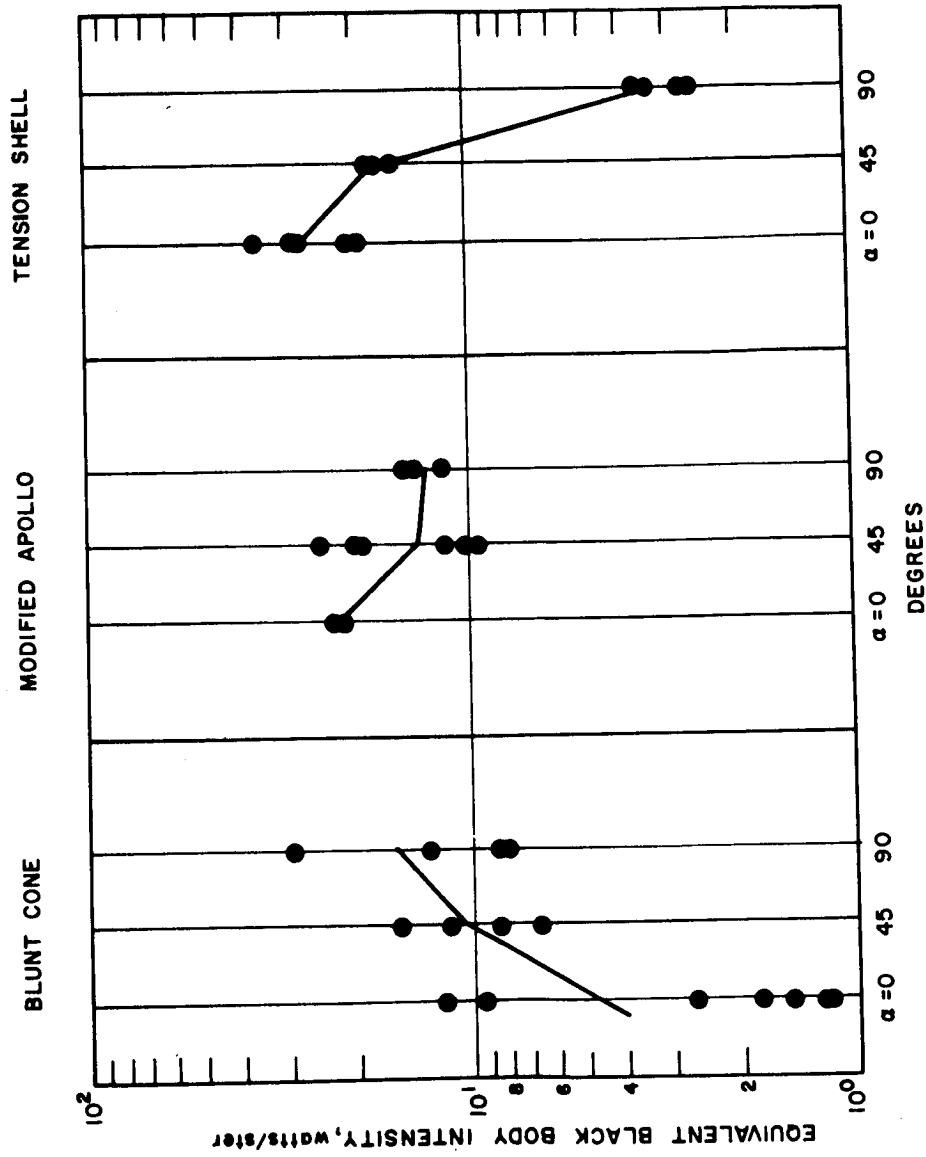


86-8748

Figure 19 SHOCK-TUBE RADIATION DATA (S-11)

25

$4800 \text{ \AA} \leq \lambda \leq 13,000 \text{ \AA}$



86-8749

Figure 20 SHOCK-TUBE RADIATION DATA (S-1)

53-1

TABLE IV
SHOCK-TUBE RADIATION DATA⁺

| Run | Model | p_a (torr) | U_a (mm/ μ sec) | J_B (watt/ster) | J_B Equiv. Blackbody Intensity (watt/ster) | J_B (watt/ster) | J_R (watt/ster) | J_R Equiv. Blackbody Intensity (watt/ster) | J_R (watt/ster) | J_B (watt/ster) | J_R (watt/ster) |
|-----|----------------------------|-----------------|--------------------------|----------------------|--|----------------------|----------------------|--|----------------------|----------------------|----------------------|
| 111 | Cone = 0 Degrees | 1.00 | 3.73 | .1513 | .152 | .578 | 0.0410 | .0414 | .0769 | -- | -- |
| 112 | | 1.00 | -- | .1513 | .152 | .578 | .0780 | .0788 | .146 | -- | -- |
| 115 | | 1.00 | 3.65 | .0842 | .120 | .455 | .0450 | .0642 | .119 | -- | -- |
| 116 | | 4.80 | 3.67 | 78.1 | 72.1 | 273. | 2.88 | 2.65 | 4.93 | 2.77×10^5 | 1.01×10^4 |
| 117 | | 4.80 | 3.77 | 124. | 83.8 | 317. | 2.23 | 1.50 | 2.79 | 3.22×10^5 | 0.577×10^4 |
| 118 | | 4.80 | 3.70 | 70.6 | 59.2 | 224. | 1.42 | 1.19 | 2.21 | 2.27×10^5 | 0.457×10^4 |
| 119 | | 4.90 | 3.67 | 62.2 | 56.0 | 212. | 1.34 | 1.21 | 2.25 | 2.15×10^5 | 0.465×10^4 |
| 120 | | 4.90 | 3.70 | 108. | 88.4 | 335. | 2.19 | 1.79 | 3.33 | 3.40×10^5 | 0.688×10^4 |
| 122 | | 1.00 | 3.77 | 11.4 | 11.1 | 42.1 | 1.04 | 1.01 | 1.08 | -- | -- |
| 123 | Cone = 0 Degrees | 1.00 | 3.76 | 33.2 | 33.2 | 125. | -- | -- | -- | -- | -- |
| 124 | Cone = 45 Degrees | 4.80 | 3.65 | 113. | 112. | 424. | -- | -- | -- | 2.34×10^5 | -- |
| 125 | | 4.80 | 3.66 | 87.3 | 83.3 | 315. | 9.01 | 8.60 | 15.9 | 1.74×10^5 | 1.79×10^4 |
| 126 | | 4.80 | 3.73 | -- | -- | -- | 8.80 | 6.71 | 12.4 | -- | 1.40×10^4 |
| 127 | | 4.80 | 3.78 | 333. | 217. | 824. | 17.6 | 11.4 | 28.5 | 4.54×10^5 | 2.39×10^4 |
| 128 | Cone = 45 Degrees | 4.85 | 3.70 | 257. | 214. | 811. | 18.5 | 15.3 | 28.5 | 4.47×10^5 | 3.21×10^4 |
| 129 | Cone = 90 Degrees | 4.85 | 3.62 | 121. | 130. | 494. | 27.2 | 29.2 | 54.3 | 16.9×10^5 | 37.8×10^4 |
| 130 | | 4.90 | -- | 41.7 | 42.8 | 162. | 8.13 | 8.34 | 15.5 | 5.54×10^5 | 10.8×10^4 |
| 131 | | 4.90 | 3.76 | 91.1 | 61.7 | 233. | 12.6 | 8.57 | 15.9 | 8.00×10^5 | 11.1×10^4 |
| 132 | Cone = 90 Degrees | 4.80 | 3.90 | -- | -- | -- | 28.9 | 13.0 | 24.3 | -- | 16.9×10^4 |
| 133 | Apollo = 0 Degrees | 4.90 | 3.58 | 159. | 192. | 729. | -- | -- | -- | 13.6×10^5 | -- |
| 134 | | 4.85 | 3.69 | 311. | 266. | 1010. | -- | -- | -- | 18.8×10^5 | -- |
| 136 | | 4.90 | 3.65 | 170. | 166. | 630. | 22.9 | 22.3 | 41.6 | 11.7×10^5 | 15.8×10^4 |
| 137 | Apollo = 0 Degrees | 4.90 | 3.65 | 68.3 | 65.6 | 248. | 22.9 | 22.0 | 41.0 | 4.64×10^5 | 15.6×10^4 |
| 139 | Apollo = 45 Degrees | 4.90 | 3.90 | 587.1 | 259. | 981. | 44.8 | 19.8 | 36.8 | 7.94×10^5 | 6.07×10^4 |
| 140 | | 4.80 | 3.84 | 258. | 194. | 735. | -- | -- | -- | 5.95×10^5 | -- |
| 141 | | 5.00 | 3.86 | 425. | 205. | 780. | 40.3 | 19.5 | 36.3 | 6.31×10^5 | 5.98×10^4 |
| 142 | | 4.90 | 3.90 | 558. | 245. | 931. | 56.24 | 24.7 | 46.0 | 7.53×10^5 | 7.59×10^4 |
| 143 | | 4.90 | 3.68 | 79.8 | 69.6 | 263. | 11.5 | 10.0 | 18.7 | 2.13×10^5 | 3.08×10^4 |
| 144 | Apollo = 45 Degrees | 4.85 | 3.61 | 80.7 | 89.7 | 339. | 10.4 | 11.5 | 21.4 | 2.75×10^5 | 3.54×10^4 |
| 145 | | 4.85 | 3.67 | -- | -- | -- | 10.4 | 9.55 | 17.7 | -- | 2.92×10^4 |
| 146 | Apollo = 90 Degrees | 4.85 | 3.67 | 61.9 | 56.6 | 214. | 15.3 | 14.0 | 26.0 | 15.1×10^5 | 37.5×10^4 |
| 147 | | 4.85 | 3.72 | 160. | 125. | 474. | 19.1 | 14.9 | 27.7 | 33.55×10^5 | 40.0×10^4 |
| 148 | | 4.80 | 3.73 | 242. | 184. | 699. | 15.3 | 11.6 | 21.7 | 49.5×10^5 | 31.3×10^4 |
| 149 | Apollo = 90 Degrees | 4.90 | 3.69 | 134. | 113. | 431. | -- | -- | -- | 30.5×10^5 | -- |
| 151 | Cone = 0 Degrees | 2.40 | 3.76 | 72.2 | 67.5 | 255. | 5.14 | 4.80 | 8.93 | -- | -- |
| 152 | | 2.60 | 3.49 | 120. | 244. | 925. | 9.99 | 20.2 | 37.6 | -- | -- |
| 153 | | 2.55 | 3.46 | 48.1 | 111. | 420. | 3.14 | 7.24 | 13.4 | -- | -- |
| 154 | | 2.60 | 3.64 | 303. | 375. | 1420. | -- | -- | -- | -- | -- |
| 155 | | 2.50 | 3.55 | 67.5 | 117. | 446. | 9.92 | 17.3 | 32.2 | -- | -- |
| 156 | | 7.60 | 3.65 | 443. | 416. | 1570. | 50.8 | 47.7 | 88.6 | -- | -- |
| 158 | | 7.50 | 3.65 | 2420. | 2320. | 8780. | 35.9 | 34.3 | 63.8 | -- | -- |
| 159 | | 7.70 | 3.63 | -- | -- | -- | 50.7 | 50.0 | 92.9 | -- | -- |
| 160 | | 7.60 | 3.55 | 6570. | 8570. | 32400. | -- | -- | -- | -- | -- |
| 161 | | 9.90 | 3.70 | 56300. | 43900. | 166000. | 8.46 | 6.58 | 12.24 | -- | -- |
| 162 | | 9.95 | 3.62 | 53400. | 50360. | 190000. | 57.10 | 53.8 | 100. | -- | -- |
| 163 | | 9.80 | 3.70 | -- | -- | -- | 11.6 | 48.5 | 90.3 | -- | -- |
| 164 | Cone = 0 Degrees | 9.95 | 3.75 | -- | -- | -- | 12.5 | 34.3 | 63.9 | -- | -- |
| 166 | Tension Shell = 45 Degrees | 4.80 | 3.65 | 168. | 165. | 626. | -- | -- | -- | 6.88×10^5 | -- |
| 167 | | 4.90 | 3.63 | 130. | 133. | 505. | 15.4 | 15.8 | 29.3 | 5.56×10^5 | 6.58×10^4 |
| 168 | | 4.80 | 3.65 | 96.4 | 94.9 | 359. | 17.7 | 17.4 | 32.4 | 3.95×10^5 | 7.26×10^4 |
| 169 | Tension Shell = 45 Degrees | 4.90 | 3.63 | 144. | 148. | 562. | 17.7 | 18.1 | 33.7 | 6.18×10^5 | 7.56×10^4 |
| 170 | Tension Shell = 0 Degrees | 4.80 | 3.60 | 270. | 312. | 1180. | 24.5 | 28.4 | 52.8 | 39.3×10^5 | 35.4×10^4 |
| 171 | | 4.75 | 3.66 | -- | -- | -- | 37.1 | 36.0 | 66.9 | -- | 44.9×10^4 |
| 172 | | 4.75 | 3.52 | 183. | 281. | 1060. | 12.5 | 19.3 | 35.8 | 35.1×10^5 | 24.0×10^4 |
| 173 | | 4.85 | 3.59 | 376. | 445. | 1680. | 17.1 | 20.3 | 37.7 | 55.6×10^5 | 25.3×10^4 |
| 174 | Tension Shell = 0 degree | 4.80 | 3.65 | 578. | 569. | 2150. | 28.5 | 28.1 | 52.2 | 71.0×10^5 | 35.0×10^4 |
| 176 | Tension Shell = 90 degrees | 4.80 | 3.62 | 24.2 | 26.2 | 99.3 | 3.31 | 3.59 | 6.67 | 5.89×10^5 | 8.07×10^4 |
| 178 | | 4.90 | 3.57 | 19.7 | 17.8 | 67.4 | 2.06 | 2.57 | 4.78 | 4.00×10^5 | 5.77×10^4 |
| 179 | | 4.75 | 3.64 | 72.4 | 54.0 | 204. | 2.62 | 2.71 | 5.04 | 12.1×10^5 | 6.09×10^4 |
| 180 | Tension Shell = 90 Degrees | 4.80 | 3.60 | 46.1 | 38.5 | 145. | 2.93 | 3.40 | 6.32 | 8.66×10^5 | 7.64×10^4 |
| 182 | Instr. Cone = 0 Degrees | 5.00 | 3.63 | 65.7 | 65.7 | 249. | -- | -- | -- | 2.52×10^5 | -- |
| 183 | | 5.05 | 3.65 | -- | -- | -- | 10.1 | 9.42 | 17.5 | -- | -- |
| 184 | Instr. Cone = 0 Degrees | 5.00 | 3.69 | 184. | 152. | 575. | 14.5 | 11.9 | 22.2 | 5.84×10^5 | 4.60×10^4 |

+ NOTE: The * indicates that the appropriate nominal test conditions indicated in Table II were used.

-53-2

causing the shock-layer volume to be relatively insensitive to angle-of-attack. This point is quite important in scaling the angle-of-attack effects, since in the hypersonic case the effect of angle-of-attack on the shock shape, and hence the radiation, will probably be more pronounced than it was in the shock tube (see Section VI D).

The total over-the-body radiation is greatest in the case of the tension shell, and is least for the blunt cone in both wavelength regions at zero angle-of-attack. In the blue wavelength region (3400Å - 5600Å), the ratio of the intensities goes as 4/2/1 for the tension shell, modified Apollo, and blunt cone, respectively, while in the red wavelength region (4800Å - 13,000Å), the ratio goes as 3/2/1, close to that in the blue region.

At 45-degrees angle-of-attack, the effect of body shape on the radiation seems to be nil in the blue wavelength region, but has the same trend as at zero-degrees angle-of-attack for the red wavelength region, with the ratio being 1.7/1.5/1.

At 90-degrees angle-of-attack, the trend is changed somewhat. The modified Apollo generates the greatest radiation, then the blunt cone, and last of all, the tension shell. In the blue, the ratio is 1/.7/.3, and in the red, the ratio of 1.3/1.3/.3.

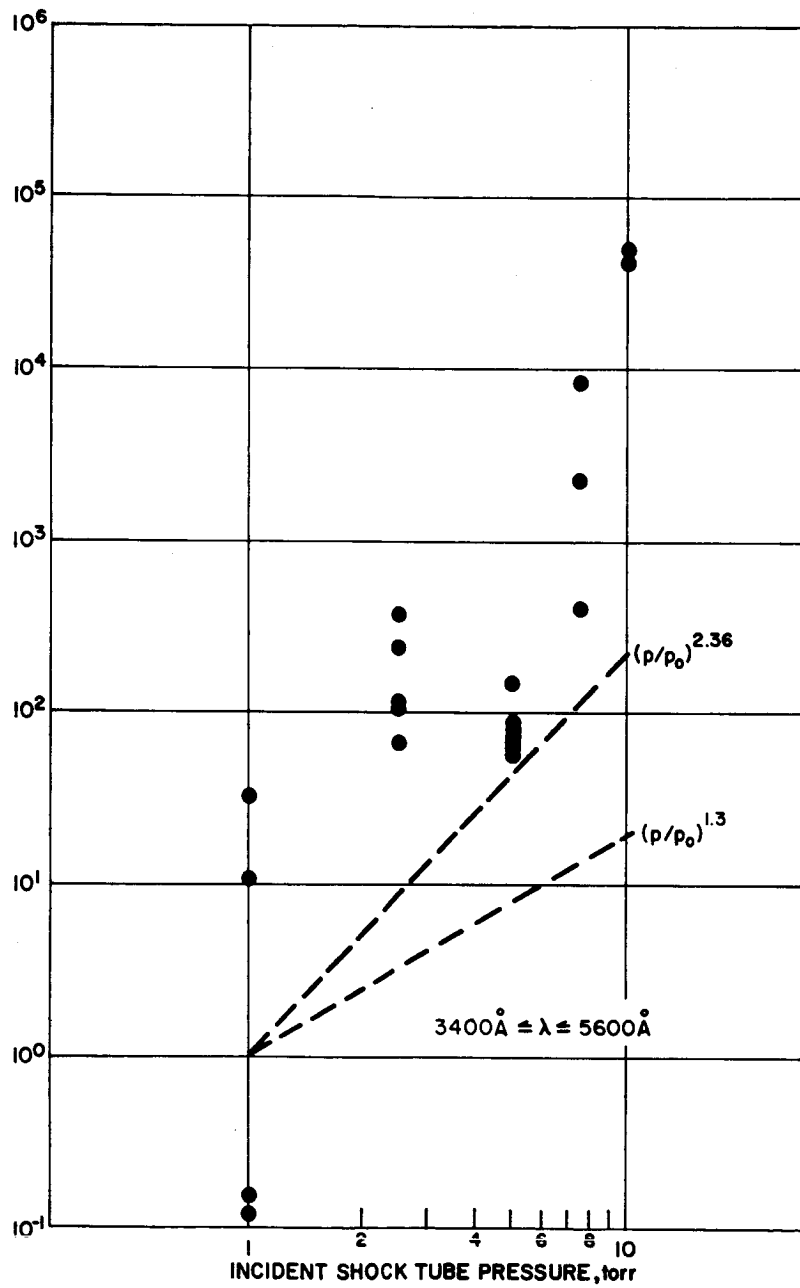
The effect of varying the initial pressure for a single entry shape, while maintaining the stagnation temperature constant, is shown in Figures 21 and 22. The general trend of increasing radiation with increasing pressure agrees with that obtained by previous investigators (summarized in Reference 8). The pressure dependence previously obtained² is $\sim \left(\frac{P^*}{P_\infty}\right)^{1.3}$, which falls within the scatter of the data. The lines in Figures 21 and 22 are shown to illustrate the slope and no attempt has been made to draw the lines through the data.

This scatter is probably due to operating at the low limits of pressure and the consequent experimental difficulties. Some inferences can, however, be made: nonequilibrium radiation is not evident (it would be observed as a deviation from the trend, at the lower pressures, in the direction of increasing radiation), and neither is the effect of self-absorption (which would appear as a deviation also, but in the direction of decreasing radiation at the higher pressure levels).

D. RADIATION SCALING RESULTS

The radiation from the models measured in the shock tube was used to predict that measured in the ballistic range to determine the merits of the analytical model of Section II D. The simple scaling analysis using the equation.

$$J_b = J_a \left(\frac{V_b}{V_a} \right) \left(\frac{\rho_b}{\rho_a} \right)_{\text{stag.}} \quad (12)$$



86-8750

Figure 21 SHOCK-TUBE RADIATION PRESSURE EFFECT DATA (S-11)

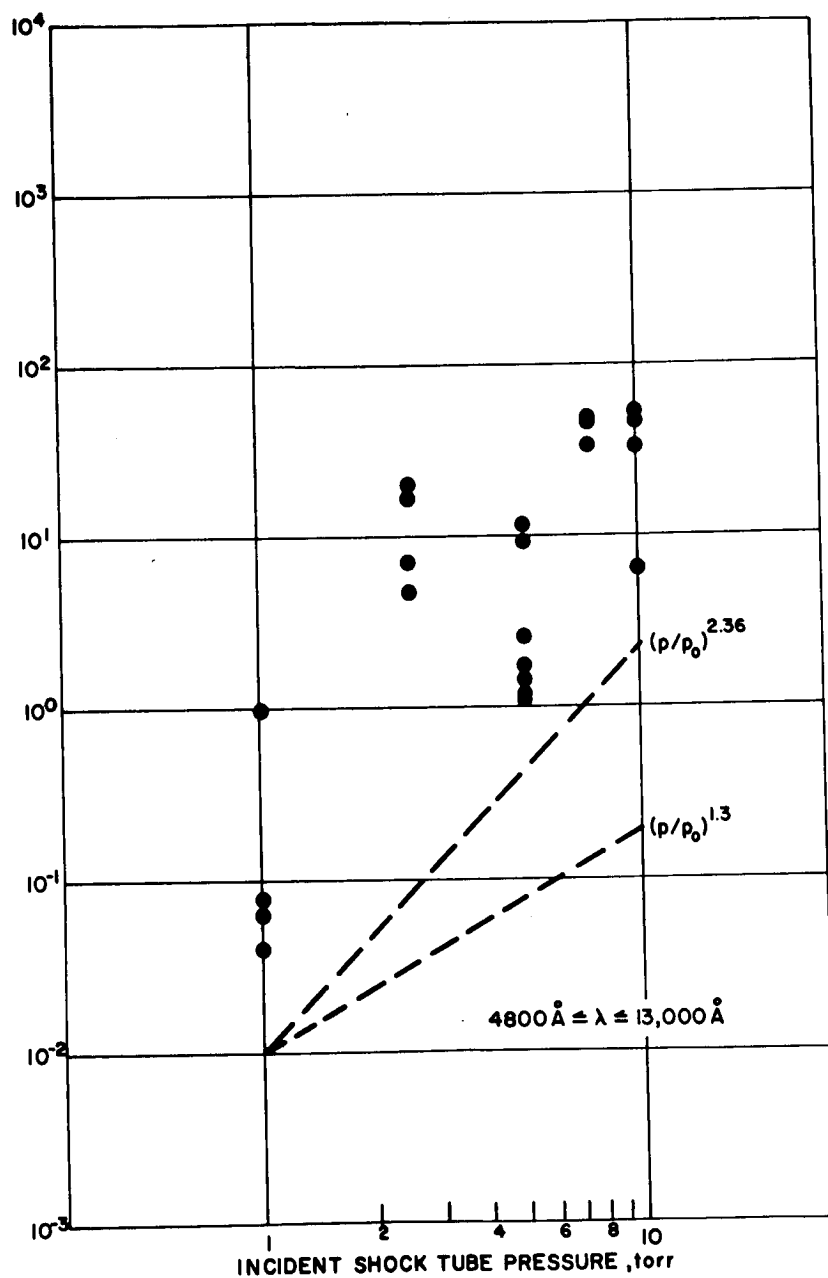


Figure 22 SHOCK-TUBE RADIATION PRESSURE EFFECT DATA (S-1)

yields the data shown in Table V. The agreement is quite good (within a factor of 2). The usefulness of the scaling analysis in predicting the tension shell case could not be checked due to the deviation of the ballistic range radiation from the assumed $\frac{1}{r^2}$ dependence, as discussed previously.

This same scaling equation (with the appropriate radiating volume and density changes) yields the prediction for the equilibrium radiation expected at the trajectory condition, for an entry body with a base diameter of 18.5 feet, shown in Figures 23 and 24. The predictions are compared (in Table VI) with the results calculated in Appendix C. The shock-tube radiation prediction overestimates those calculated in Appendix C by 12 percent for the case of the blunt cone by a factor of 3.5 for the Apollo, and by more than an order-of-magnitude for the tension shell.

The agreement between the simple theory of Appendix C and the shock-tube radiation predictions is quite good for the blunt cone and modified Apollo, but breaks down for the tension shell. This constitutes an approximate verification of the simple theory. It is impossible to assess the usefulness of the scaling analysis for predicting the radiation in the base of the tension shell, however, because it is believed that the simple theory of Appendix C breaks down when the shock-layer flow field becomes as complex as in the case of the tension shell.

As mentioned in Section C, and can be seen in Figures 23 and 24, angle-of-attack effects become more pronounced after scaling to the trajectory condition than they appear in the basic shock-tube results. Taking into account the shock-layer radiation volume corrections definitely causes the radiation to decrease as the angle-of-attack changes from 0 to 45 degrees, except, perhaps, on the Apollo where the radiation remains approximately constant. The trend is reversed, however, at 90 degrees. This is because the radiation is mostly from the shock layer about the afterbody, which is approximately the same for all three models.

The comparison of the relative heating to the various bodies at the flight condition was, however, shown (Reference Appendix D) to be good to within 35 percent. These results are summarized below:

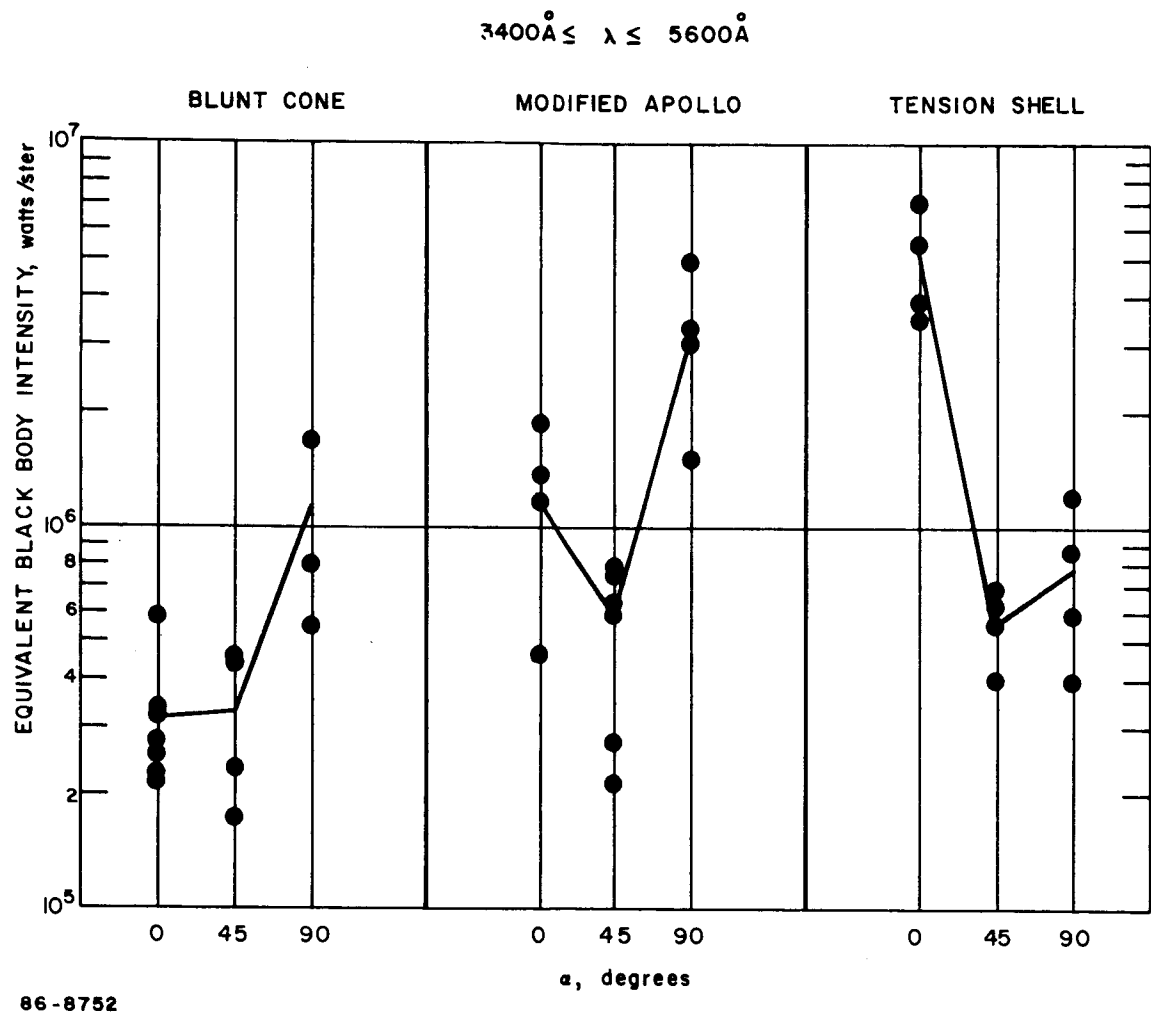
| Angle of Attack | $\frac{W_{\text{Apollo}}}{W_{\text{Cone}}}$ | | $\frac{W_{\text{Tension Shell}}}{W_{\text{Cone}}}$ | |
|-----------------------|---|--------|--|--------|
| | Scaling | Theory | Scaling | Theory |
| $\alpha = 0$ degrees | 2.91 | 1.26 | 16.02 | 1.39 |
| $\alpha = 45$ degrees | 1.69 | -- | 1.82 | -- |
| $\alpha = 90$ degrees | 2.97 | -- | 0.69 | -- |

TABLE V

COMPARISON OF PREDICTED TO ACTUAL
BALLISTIC RANGE DATA

| | | $J_B \text{ predicted} =$ | | $J_R \text{ predicted} =$ | |
|-----------------------|---------------|---|--|---|--|
| | | $\frac{J_{B_a}}{\bar{f}_B} \left(\frac{P^*}{P_\infty} \right)^{1.3} \left(\frac{U^*}{U_\infty} \right)^{11.8}$ (watt/ster) | $\frac{J_{B_a}}{\bar{f}_B} \left(\frac{P^*}{P_\infty} \right)^{1.3} \left(\frac{U^*}{U_\infty} \right)^{11.8} \left(\frac{v_b}{v_a} \right) \frac{\rho_b}{\rho_a}$ (watt/ster) | $\frac{J_{R_a}}{\bar{f}_R} \left(\frac{P^*}{P_\infty} \right)^{1.3} \left(\frac{U^*}{U_\infty} \right)^{11.8}$ (watt/ster) | $\frac{J_{R_a}}{\bar{f}_R} \left(\frac{P^*}{P_\infty} \right)^{1.3} \left(\frac{U^*}{U_\infty} \right)^{11.8} \left(\frac{v_b}{v_a} \right) \frac{\rho_b}{\rho_a}$ (watt/ster) |
| Shock Tube Tests | Cone | 273 | 5.89 | 4.93 | .106 |
| | | 317 | 6.85 | 2.79 | .0602 |
| | | 224 | 4.83 | 2.21 | .0478 |
| | | 212 | 4.58 | 2.25 | .0486 |
| | | 335 | 7.22 | 3.33 | .0718 |
| | | 249 | 5.37 | | .377 |
| | | 575 | 12.4 | | .481 |
| | Apollo | 729 | 23.7 | 41.6 | 1.35 |
| | | 1010 | 32.9 | 41.0 | 1.33 |
| | | 630 | 20.5 | | |
| | | 248 | 8.09 | | |
| | Tension Shell | 1180 | 68.0 | 52.8 | 3.03 |
| | | 1060 | 61.2 | 66.9 | 3.84 |
| | | 1680 | 97.0 | 35.8 | 2.06 |
| | | 2150 | 123 | 37.7 | 2.16 |
| Ballistic Range Tests | | | | | |
| | | | $J_B \left(\frac{U^*}{U_\infty} \right)^{11.8} / \bar{f}_B \text{ watts/ster}$ | $J_R \left(\frac{U^*}{U_\infty} \right)^{11.8} / \bar{f}_R \text{ watts/ster}$ | |
| | Cone | 3.47 | | .501 | |
| | | 6.30 | | | |
| | Apollo | 33.1 | | | |
| | | 24.4 | | | |
| | | 23.1 | | | |
| | | 16.6 | | | |

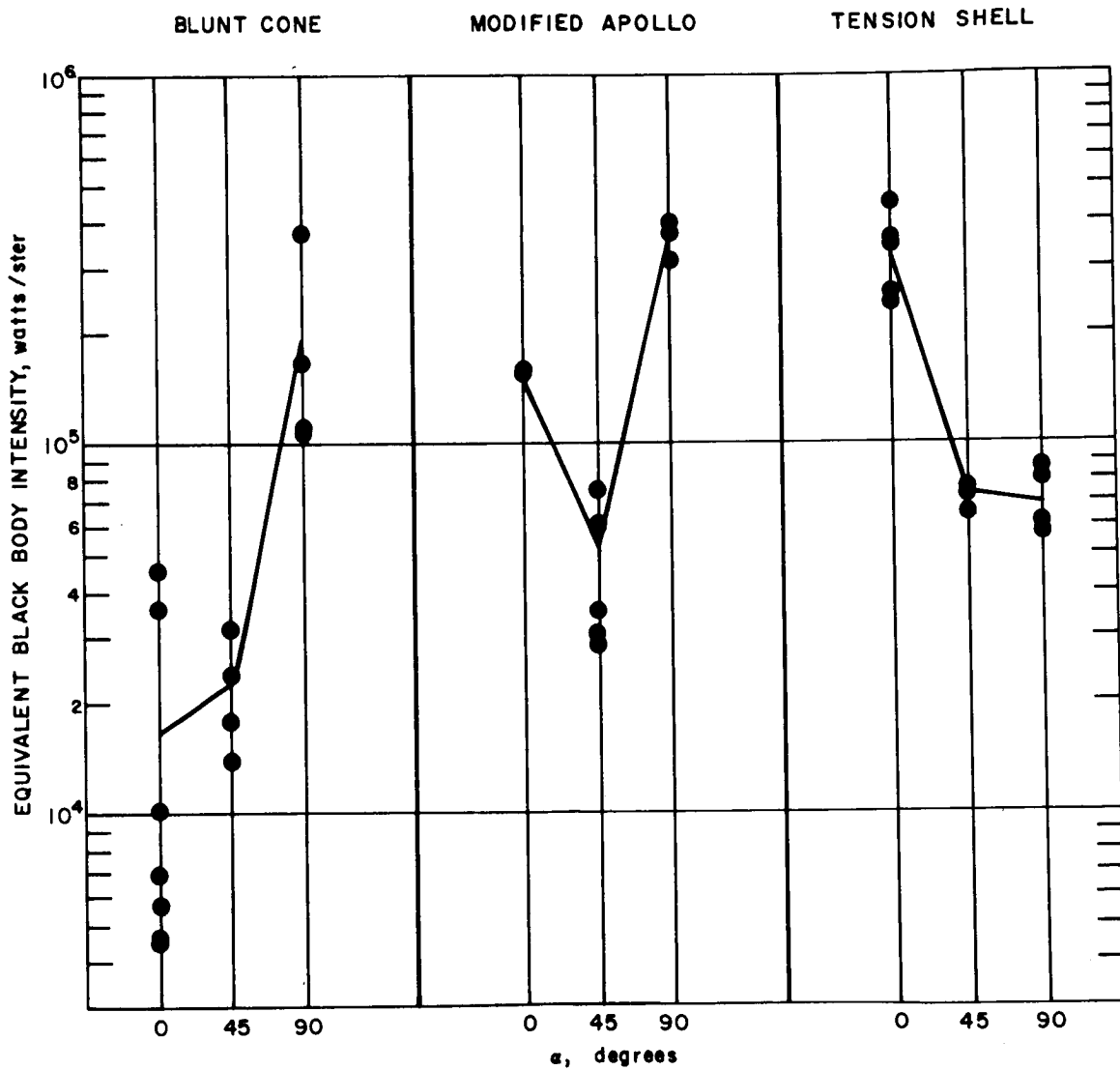
$$\begin{aligned}
 \rho_{b_{\text{stag}}} &= 3.07 \times 10^{-3} \text{ gm/cm}^3 & [CN]_b &= 6.16 \times 10^{15} \text{ cm}^{-3} \\
 \rho_{a_{\text{stag}}} &= 6.62 \times 10 \times 10^{-4} \text{ gm/cm}^3 & [CN]_a &= 2.30 \times 10^{15} \text{ cm}^{-3} \\
 v_b = .0494 \text{ cm}^3 & \left. \begin{array}{l} C \\ O \\ N \\ E \end{array} \right\} & v_b = .159 \text{ cm}^3 & \left. \begin{array}{l} A \\ P \\ O \\ L \\ O \end{array} \right\} & v_b = .110 \text{ cm}^3 & \left. \begin{array}{l} T \\ E \\ N \\ S \\ E \\ I \\ O \\ N \end{array} \right\} \\
 v_a = 25.9 \text{ cm}^3 & & v_a = 45.4 \text{ cm}^3 & & v_a = 17.8 \text{ cm}^3 &
 \end{aligned}$$



86-8752

Figure 23 EXTRAPOLATED TRAJECTORY DATA (S-11; $R_B = 9.25$ FEET)

$$4800\text{\AA} \leq \lambda \leq 13,000\text{\AA}$$



86-8753

Figure 24 EXTRAPOLATED TRAJECTORY DATA (S-1; $R_B = 9.25$ FEET)

TABLE VI
COMPARISON OF PREDICTED FREE FLIGHT RADIATION

| | $\left(\frac{J_B}{\bar{f}_B} + \frac{J_R}{\bar{f}_R} \right) \left(\frac{P_*}{P_\phi} \right)^{1.3} \left(\frac{U_*}{U_\phi} \right)^{11.8}$ (watt/ster) | $W_{predc} = \left(\frac{J_B}{\bar{f}_B} + \frac{J_R}{\bar{f}_R} \right) \left(\frac{P_*}{P_\phi} \right)^{1.3} \left(\frac{U_*}{U_\phi} \right)^{11.8} 2\pi \left(\frac{V_c}{V_a} \right) \left(\frac{\rho_c}{\rho_a} \right)$ (watt) | $W_{c \text{ calculated}}$ (watts) |
|---|---|---|------------------------------------|
| | | | |
| Tension Shell Apollo Cone = 0 Deg = 0 Deg | 278 | 6.72 x 10 ⁶ | 6.80 x 10 ⁶ |
| | 320 | 7.74 x 10 ⁶ | |
| | 226 | 5.47 x 10 ⁶ | |
| | 214 | 5.19 x 10 ⁶ | |
| | 338 | 8.17 x 10 ⁶ | |
| | 249 | 6.01 x 10 ⁶ | 8.60 x 10 ⁶ |
| | 598 | 14.4 x 10 ⁶ | |
| | 729 | 32.4 x 10 ⁶ | |
| | 1010 | 44.9 x 10 ⁶ | |
| | 672 | 29.8 x 10 ⁶ | |
| | 289 | 12.8 x 10 ⁶ | 9.50 x 10 ⁶ |
| | 1230 | 97.0 x 10 ⁶ | |
| | 1100 | 86.3 x 10 ⁶ | |
| | 1720 | 135 x 10 ⁶ | |
| | 2160 | 173 x 10 ⁶ | |

The reason for the high relative heating to the tension shell at zero angle-of-attack can be understood by comparing the shock shapes for the three configurations. It can be seen that the tension shell had shock angles close to normal near the perimeter of the model where the radiating volume contribution is largest. In addition, the tension shell exhibits a very strong shock pattern and large standoff distance (especially in the hypersonic case) near the edge of the model as compared to the other two configurations.

The theory of Appendix C showed that the radiation is high near the body (for the blunt cone) because of the high entropy layer. In the case of the tension shell, however, most of volume has been processed by nearly normal shock and thus the radiation will not decrease as drastically with distance from the body. This is especially important near the perimeter of the body.

E. INSTRUMENTED MODEL

The radiation data obtained using the blunt 60-degree half-angle cone, at zero-degree angle-of-attack, instrumented with fiber optical bundles are given in Table VII, and the local shock standoff distances are given in Table VIII. For the case of radiation to the stagnation point, an integration of Equation (1), assuming a uniform-infinite slab shock layer of thickness equal to the stagnation point shock standoff distance,^{3, 4, 6, 7} yields

$$W = \dot{q} A = 2\pi \delta A \int_{\lambda_1}^{\lambda_2} I_{\lambda} d\lambda \quad (13)$$

To use the Ames data of Figure 2b, however, the correct equation is

$$W = H \delta A \frac{\omega}{4\pi}, \quad (14)$$

since the Ames data is the spectrally integrated, isotropic radiation per unit volume of gas radiating into 4π steradians. This equation yields a value of 4.46×10^{-3} watts, which compares with the experimentally measured values of 2.44×10^{-2} watts shown in Table VII. Thus, agreement is within a factor of 5.

The shock-tube data show that the radiation away from the stagnation point, specifically at fiber bundles 2 and 3 (at a point halfway between the apex and the cone edge and at the cone edge) is greater than the radiation at the stagnation point. Though this result holds strictly only for the low flow Mach number characteristic of shock-tube testing, a scaling analysis similar to that used previously in this report is used to extrapolate the data to the trajectory condition. The extrapolated results are then compared with the simple theory of Appendix C.

TABLE VII
FIBER OPTICS RADIATION DATA*

| Run No. | W_1 (watts) | W_2 (watts) | W_3 (watts) | W_4 (watts) |
|---------|------------------|------------------|------------------|------------------|
| 183 | .0244 | .288 | .0631 | .0198 |
| 184 | .0204 | .239 | .0849 | .0125 |

*All intensities quoted are in the 0.33-1.11 micron wavelength region defined by the spectral response of the Crofon fibers and the S-1 response of the photomultiplier.

TABLE VIII
SHOCK WAVE STANDOFF DISTANCES

| Shock Tube ($R_B = 1$ inch) | Hypersonic Case | |
|---------------------------------|-----------------------------------|------------------------------------|
| | Shock Tunnel ($R_B = 1$ inch) | Freeflight ($R_B = 9.25$ feet) |
| $\delta_1 = 0.06$ inch | 0.028 inch | 3.11 inches |
| $\delta_2 = 0.18$ inch | 0.050 inch | 5.55 inches |
| $\delta_3 = 0.46$ inch | 0.340 inch | 37.74 inches |
| $\delta_4 = \text{---}$ | --- | --- |

Note: Solid angle viewed by fiber = 2.39×10^{-2} steradians

The scaling is based on the assumption that the ratio of the radiation heating rate between any two points on the body is proportional to the ratio of the local shock standoff distances and densities. Thus, for both the shock-tube and flight cases, a relation of the form

$$\frac{q_2}{q_1} = \left(\frac{\delta_2}{\delta_1} \right) \left(\frac{\rho_2}{\rho_1} \right) \quad (15)$$

holds. Since constant properties are assumed throughout the shock layer, this reduces to

$$\frac{q_2}{q_1} = \frac{\delta_2}{\delta_1} \quad (16)$$

scaling from the shock tube to flight conditions involves two steps. First, a scaling of the stagnation point heating rate, and then a scaling of that to points corresponding to those measured in the shock tube. The relations are:

$$q_{1c} = q_{1a} \left(\frac{\delta_{1c}}{\delta_{1a}} \right) \left(\frac{\rho_c}{\rho_a} \right) \quad (17)$$

$$q_{2c} = q_{1c} \left(\frac{\delta_{2c}}{\delta_{1c}} \right) \quad \& \quad q_{3c} = q_{1c} \left(\frac{\delta_{3c}}{\delta_{1c}} \right) \quad (18)$$

Using Equation (16) with the average of the measured values, the stagnation point heating rate for the flight case is found to be

$$q_{1c} = 7.13 \times 10^{-2} \text{ watts/cm}^2$$

for the 2.39×10^{-2} steradians viewed by the fibers. This compares with

$$q_{1c} = 11.2 \times 10^{-2} \text{ watts/cm}^2$$

calculated using Equation (14) and the Ames data from Figure 2a. Here the agreement is within a factor of 1.6.

The heating rate at the other two points on the cone surface are found from Equation (18) to be

$$q_{2c} = 0.127 \text{ watts/cm}^2$$

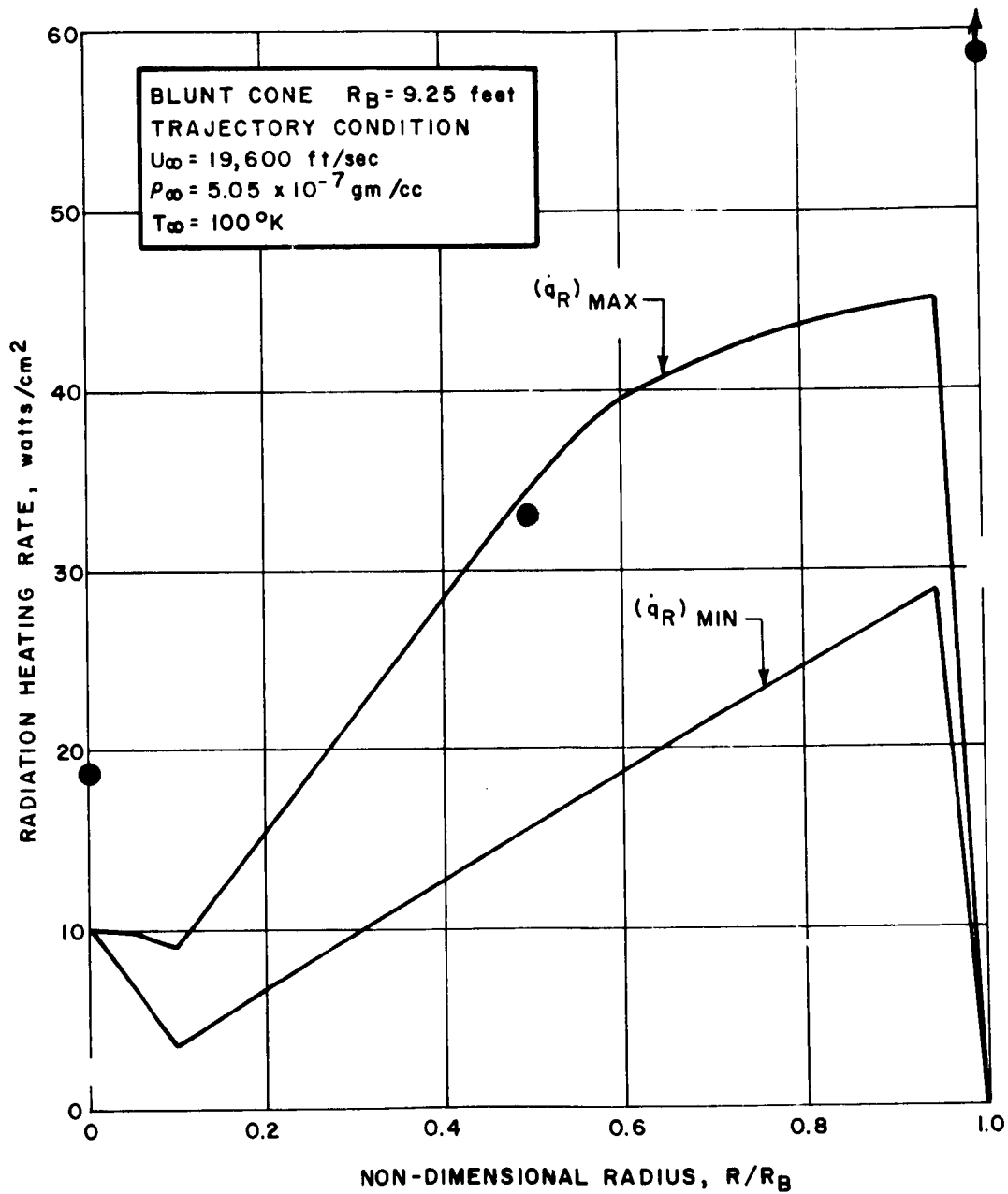
and

$$q_{3c} = 0.866 \text{ watts/cm}^2$$

These values are for the solid angle (2.39×10^{-2} steradians) viewed by the fiber optics, and must be corrected by the ratio $2\pi/2.39 \times 10^{-2}$ in order to be compared with the distribution calculated in Appendix C. The data are compared in Figure 25. It obviously overestimates the radiation at the cone edge. The reason for this difference probably lies in both the breakdown of the infinite slab approximation (used both in data scaling and in the theory) and in the fact that local conditions in the shock layer have strong axial gradients at this location, so that the choice of condition from which to compute the radiation is rather arbitrary. This can be seen directly from Table C-1 of Appendix C. The radiative density, H , is quite a strong function of the shock-wave angle, which decreases quite rapidly near the cone edge.

The same statement can be said here with regard to the question of which density is used for scaling as was said in Section D. Consequently, the ratio of the intensities along the cone with respect to the stagnation point are regarded as being more representative than are their absolute values.

The general trend predicted by the method of Appendix C is confirmed, except for the decrease in radiation around the blunt hemisphere tip to the junction with the cone ($R/R_B = 0.1$). This decrease in radiation is what has been predicted for a hemispherical nose by the analysis of References 5 and 6. The recent analysis of Reference 21 for a sphere, however, has shown that while the relative radiance per unit length ($\text{watt/cm}^3 \text{ ster}$) does decrease with distance from the stagnation point, the relative radiant intensity (watt/ster) first increases with distance from the stagnation point, goes to a maximum at a point on the surface whose normal makes an angle of about 30 degrees with the free stream, and then finally decreases.



86-9681

Figure 25 COMPARISON OF RADIATION HEATING RATE DISTRIBUTIONS

VII. CONCLUSIONS

In conclusion, the results of the present experimental investigation have indicated that the radiation measurements performed for various Mars entry body shapes at angle-of-attack in a shock tube can be used, along with hypersonic shock-shape measurements of these same bodies in a shock tunnel, to scale and compare the total over the body equilibrium heating load to similar body shapes at an actual Mars entry trajectory condition. The method is limited to scaling over pressure and size, requiring that the stagnation temperature be kept constant, and with the assumptions that the gas is optically thin and that the total radiative transfer can be assessed from that occurring in the 0.24- to 1.3-micron wavelength region.

The accuracy of the scaling analysis has been confirmed for a blunt 60-degree half-angle cone and a modified Apollo shape at zero angle-of-attack by comparing the radiation prediction (to within a factor of 2) with that actually measured in a ballistic range and with a simple theoretical analysis at the trajectory condition. The prediction for the tension shell shape was not confirmed in either case due to the lack of ballistic range data for this shape and because the flow field is so complex that the simple theoretical analysis is undoubtedly poor.

The experimental shock tube results scaled to the trajectory condition are:

| α | $\frac{W_{\text{Apollo}}}{W_{\text{Cone}}}$ | $\frac{W_{\text{Tension Shell}}}{W_{\text{Cone}}}$ |
|----------------------|---|--|
| $\alpha = 0$ degree | 2.91 | 16.02 |
| $\alpha = 45$ degree | 1.69 | 1.82 |
| $\alpha = 90$ degree | 2.97 | 0.69 |

The simplified scaling analysis was shown to be adequate for discriminating among various entry body shapes on the basis of total radiative energy transfer to within a scatter of 50 percent.

Although not requested in this contract, it is felt that the effects of vacuum ultraviolet radiation for this entry condition (especially that from the CO(4+) band system) and of nonequilibrium radiation on the radiative discrimination of entry body shapes have not been fully assessed.

In addition, the blunt-cone model instrumented with fiber optical bundles enabled the direct determination of the radiation at several locations on the surface of the body. The results confirm that the radiation heating rate is not a maximum at the stagnation point, but increased with distance along the cone to the cone edge.

It is felt that the present results indicate the usefulness of the fiber optics instrumentation technique for determining the more precise information necessary in assessing the accuracy of theoretical heating rate distributions along arbitrary body surfaces for actual atmospheric entry-heat shield design. This is felt to be extremely important for entry into the atmosphere of Venus at a higher density and velocity than that for Mars. In this case, the stagnation temperature will be high enough so that only continuum and atomic line emission will be important, while as the flow expands and cools away from the stagnation point, radiation from the binary systems will increase. Thus, an accurate determination of the distribution of the radiation heating rate around the body (for individual band systems as well as for the total integrated radiation intensity) will become increasingly necessary.

VIII. REFERENCES

1. Bobbit, P. J., Effects of shape on Total Radiative and Convective Heat Inputs at Hyperbolic Entry Speeds. Presented at the 9th Annual American Astronautical Society Meeting of the Interplanetary Missions Conference, Los Angeles, California (15-17 January 1963).
2. James, C., Experimental Study of Radiative Transport from Hot Gases Simulating in Composition and Atmospheres of Mars and Venus, AIAA J. 2, (1964) pp. 470-475.
3. Kivel, F., and K. Bailey, Tables of Radiation from High Temperature Air, Avco Everett Res. Rep. 21 (1957).
4. Meyerott, R. E., Radiation Heat Transfer to Hypersonic Vehicles, Presented at the Third AGARD Colloquium on Combustion and Propulsion, Palermo, Sicily, (17-21 March 1958).
5. De L'Estoile, H., and L. Rosenthal, Rapid Evaluation of Radiant Heating During Entry into the Atmosphere, Aeronautics and Astronautics - Proceedings of the Durand Centennial Conference (August 1959).
6. Strack, S. L., Radiant Heat Transfer around Re-Entry Bodies, ARS. J. 32, (1962) p. 744.
7. Kennett, H., and S. L. Strack, Stagnation Point Radiative Transfer, ARS. J. 31, (1961) p. 370.
8. Wolf, F., and J. M. Spiegel, Status of Basic Shock Layer Radiation Information for Inner-Planet Atmospheric Entry, AIAA Paper No. 66-421, Presented at the 4th Aerospace Sciences Meeting, Los Angeles, California (27-29 June 1966).
9. Myer, H. G., Ohrenberger, and R. T. Thompson, Emission and Absorption of Radiant Energy in a Model Planetary Atmosphere, AIAA Journal Vol. 3, No. 12 (December 1965) pp. 2203-2210.
10. Thomas, G. M., and W. A. Menard, Experimental Measurements of Non-Equilibrium and Equilibrium Radiation from Planetary Atmospheres, AIAA J. 4 (1966) p. 227.
11. Arnold, J. O., V. H. Reis, and H. T. Woodward, Studies of Shock Layer Radiation of Bodies Entering Planetary Atmospheres, AIAA J. 3 (1965) p. 2019.

12. Gruszczynski, J. S., and W. R. Warren, Experimental Heat Transfer Studies of Hypervelocity Flight in Planetary Atmospheres, AIAA J. 2 (1964) p. 1542.
13. Penner, S. S., Quantitative Molecular Spectroscopy and Gas Emissivities, Addison-Wesley, Reading, Mass. (1959).
14. Gillespie, R. D., and J. Warga, A Program for Computing Thermo-chemical Equilibrium Behind a Moving Shock Wave, Avco Report RAD-TM-63-65 (September 1963). J. Warga, J. Soc. Indust. Appl. Math. 11, 594 (1963).
15. Woodward, H. T., Private communication through H. Stumpf of J. P. L.
16. Williams, M. J., and C. E. Treavor, A Method for Calculating Diatomic Spectra Using a Digital Computer, CAL-QM-1626-A-5, Cornell Aeronautical Laboratory (May 1962).
17. Keck, J. C., J. C. Camm, B. Kivel, and T. Wentink, Radiation from Hot Air, Annals of Physics 7, (1959) p. 1.
18. Wolf, F., and Horton, T., Effect of Argon Addition on Shock Layer Radiation of CO₂ - N₂ Gas Mixtures, AIAA J. 2 (August 1964) pp 1472-1474.
19. J. P. L. Private Communication.
20. Gillespie, R. D., A Program to Compute the Expansion of an Arbitrary Gas in Thermochemical Equilibrium Through a Nozzle, Avco Technical Release, Program No. 1664.
21. Ball, H. W., H. G. Harris, and J. Hiatt, Design and Evaluation of a Radiometer System for Measuring Absolute Radiation from the Flow Field of a Hypervelocity Projectile, Presented at the 2nd International Congress on Instrumentation in Aerospace Simulation Facilities, Stanford University, (29 August 1966).
22. De Vos, J. C., A New Determination of the Emissivity of Tungsten Ribbon, Physics XX, (1954) pp. 690-714.
23. Modica, A. P., and H. B. Dyner, Analysis of Optical Radiation in the Wavelength Regions of 4216A, 4278A, 4835A, and 5165A Behind High-Speed Shock Waves into Low Density Martian Atmospheres, Final Report NASA/Ames Contract NASW 1208 (in preparation).

24. JPL Entry Vehicle Design Computer Program Users Manual, AVSSD-0001-66-RR, JPL Contract 951070 (26 May 1966).
25. Comparative Studies of Conceptual Design and Qualification Procedures for a Mars Lander, Final Report AVSSD-0006-66-RR, 11, May 1966, Contract NAS 1-5224, Vol. V., Book 2, Aeromechanics and Thermal Control.

APPENDIXES

- A. RADIATION CALIBRATION THEORY
- B. OPTICALLY THIN-EQUILIBRIUM RADIATION CRITERIA
- C. THEORETICAL RADIATION CALCULATIONS
- D. SHOCK-TUBE SIMULATION OF RADIATIVE INTENSITY

$$K = \frac{V_c}{W_{eff}}, \text{ volts/watt} \quad (A2)$$

When the same radiometer system is used to measure the radiation from the shock layer about the body, the spectral distribution is from an unknown source rather than from a standard lamp, but the same basic equation still holds.

The data of interest are the total intensities over the entry body shape in the entire wavelength interval through which the radiometers are sensitive; i.e.,

$$W = \int_{\lambda_1}^{\lambda_2} I(\lambda) \frac{A_1 A_2}{d^2} \cos \theta d\lambda \quad (A3)$$

However, the effective intensity seen by the radiometer is once again given by

$$W_{eff}^* = \int_0^{\infty} I_{\lambda} \frac{A_1 A_2}{d^2} \cos \theta t_1(\lambda) t_2(\lambda) t_3(\lambda) d\lambda \quad (A4)$$

and

$$W_{eff}^* = \frac{V}{K} \quad (A5)$$

Equation (A4) is the same as Equation (A1), except that I_{λ} , the unknown spectral distribution has been substituted for S_{λ} , the lamp spectral intensity, and $t_3(\lambda)$, an additional spectral transmissivity of any windows not present during calibration is included. To reduce the data, we must assume a theoretical spectral distribution for the unknown spectral distribution. We then obtain the following correction factor,

$$\bar{f} = \left(\frac{W_{eff}^*}{W^*} \right)_{\text{theoretical}} = \frac{\int_0^{\infty} (I_{\lambda})_{\text{theor.}} \cos \theta \frac{A_1 A_2}{d^2} t_1(\lambda) t_2(\lambda) t_3(\lambda) d\lambda}{\int_{\lambda_1}^{\lambda_2} (I_{\lambda})_{\text{theor.}} \cos \theta \frac{A_1 A_2}{d^2} d\lambda} \quad (A6)$$

The values of \bar{f} found using the theoretical spectral distribution given in Figure 2 are shown in Table A-I. The correct intensity is then found from

$$W^* = V/K\bar{f} \quad (A7)$$

TABLE A-I
SPECTRAL CORRECTION FACTORS

| \bar{f}_B (blue filter, S-11) | \bar{f}_R (red filter, S-1) |
|---------------------------------|-------------------------------|
| (3400Å to 5600Å) | (4800Å to 13,000Å) |
| Shock Tube 0.264 | 0.538 |
| Ballistic Range 0.310 | 0.454 |
| | 3000Å to 12,000Å |
| Shock Tube (Fiber Bundle) | 0.729 |

APPENDIX B

OPTICALLY THIN - EQUILIBRIUM RADIATION CRITERIA

A. EQUILIBRIUM RADIATION CRITERION

The choice of ballistic range test pressure was made on the basis of that required to ensure that the gas cap radiation was primarily equilibrium radiation. The method of determining the pressure was as follows:

Oscilloscope traces which monitored the nonequilibrium CN violet radiation behind incident shock waves²³ (in a shock tube) into two typical Martian atmospheres (10-percent CO₂ + 90-percent N₂ and 50-percent CO₂ + 50-percent N₂) were used to obtain an estimate of the particle time required to ensure that the total integrated radiation was no more than six-fifths (6/5) that of the equilibrium radiation. Then binary scaling was used, with an estimate of a typical stay time in the shock layer of the projectile (taken for convenience as $R_B/5U$, where U is the average particle velocity relative to the body), to obtain the test pressure required to achieve this condition.

The pressures deduced were 220 torr for the 10-percent CO₂ + 90-percent N₂ mixture, and 120 torr for the 50-percent CO₂ + 50-percent N₂ mixture. Consequently, a choice of 150 torr was made for the 30-percent CO₂ + 70-percent N₂ mixture of this investigation.

The initial pressure in the shock tube was chosen by requiring that the stagnation pressure-diameter product was the same as that in the ballistic range. Further insurance of the achievement of equilibrium radiation in the shock tube case was due to testing in the gas which has been processed by the incident shock.

B. OPTICALLY THIN-SHOCK LAYER CRITERION

The possibility of self-absorption in the range tests was checked using the simplified analysis of Reference 9. The criterion by which one ascertains whether self-absorption is present is when the nongrey absorption coefficient, μ^* , of Reference 9, for a band system, multiplied by a characteristic length in the flow field is of the order-of-unity.

Since the band system of maximum importance in the wavelength region investigated here is the CN violet, we investigate its self-absorption characteristics.

From Figure 10 of Reference 9[†], $\mu^* \approx 2 \text{ cm}^{-1}$ at 15,000 ft/sec and $p = 50$ atmospheres. With a shock standoff distance equal to 0.08 cm (obtained from the shock-tunnel photograph of the Apollo, and then scaled to the range model size), this yields

$$\delta_1 \mu^* = 0.16 \text{ for the range condition.}$$

Similarly for the shock tube, $\mu^* \approx 10^{-2} \text{ cm}^{-1}$ at 11,000 ft/sec and $p = 20$ atmospheres and the standoff distance of 0.825 cm, and we have

$$\delta_1 \mu^* = 8.25 \times 10^{-3} \text{ for the shock tube condition.}$$

This implies that self-absorption is not present in the range or any of the shock tube tests.

[†]We use this figure, even though it has been calculated for a mixture of 15-percent CO_2 + 85-percent N_2 , because Figure 12 of the same paper shows that for our gas composition (30-percent CO_2 + 70-percent N_2), the total radiation intensity for CN (V), CN (R), N_2 (1^+), and N_2 (2^+) decreased from that used to determine μ^* in Figure 10 of Reference 9.

APPENDIX C

THEORETICAL RADIATION CALCULATIONS

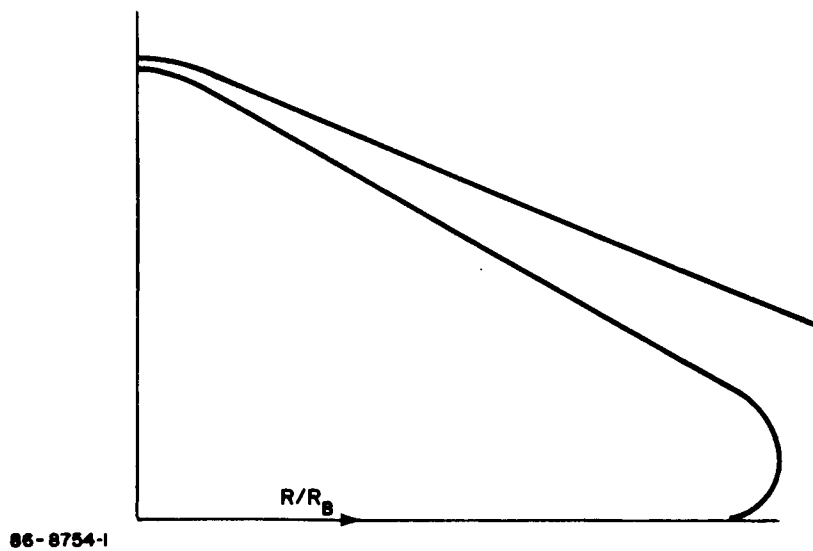
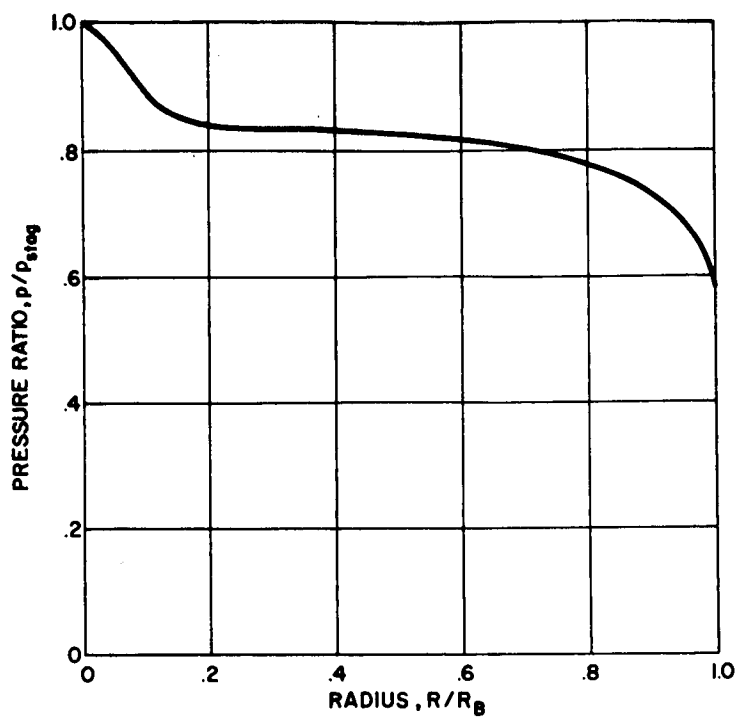
A theoretical analysis was performed comparing the total equilibrium radiation heating for the selected flight condition and for 18.5 foot base diameter vehicles. The shock shapes obtained in the shock-tunnel tests yielded shock angles which were used to compute the flow conditions and then the radiation intensity at the outer edge of the shock layer. By use of the shock angles and the pressure distributions around the body (see Figure C-1)* radiation intensity distributions around the body were computed. The radiation intensity (assuming a transparent gas layer) is based on computer program 1885 described in Reference 24.

Figures C-2 through C-4 show the maximum heating rate distribution, $\dot{q}_{R \max}$ (obtained by multiplying the intensity at the body by the local-shock standoff distance), the minimum heating rate distribution, $\dot{q}_{R \min}$ (obtained by taking the product of the local-shock standoff distance and the radiation intensity at the shock wave), and the linear average heating rate distribution, used for all comparisons. This average heating rate is too high, especially near the cone edge, because the high-radiation intensities corresponding to values close to that at the wall are confined to a relatively thin layer, and most of the shock layer is at a value close to that corresponding to $\dot{q}_{R \min}$. The flow properties as a function of shock angle are tabulated in Table C-1.

The total radiative heat load to the three shapes as predicted by the calculations is summarized below:

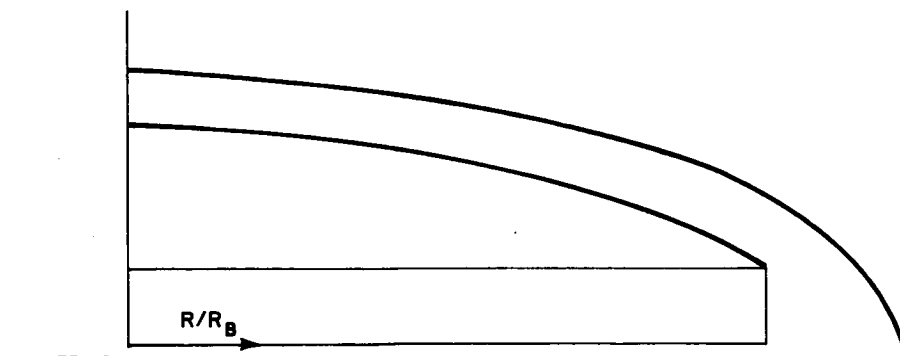
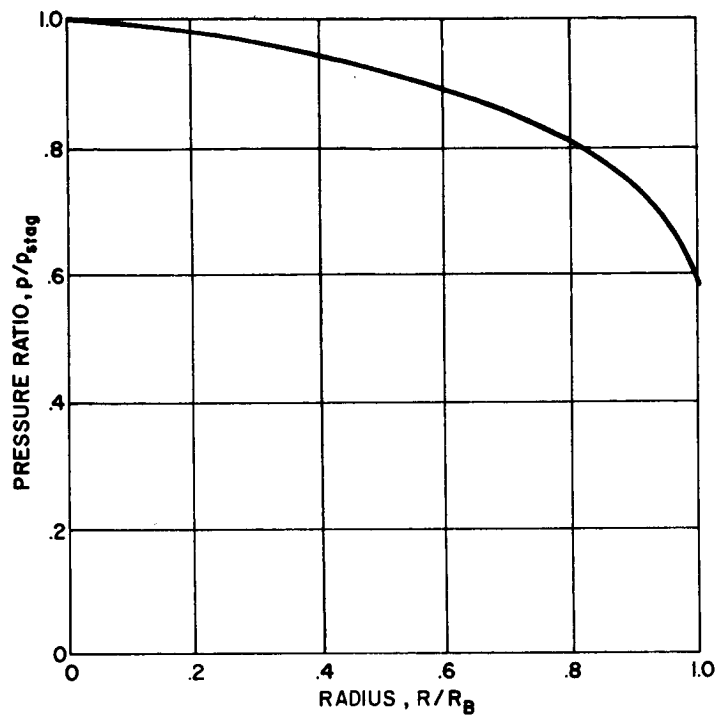
| | Ratio of total equilibrium radiation to that for the cone |
|---------------|--|
| Cone | 1.00 |
| Apollo | 1.25 |
| Tension Shell | 1.45 |

*The pressure distributions for the Apollo and blunt cone (see Reference 25) were obtained from the Avco/SSD blunt-body program. The pressure distribution about the tension shell is obtained from Newtonian theory, except in the shock interaction zone where a pressure recovery greater than that obtained from normal shock stagnation pressure is possible due to the high efficiency of the multiple shock compression process.



66-8754-1

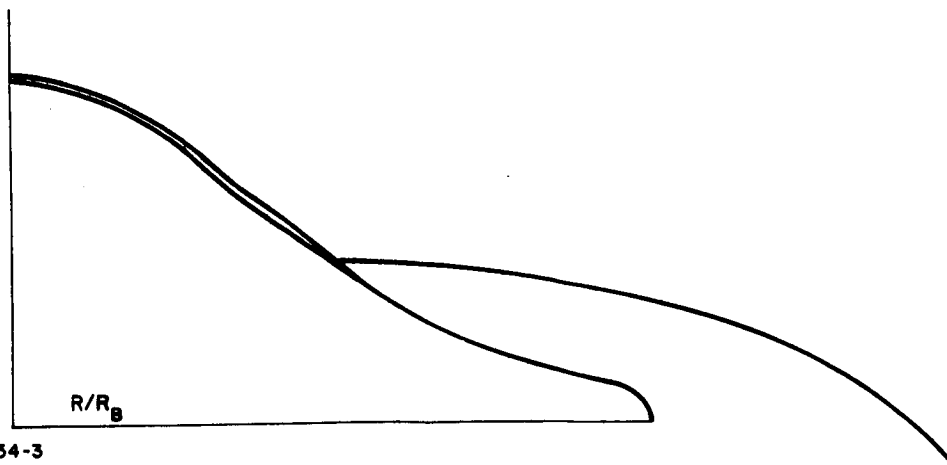
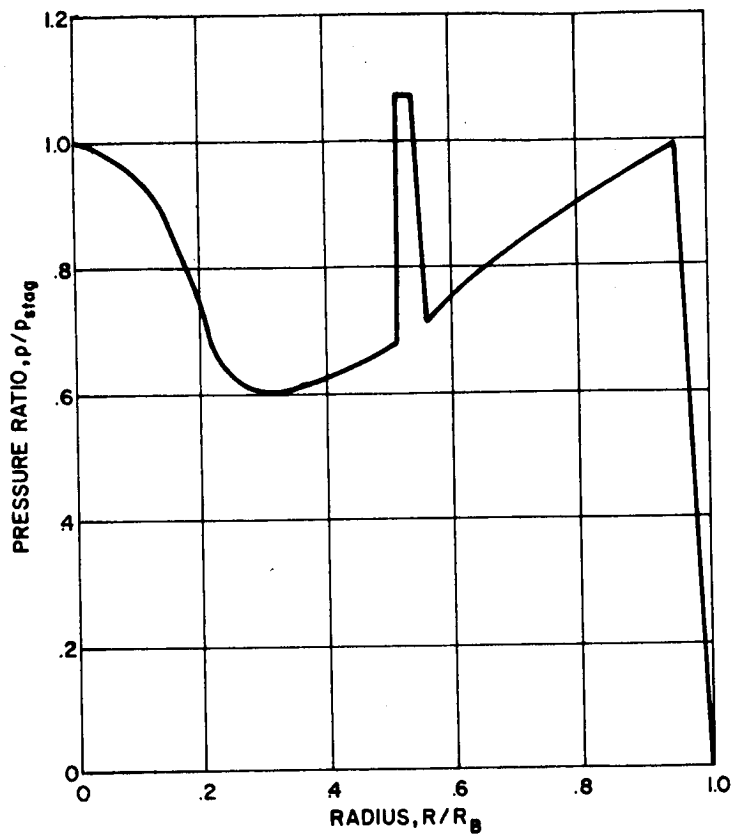
Figure C-1a BLUNT-CONE HYPERSONIC SHOCK SHAPE AND PRESSURE DISTRIBUTION



86-8754-2

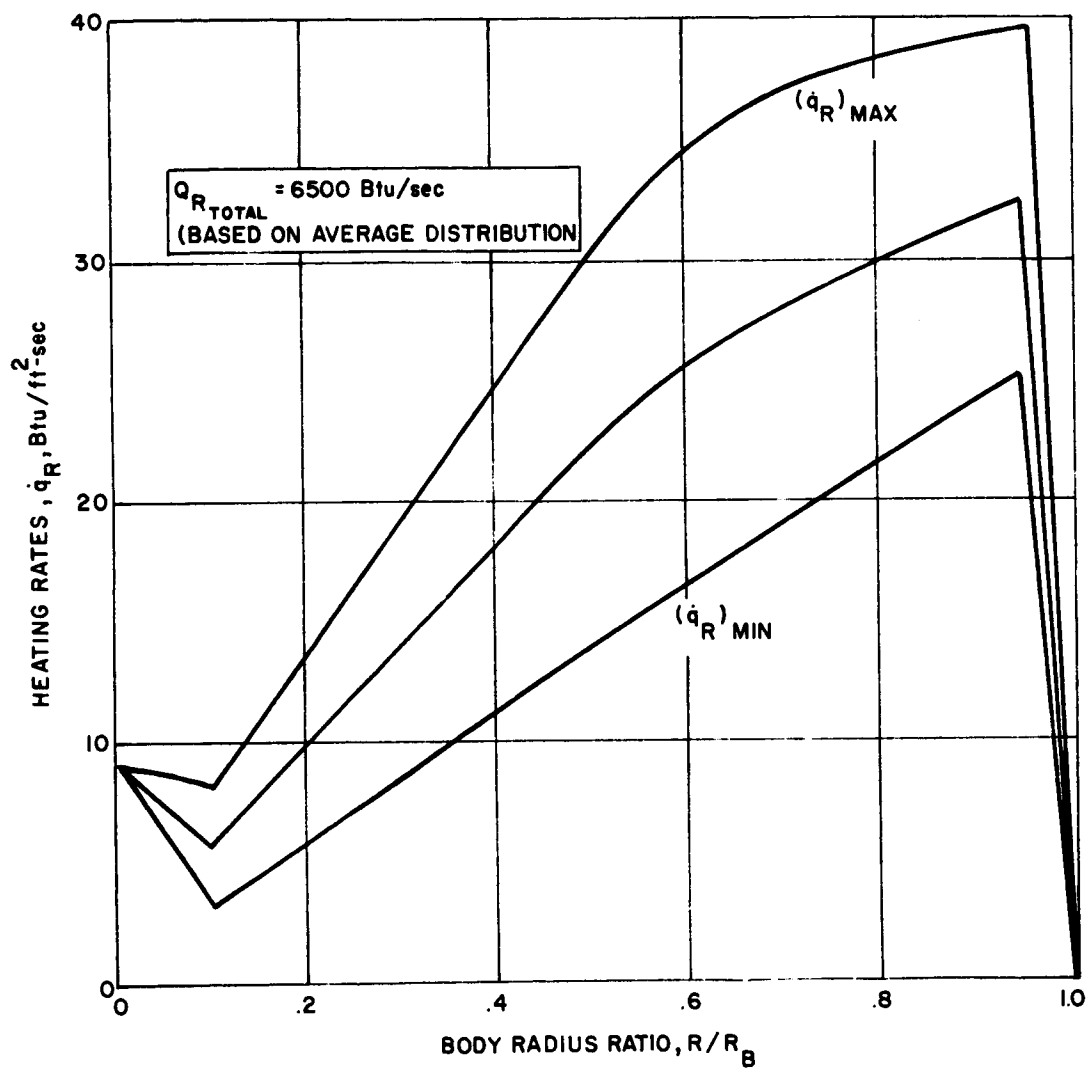
Figure C-1b MODIFIED APOLLO HYPERSONIC SHOCK SHAPE AND PRESSURE DISTRIBUTION

94



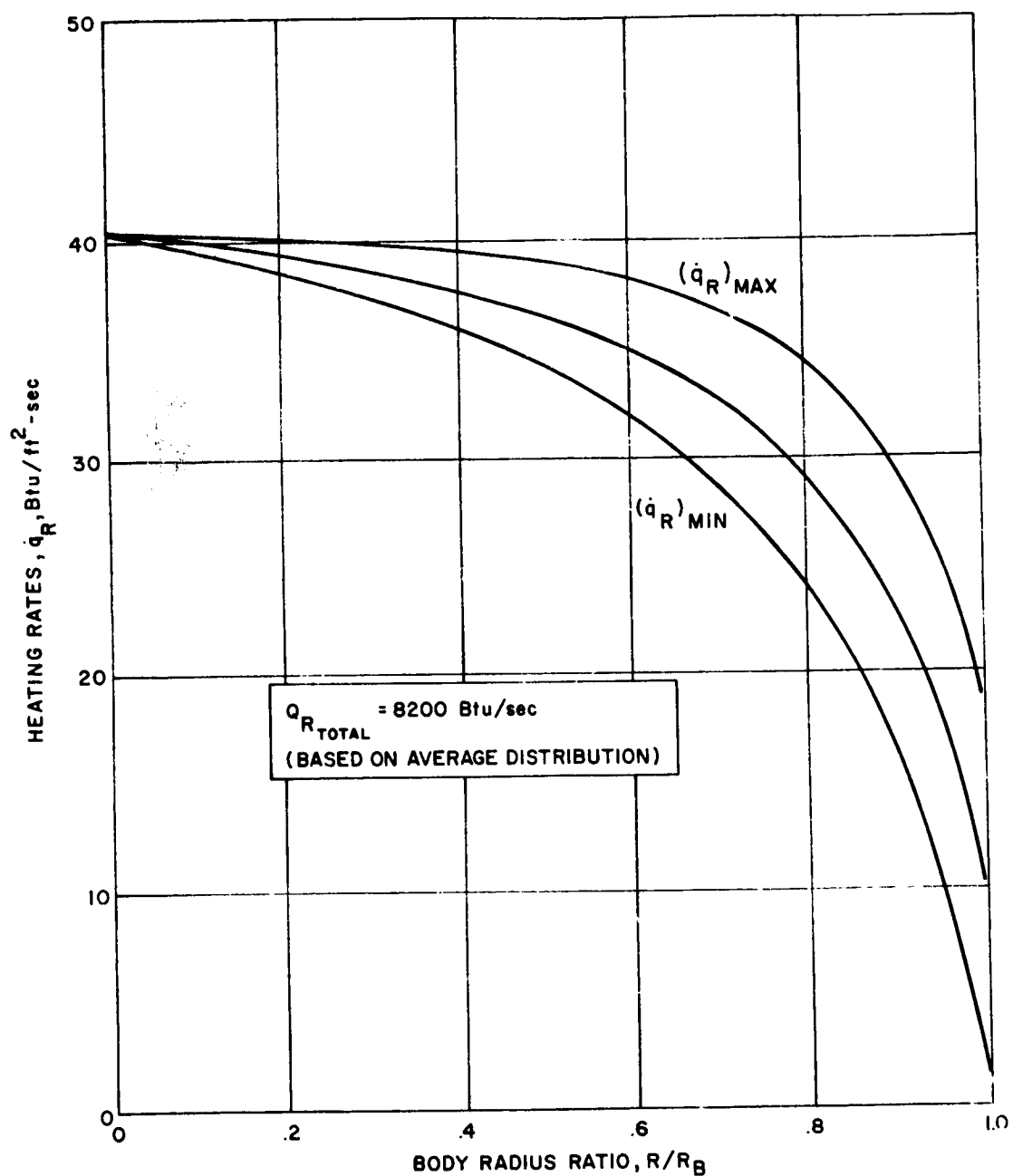
86-9754-3

Figure C-1c TENSION SHELL HYPERSONIC SHOCK SHAPE AND PRESSURE DISTRIBUTION



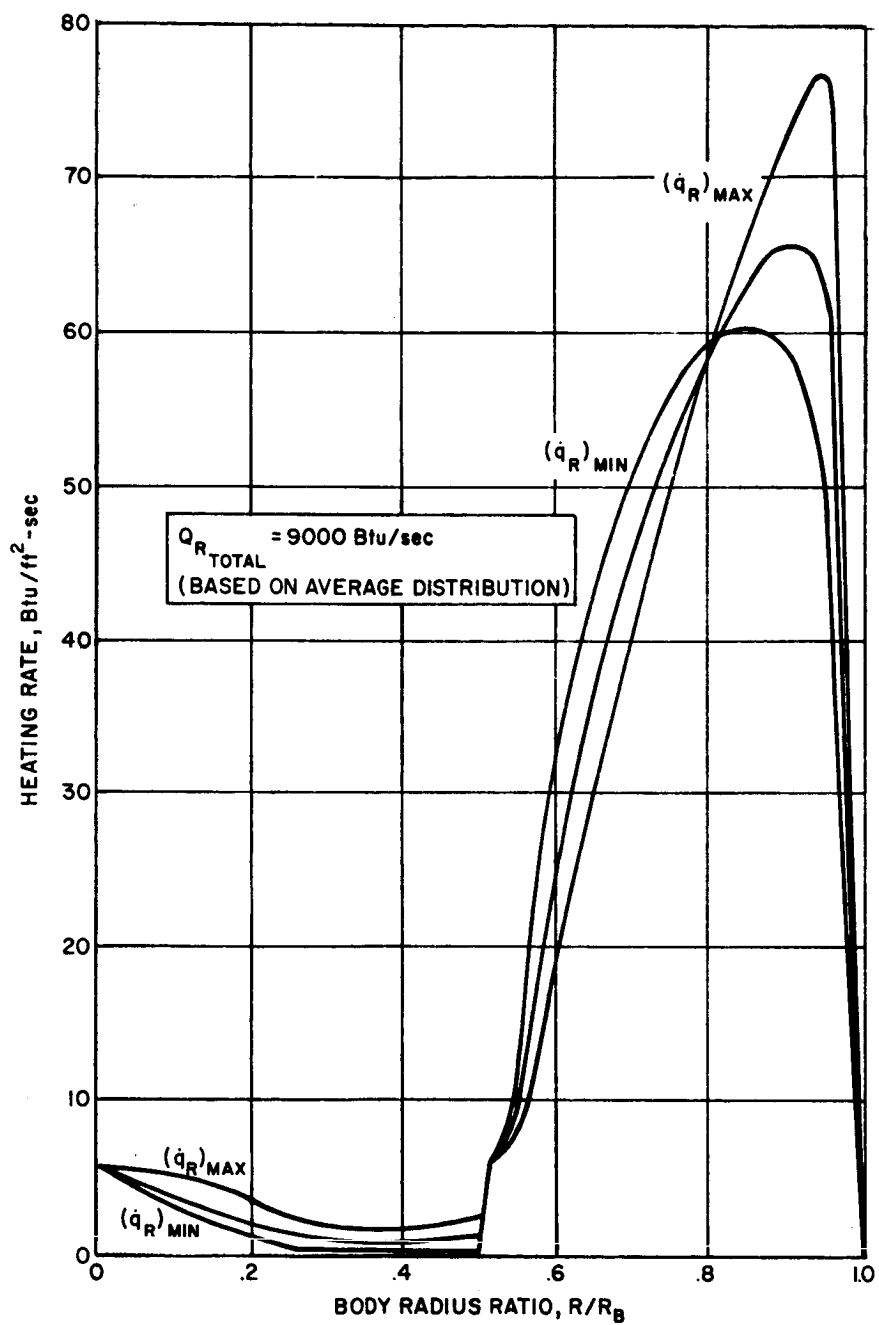
86-9682

Figure C-2 BLUNT-CONE AND TRAJECTORY CONDITION RADIATION HEATING RATE DISTRIBUTION



86-8755

Figure C-3 MODIFIED APOLLO TRAJECTORY CONDITION RADIATION HEATING RATE DISTRIBUTION



86-8756

Figure C-4 TENSION SHELL TRAJECTORY CONDITION HEATING RATE DISTRIBUTION

TABLE C-1
TRAJECTORY POINT RADIATION PROPERTIES

| Wave (degrees) | T _∞ °K | P earth atm. | $\rho_{\text{wave}}/\rho_{\infty}$ | H _{wave} (Btu/ft ³ sec) | H _{body} (Btu/ft ³ sec) |
|-------------------|----------------------|-----------------|------------------------------------|--|--|
| 90 | 5750 | 0.174 | 15.5 | 109 | 109 |
| 86 | 5730 | 0.168 | 15.5 | 108 | 109 |
| 82 | 5690 | 0.165 | 15.4 | 97.6 | 105 |
| 78 | 5650 | 0.161 | 15.2 | 84.1 | 100 |
| 74 | 5590 | 0.155 | 15.0 | 69.0 | 93.5 |
| 68 | 5450 | 0.144 | 14.6 | 40.8 | 81.2 |
| 67 | 5420 | 0.142 | 14.5 | 36.0 | 79.0 |
| 66 | 5400 | 0.140 | 14.4 | 33.0 | 76.5 |
| 52 | 4610 | 0.103 | 13.4 | 0.810 | 42.6 |
| 84 | 5720 | 0.167 | 15.5 | 106 | 108 |

APPENDIX D

SHOCK-TUBE SIMULATION OF RADIATIVE INTENSITY

The measurement of radiative flux to scaled models can be conveniently performed in the shock tube. The simulation of flight conditions is feasible in the case of equilibrium flow field and radiation. Nonequilibrium radiation is best studied behind the incident shock, i. e. , without using a model, and will not be considered further in the present discussion.

Shock-tube test conditions can be chosen to provide the correct stagnation enthalpy and to simulate optical thickness at the stagnation point. However, the test flow Mach number is low ($M_2 \sim 2$ to 3), and the equilibrium test flow behind the incident shock is both preheated and predissociated. In other words, only a fraction of the stagnation enthalpy, say $\alpha^2 < 1$ (where $\alpha = U_2/U_\infty$, and where U_2 and U_∞ are test-flow and flight velocities respectively), appears as kinetic energy of the test flow

$$u_2 = u_\infty \alpha \quad (D1)$$

For equilibrium flow, the state-of-the-gas behind the bow shock of the model is controlled by stagnation enthalpy and by α at a given shock slope. Indeed, the dependence on pressure along the shock is essentially negligible. Since $\alpha < 1$, the shock-tube flow around the model will be hotter than in flight, except at the stagnation point, where exact matching can be obtained. Since the radiation intensity varies strongly with temperature, it is useful to estimate the error incurred in simulation at given shock slope and specified α . Then, α can be chosen (by controlling test conditions) to reduce the maximum error within an acceptable limit.

The calculation is very simple. Consider the data of Figure D-1 which represents normalized intensity, $\frac{I}{I_{\text{stag}}}$, as a function of shock angle, θ . These data apply to the Martian atmosphere (30-percent CO_2 , 70-percent N_2) at a reentry velocity of 21,000 ft/sec and a free-stream density of 10^{-6} gm/cc. These values are chosen as a typical example to demonstrate the method. As noted above, the radiation intensity at stagnation, I_{stag} ($\theta = 90$ degrees), can be matched exactly in the shock tube. The curve of Figure D-1 is applicable to both flight and shock-tube tests when it is interpreted in terms of static enthalpy of the shocked gas. Indeed, the pressure dependence has been essentially absorbed into the normalization (by I_{stag}). Using the Hugoniot conditions for large density ratio, one finds

$$\frac{h(\alpha, \theta)}{h_{\text{stag}}} \approx 1 - \alpha^2 \cos^2 \theta, \quad h_{\text{stag}} \approx \frac{1}{2} u_\infty^2 \quad (D2)$$

These curves are plotted in Figure D-2 for $a^2 = 1$ (flight), $1/2$, $2/3$ and $4/5$. The case $a^2 = 2/3$ corresponds to practical shock-tube test conditions in the Martian atmosphere. As expected, $\frac{h}{H_{stag}}$ increases with decreasing a , i. e., as the test flow becomes hotter for a given stagnation enthalpy.

Figures D-1 and D-2 can be combined to yield the normalized intensity as a function of α and θ . The results are shown in Figure D-3.

The basis of comparison is $\frac{I_{st} - I_f}{I_{stag}}$, namely the difference between normalized intensity in the shock tube, $\frac{I_{st}}{I_{stag}}$, and normalized intensity in flight, $\frac{I_f}{I_{stag}}$.

At $\theta = 90$ degrees, this difference vanishes for all cases because of normalization. For all θ and $a = 1$, the difference also vanishes (exact simulation). For small θ and any a , the difference becomes small, because I decays rapidly with shock angle. Near $\theta = 60$ degrees, the curves show a maximum. The height of this maximum is interpreted here as the maximum simulation error. The following values are obtained from Figure D-3.

| a^2 | 1 | 4/5 | 2/3 | 1/2 |
|---------------|---|------------|------------|------------|
| Maximum Error | 0 | 13 percent | 22 percent | 35 percent |

The maximum error decreases rapidly with increasing a^2 .

This method can be used to estimate simulation error in a convenient manner. It does not require knowledge of the complete flow field around the model, thus it can be applied to models at high angle-of-attack. On the other hand, the present estimate is conservative, because it is based on maximum error and on radiation behind the shock. Indeed, this latter decreases more slowly with θ than the radiation flux to the body, because the radiating gas cap thins out at increasing θ .

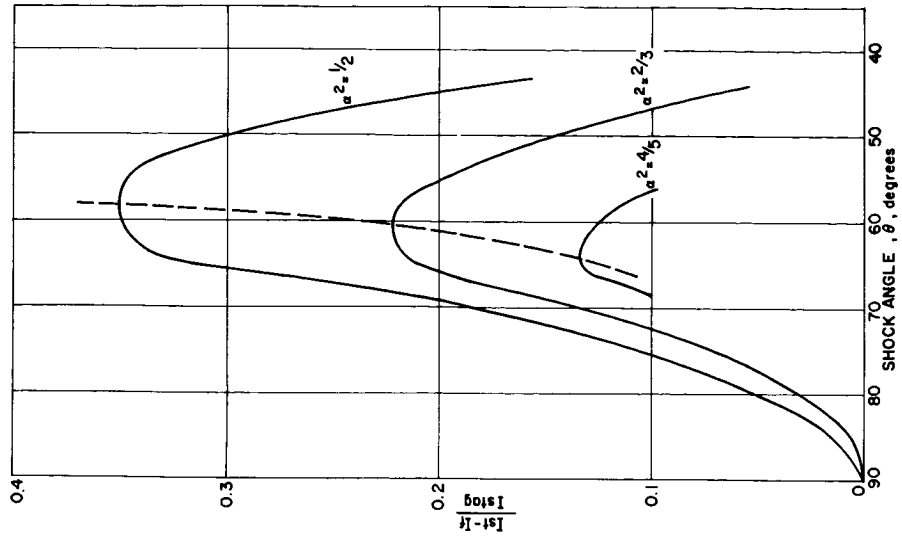
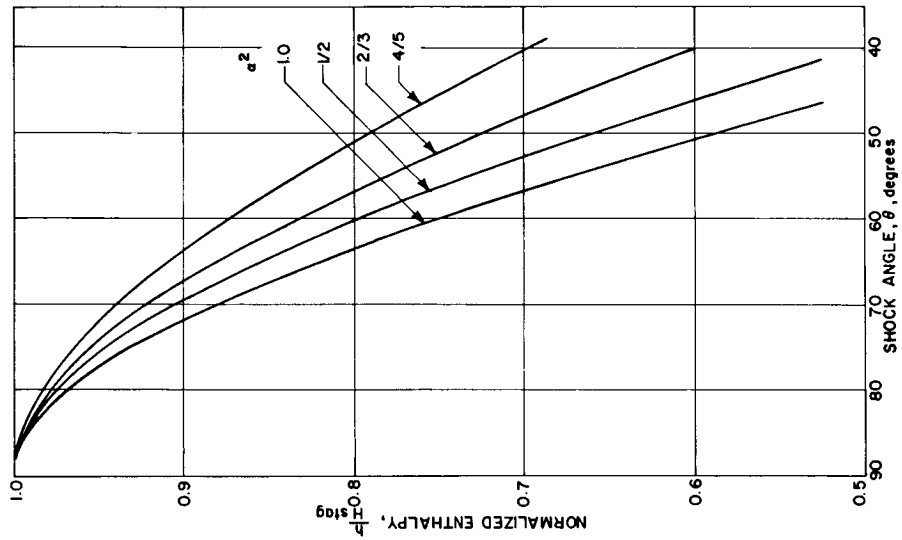
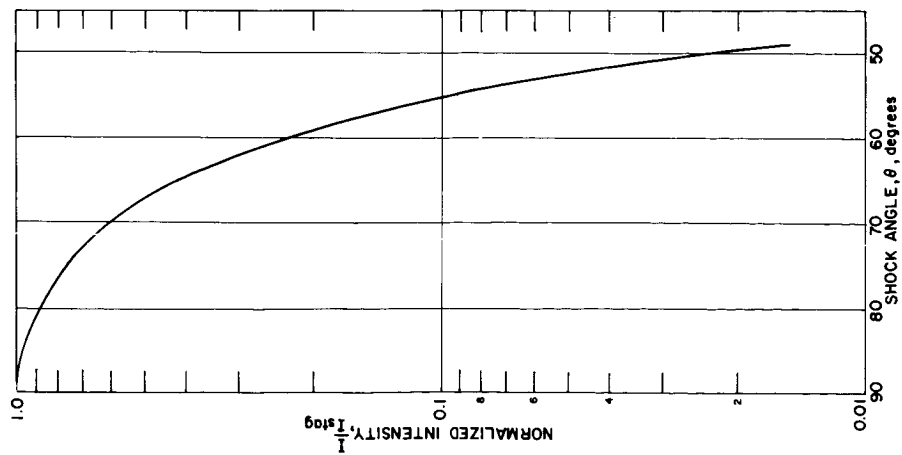


Figure D-1 INTENSITY RATIO VERSUS SHOCK ANGLE Figure D-2 ENTHALPY RATIO VERSUS SHOCK ANGLE Figure D-3 INTENSITY ERROR VERSUS SHOCK SHAPE

DISTRIBUTION

| <u>Addressee</u> | <u>No. of Copies</u> |
|---|----------------------|
| Jet Propulsion Laboratory (+1 reproducible) 4800 Oak Grove Drive Pasadena, California Attn: Dr. Stumpf | 6 |
| Research Library - Wilmington (+1 reproducible) | 3 |
| Research Library - Lowell (+1 reproducible) | 1 |
| Reports Distribution Center - Wilmington | 57 |